STUDIES OF COBALT AND IRON OXIDES/ OXYHYDROXIDES NANOSTRUCTURES FOR ELECTROCHEMICAL APPLICATIONS

LEE KIAN KEAT

NATIONAL UNIVERSITY OF SINGAPORE

2014

STUDIES OF COBALT AND IRON OXIDES/ OXYHYDROXIDES NANOSTRUCTURES FOR ELECTROCHEMICAL APPLICATIONS

LEE KIAN KEAT
(M. Sc., Universiti Teknologi Malaysia)

A THESIS SUBMITTED

FOR THE DEGREE OF
DOCTOR OF PHILOSOPHY

DEPARTMENT OF CHEMISTRY

NATIONAL UNIVERSITY OF SINGAPORE

2014

DECLARATION

I hereby declare that the thesis is my original work and it has been written by me in its entirely, under the supervision of Assoc. Prof. Sow Chorng Haur (Department of Physics) and Assoc. Prof. Chin Wee Shong (Department of Chemistry), National University of Singapore, between 3 August 2009 and 31 Jan 2014.

I have duly acknowledged all the sources of information which have been used in the thesis. This thesis has also not been submitted for any degree in any university previously.

The content of the thesis has been partly published in:

1. Lee, K. K., Loh, P. Y., Sow, C. H., Chin, W. S. CoOOH nanosheet electrodes: Simple fabrication for sensitive electrochemical sensing of hydrogen peroxide and hydrazine. *Biosensors and Bioelectronics,* **2013**, *39*, 255-260. **(Chapter 3 & 5)**

2. Lee, K. K., Loh, P. Y., Sow, C. H., Chin, W. S. CoOOH nanosheets on cobalt substrate as a non-enzymatic glucose sensor. *Electrochemistry Communications,* **2012**, *20*, 128-132. **(Chapter 4)**

3. Lee, K. K.[#], Deng, S.[#], Fan, H. M., Mhaisalkar, S., Tan, H. R., Tok, E. S., Loh, K. P., Chin, W. S, Sow, C. H. α-Fe_2O_3 nanotubes-reduced graphene oxide composites as synergistic electrochemical capacitor materials. *Nanoscale,* **2012**, *4*, 2958-2961. (# equal contribution). **(Chapter 6)**

4. Lee, K. K., Ng, R. W. Y., She, K. K., Sow, C. H., Chin, W. S. Vertically aligned iron (III) oxyhydroxide/oxide nanosheets grown on iron substrates for electrochemical charge storage. *Materials Letters*, 2014, 118, 150-153. **(Chapter 7)**

Lee Kian Keat		31 January 2014
Name	Signature	Date

Acknowledgement

I would like to express my greatest gratitude to the following people who has directly or indirectly supported and helped me throughout my PhD study. Without their presence, this thesis is not possible! Thank you very much!!

Mentors

A/Prof. Sow Chorng Haur
A/Prof. Chin Wee Shong
Dr. Xie Xianning

Co-directors @ NUSNNI

Prof. Andrew Wee T.S.
Prof. Loh Kian Ping
Prof. Mark Breese
Prof. T. V. Venkatesan

(Ex-)Colleagues @ NUSNNI

Amanda Lee
Chan Sook Fun
Chin Kok Chung
Chung Hung Jing
Jasmin Lee
Jocelyn Tang
Junnie Teo
Liu Minghui
Van Li Hui
Rajiv R. Prabhakar
Stephen Ng
Tan Chia yin
Wang Junzhong
Wang Qian
Wang Yuzhan

Lab mates @ Chem.

Barry Huang Baoshi
Chen Jiaxin
Doreen Yong Wei Ying
Elgin Ting Zhi Hong
Li Guangshuo
Neo Min Shern
Joy Ng Chun Qi
Khoh Rong Lun
Loh Pui Yee
Sharon Teo Tingting
Tan Zhi Yi
Wang Shuai

Lab technologists & other officers

Chen Gin Seng
Ho Kok Wen
Hong Yimian
Foo Eng Tin
Lee Ka Yau
Ong Pang Ming
Suriawati Bte Sa'ad
Tan Choon Wah
Tan Geok Kheng
Tan Teng Jar
Wong How Kwong

Lab mates @ Physics

Bablu Mukherjee
Binni Varghese
Chang Sheh Lit
Christie T. Cherian
Deng Suzi
Lena Lui Wai Yi
Lim Kim Yong
Lim Zhi Han
Lu Junpeng
Hoi Siew Kit
Hu Zhibin
Rajesh Tamang
Sara Azimi
Sharon Lim Xiaodai
Tao Ye
Teoh Hao Fatt
Yun Tao
Zheng Minrui
Zhu Yanwu

Collaborators

Mak Wai Fatt
Poh Chee Kok
Wei Dacheng
Tang Zhe
Teh Pei Fen

Table of Contents

		Page
Contents		i
Summary		v
List of Tables		vi
List of Figures		vii
List of Abbreviations		x
List of Publications		xi
List of Conference Presentations		xiii

Chapter 1 Introduction

1.1	The role of nanoscience in renewable energy	1
1.2	Electrochemical storage: electrochemical capacitors	3
1.2.1	Electric double layer capacitors (EDLC) vs. pseudocapacitors	4
1.2.2	Research trends in development of the electrode materials for electrochemical capacitors (ECs)	6
1.3	Transition metal oxides/ oxyhydroxides nanostructures in electrochemical sensing	7
1.4	Oxidation routes to in situ growth of nanostructures	10
1.5	Properties of cobalt compounds relevant to electrochemical applications	12
1.5.1	Electrochemical capacitance and electrochemistry of cobalt compounds	12
1.5.2	Oxidation mechanism of different cobalt compounds and topotactic relationship	14
1.6	Iron oxides/ oxyhydroxides in electrochemical capacitors	17
1.7	Objectives and scope of thesis	21
1.8	References	23

Chapter 2 Co_3O_4 nanowalls synthesized via thermal oxidation for electrochemical capacitor

2.1	Introduction	28

2.2 Experimental Section 29
2.2.1 Synthesis of cobalt oxide nanostructures 29
2.2.2 Characterizations 30
2.2.3 Electrochemical studies 30
2.3 Results and Discussion 31
2.3.1 Synthesis and characterizations of cobalt oxide nanostructures 31
2.3.2 Detailed calculation procedures of Co_3O_4 mass on cobalt foil 40
2.3.3 Electrochemical studies of cobalt oxide nanostructures 41
2.4 Conclusions 47
2.5 References 48

Chapter 3 Fabrication of CoOOH and Co_3O_4 nanosheets and their comparative electrochemical capacitance studies
3.1 Introduction 50
3.2 Experimental Section 52
3.2.1 Synthesis of CoOOH nanosheets 52
3.2.2 Thermal conversion of CoOOH to Co_3O_4 nanosheets 52
3.2.3 Characterizations 53
3.2.4 Electrochemical studies 53
3.3 Results and Discussion 54
3.3.1 Formation and characterizations of CoOOH nanosheets 54
3.3.2 Thermal conversion of CoOOH to Co_3O_4 nanosheets 60
3.3.3 Comparative electrochemical studies of CoOOH and Co_3O_4 nanosheets 65
3.4 Conclusions 71
3.5 References 71

Chapter 4 CoOOH nanosheets electrode: Electrochemical sensing of glucose
4.1 Introduction 74
4.2 Electrochemical experiments 75
4.3 Results and Discussion 75
4.3.1 Electrochemical events of CoOOH nanosheets 75

4.3.2 CoOOH nanosheets electrode as a glucose sensor 78
4.3.3 The performance of CoOOH electrode in the presence of chloride 81
4.3.4 The performance of CoOOH electrode in the presence of interfering compounds 82
4.3.5 Effect of electrolyte concentration and reproducibility of CoOOH electrode 83
4.4 Conclusions 84
4.5 References 85

Chapter 5 **CoOOH nanosheets electrode: Electrochemical sensing of hydrogen peroxide and hydrazine**
5.1 Introduction 87
5.2 Electrochemical studies 89
5.3 Results and Discussion 89
5.3.1 Electrochemical sensing of H_2O_2 on CoOOH nanosheets 89
5.3.2 Electrochemical sensing of N_2H_4 on CoOOH nanosheets 95
5.4 Conclusions 100
5.5 References 100

Chapter 6 **α-Fe_2O_3 nanotubes-reduced graphene oxide composites as synergistic electrochemical capacitor materials**
6.1 Introduction 103
6.2 Experimental Section 105
6.2.1 Synthesis of rGO, α-Fe_2O_3 NTs, and α-Fe_2O_3 NTs-rGO composites 105
6.2.2 Characterizations 106
6.2.3 Preparation of working electrodes 106
6.2.4 Electrochemical studies 107
6.3 Results and Discussion 107
6.3.1 Synthesis and characterizations of α-Fe_2O_3 NTs-rGO composite 107

6.3.2 Electrochemical studies 113

6.4 Conclusions 118

6.5 References 118

Chapter 7 **Vertically aligned iron (III) oxyhydroxide/oxide nanosheets grown on iron substrates for electrochemical charge storage**

7.1 Introduction 121

7.2 Experimental 122

7.3 Results and Discussion 123

7.3.1 Characterizations of the nanostructured iron compound 123

7.3.2 Electrochemical studies in three different electrolytes 124

7.3.3 Cycling stability of electrodes in Na_2SO_3 and Na_2SO_4 127

7.4 Conclusions 128

7.5 References 129

Chapter 8 **Conclusions and Outlook** 130

Summary

Firstly, cobalt oxide (Co_3O_4) nanostructures with different morphology prepared by thermal oxidation were evaluated as an electrode for electrochemical capacitors (*Chapter 2*). By exploiting the *in situ* chemistry of cobalt, an innovative synthesis route was developed to fabricate cobalt oxyhydroxide (CoOOH) nanosheet arrays. The nanostructured thin film was prepared by simply oxidizing cobalt foil in alkaline medium at room temperature, without catalyst, template and electrical current or voltage. A conversion of CoOOH nanosheets to Co_3O_4 nanosheets was performed, and both species were adequately characterized by a comprehensive range of techniques. Comparative electrochemical studies revealed that CoOOH electrode exhibited significantly better electrochemical capacitance and rate capability than Co_3O_4 electrode. However, Co_3O_4 electrode showed better cycling life than CoOOH electrode (*Chapter 3*). CoOOH electrode was applied as electrochemical sensors to detect glucose, hydrogen peroxide and hydrazine. The sensors exhibited low detection limit, rapid response and high sensitivity for the analytes, especially the sensitivity surpasses many reported values in the literature. The results clearly demonstrate the potential of CoOOH nanostructures for non-enzymatic sensors, as well as electrocatalysts for fuel cell based on glucose, hydrogen peroxide or hydrazine (*Chapter 4 & 5*). On the other hand, we fabricated a novel nanocomposite by coupling iron oxide (α-Fe_2O_3) nanotubes (NTs) and reduced graphene oxide (rGO). Several synergistic effects desirable for electrochemical capacitors were attributed to the intimate coupling of the two components. The hollow tubular α-Fe_2O_3 possesses high surface area, while the incorporation of rGO provides an efficient two-dimensional conductive pathway to allow a fast, reversible redox reaction, and thus maximize the capacitance (*Chapter 6*). Iron (III) oxyhydroxide/oxide nanosheets were prepared on iron foil by wet oxidation in an acidic medium. The electrochemical capacitance properties of the electrode were explored in three different types of electrolytes (KOH, Na_2SO_3 and Na_2SO_4). The electrode exhibited a higher areal capacitance in Na_2SO_3 and Na_2SO_4. Cycling studies revealed that iron (III) oxyhydroxide/oxide was not stable for prolonged cycling in Na_2SO_4 and underwent reductive dissolution. On the other hand, the electrode was stable in Na_2SO_3 for 2000 cycles and exhibited high areal capacitance of 0.3-0.4 F/cm^2 (*Chapter 7*).

List of Tables

Table	Table caption	Page
1.1	Characteristic length and time scales for energy carriers under ambient conditions	3
1.2	Standard equilibrium potentials in the Co/KOH system	14
1.3	Electrochemical capacitance performance of various iron oxides and iron oxide based composite materials in aqueous electrolytes	20
2.1	Mass of Co_3O_4 on Co foils heated to different temperature and durations	39
4.1	Comparison of non-enzymatic glucose sensing performance based on different electrode materials of transition metal compounds.	81
5.1	Summary of electrochemical sensing (electrooxidation) of hydrogen peroxide by various transition metal compounds.	94
5.2	Summary of electrochemical sensing of hydrazine by various transition metal compounds.	99
6.1	Electrochemical properties of various metal oxide-graphene materials composite electrodes explored in aqueous electrolytes.	105
6.2	Percentage of various oxygenated functional groups	112

List of Figures

Figure	Caption	Page
1.1	Ragone plot for various electric energy storage devices	4
2.1	SEM images of cobalt foils heated at 350 °C for (a) 8 h, (b) 16 h, (c) 24 h, (d) 48 h and 450 °C for (e) 8 h, (f) 24 h (all scale bars = 1 μm).	32
2.2	(a) XRD patterns of cobalt foil heated at 350 °C for various durations (inset) and the magnified XRD pattern of cobalt foil heated at 350 °C for 24 h, (b) XRD patterns of cobalt foil heated at 450 °C for various durations.	34
2.3	Representative Raman spectrum of the heated cobalt foil	35
2.4	(a, b) TEM images of isolated cobalt oxide nanowalls, (c) SAED of cobalt oxide nanowalls, (d) HRTEM image of cobalt oxide nanowalls	36
2.5	EDX spectrum of the Co_3O_4 nanowalls	36
2.6	(a) Wide scan XPS spectrum, (b) XPS spectrum of the O 1s region, (c) XPS spectrum of the Co 2p of Co_3O_4 nanowalls	38
2.7	CV curves of a cobalt oxide sample performed in KOH electrolyte at different concentrations of 1 M to 5 M	42
2.8	(a) CV curves of Co_3O_4 prepared at 350 °C (Co-350) and 450 °C (Co-450) for 24 h, (b) CV curves of Co_3O_4 nanowalls prepared at 350 °C for different heating durations, (c) CV curves of Co_3O_4 nanowalls at different scan rates, (d) plots of peak currents.	44
2.9	(a) Galvanostatic charge-discharge curves at different current densities for Co_3O_4 nanowalls, (b) the corresponding derived specific capacitances from discharge curves at different scan rates	46
2.10	Cycling life data at a discharge current of 0.5 mA cm^{-2}, insets shown are the charge-discharge curves of the 11th-20th cycles (left inset) and charge-discharge curves of the 1490th-1500th cycles (right inset)	47
3.1	(a) Photographs showing the appearance of a cobalt foil before (right) and after (left) NaOH treatment. (b) SEM image of Co foil before NaOH treatment. (c and d) SEM images of CoOOH nanosheet arrays grown on the Co foil at (c) low and (d) high magnification	54
3.2	(a) XRD pattern of the as-prepared nanosheet arrays on cobalt substrate. The standard XRD patterns from database JCPDS 05-0727 of cobalt and JCPDS 07-0169 of CoOOH were denoted, (b) Raman spectrum of the as-grown CoOOH nanosheet arrays. One strong peak at 499 cm^{-1} and two weaker vibrations at 575 and 634 cm^{-1} were observed, (c) FTIR spectrum of the as-grown CoOOH nanosheet arrays	56
3.3	(a) TEM image of some isolated CoOOH nanosheets isolated from Co foil, (b) the corresponding SAED pattern and (c) typical HRTEM image. (d) The corresponding electron dispersive X-ray spectrum of the nanosheets	57
3.4	(a) Evolution of solution color during the growth of CoOOH on cobalt foil in 2.5 M NaOH solution monitored at various intervals; and (b) the corresponding UV-Vis spectra	58
3.5	SEM images of the as-synthesized CoOOH nanosheet arrays before (a & b) and after (c & d) heat treatment at 300 °C for 4 h. The images were	61

taken at the same spot of sample before and after heat treatment. (e) Low resolution TEM image showing the porosity and (f) HRTEM showing the lattice planes of the resultant Co_3O_4 product. Inset shows the SAED pattern

3.6 Comparison of the (a) XRD patterns, (b) Raman spectra and (c) FTIR spectra of CoOOH nanosheets (before heat treatment) and Co_3O_4 sample (after heat treatment). The XRD patterns were indexed to Co (JCPDS 05-0727), CoOOH (JCPDS 07-0169) and Co_3O_4 (JCPDS 43-1003) 63

3.7 XPS measurements of Co 2p3/2 (upper spectra) and O 1s (lower spectra) core levels for CoOOH (a and c) and Co_3O_4 (b and d) nanosheet arrays, respectively 65

3.8 CVs obtained using CoOOH (a) and Co_3O_4 (b) electrodes in NaOH electrolyte of different concentrations scanned at 10 mV/s. 66

3.9 CVs of CoOOH electrode in 0.5 M NaOH (a) and Co_3O_4 electrode in 3 M NaOH electrolyte (b) scanned at different scan rates; (c) Cathodic peak currents I_{pc1} and I_{pc2} of CoOOH obtained at different scan rates were plotted against (scan rate)$^{1/2}$ and scan rate, respectively, and their corresponding linear curves; (d) Cathodic peak currents (I_p) of Co_3O_4 obtained at different scan rates were plotted against (scan rate)$^{1/2}$ and scan rate. 68

3.10 Typical galvanostatic charge-discharge profiles of CoOOH (a) and Co_3O_4 (b) electrodes at different current densities (mA/cm^2), (c) calculated areal capacitance of CoOOH and Co_3O_4 electrodes based on galvanostatic discharge profiles, (d) Capacitance retention (cycling stability) of CoOOH (at a current density of 3 mA/cm^2) and Co_3O_4 (at a current density of 2 mA/cm^2) electrodes computed from galvanostatic discharge curve for continuous 5000 cycles, (e) comparison of galvanostatic charge-discharge profiles of CoOOH electrode at different cycles, (f) comparison of galvanostatic charge-discharge profiles of Co_3O_4 electrode at cycle 100-105 and cycle 4995-5000. Note: all electrochemical studies of CoOOH electrodes were performed in 0.5 M NaOH. 70

4.1 (a) CVs of CoOOH nanosheets electrode cycled to progressively more positive potential at scan rate of 10 mV/s, and (b) CV of CoOOH nanosheets electrode cycled to 0.65 V at low scan rate of 5 mV/s. 78

4.2 (a) CVs of CoOOH electrode in the absence and presence of glucose, (b) Amperometric responses of CoOOH electrode upon the successive addition of 50 µM glucose, (c) The amperometric current plotted vs. total glucose concentration, and (d) their corresponding linear calibration curves. 80

4.3 Amperometric responses of CoOOH electrode (a, b) with the addition of 0.25 mM and 0.5 mM glucose with the absence and presence of 0.1 M NaCl (in 0.1 M NaOH), (c) to the successive addition of phosphate, (d) at different NaOH concentrations and pH. 84

5.1 (a) CVs of CoOOH electrode in the absence and presence of various concentrations of H_2O_2 (scan rate: 10 mV/s), (b) LSVs of CoOOH electrode with successive addition of H_2O_2 (scan rate: 50 mV/s), (c) amperometric current curves at CoOOH electrode with sequential addition of 0.5 mM H_2O_2 for long duration (1000 s) at different applied potentials, (d) amperometric current response at CoOOH electrode held at 0 V with sequential addition of 0.5 mM H_2O_2, (e) amperometric current 92

	response at CoOOH electrode held at 0.1 V with sequential addition of 0.1 mM H_2O_2 and (f) the corresponding linear calibration plot for (e) (All experiments were performed in 0.1 M NaOH).	
5.2	(a) CVs of CoOOH electrode in the absence and presence of N_2H_4 (scan rate: 10 mV/s), amperometric current curves at CoOOH electrode, (b) with the successive addition of 0.2 mM N_2H_4 held at 0 V, (d) with the successive addition of 0.1 mM N_2H_4 held at 0.1 V, (d) the corresponding linear calibration plots. (All experiments were performed in 0.1 M NaOH).	97
5.3	Current responses (in % with respect to Day 1) measured over a continuous 7 days with the addition of 0.4 and 0.8 mM N_2H_4.	98
6.1	UV-Vis absorption spectra of GO and rGO.	108
6.2	(a) SEM image of the α-Fe_2O_3 NTs-rGO composite, (b) higher magnification SEM image, (c) TEM image and (d) high-resolution TEM image and SAED (inset).	110
6.3	(a) XRD and (b) Raman spectrum of α-Fe_2O_3 NTs-rGO.	111
6.4	Fe 2p core-level XPS spectra of the α-Fe_2O_3 and α-Fe_2O_3 -rGO.	112
6.5	C 1s core-level XPS spectra of (a) GO and (b) α-Fe_2O_3-rGO.	113
6.6	CV curves of (a) α-Fe_2O_3 NTs, (b) α-Fe_2O_3 NTs-rGO at different scan rates and galvanostatic charge-discharge curves of (c) α-Fe_2O_3 NTs, (d) α-Fe_2O_3 NTs-rGO electrodes at different current densities in 1 M Na_2SO_4, the corresponding calculated specific capacitances based on (e) CV curves and (f) galvanostatic charge-discharge curves.	116
6.7	(a) Cycling performance of α-Fe_2O_3 NTs and α-Fe_2O_3 NTs-rGO composites at a current density of 5 A/g in 1 M Na_2SO_4, (b) Galvanostatic charge-discharge curves of α-Fe_2O_3 NTs-rGO electrode from different cycles.	118
7.1	(a) Photographs of polished Fe foil (left) and two samples after reaction in acidic KCl solution, (b) two representative Raman spectra obtained for the samples, (c, d) SEM images of the iron (III) oxyhydroxide/oxide nanosheets at different magnifications. Scale bars are equal to 1 µm.	124
7.2	CV curves of iron (III) oxyhydroxide/oxide electrode in 1 M KOH (a), 1 M Na_2SO_4 (b) and 1 M Na_2SO_3 (c) at different scan rates (10 to 200 mV/s); (d) Comparison of CV curves of iron (III) oxyhydroxide/oxide electrode in different electrolytes at 10 mV/s; (e) Areal capacitances of iron (III) oxyhydroxide/oxide electrode against scan rates in different electrolytes calculated from (a-c).	125
7.3	Galvanostatic charge-discharge curves of iron (III) oxyhydroxide/oxide electrode in 1 M KOH (a), 1 M Na_2SO_4 (b) and 1 M Na_2SO_3 (c) at different current densities; (d) Areal capacitances of iron (III) oxyhydroxide/oxide electrode in 1 M Na_2SO_4 and Na_2SO_3 against current densities.	126
7.4	CV curves of iron (III) oxyhydroxide/oxide electrode at different cycles in 1 M Na_2SO_4 (a) and a photograph showing the change of electrolyte color after 200 cycles (b); CV curves of iron (III) oxyhydroxide/oxide electrode in 1 M Na_2SO_3 at different cycles (c) and the corresponding areal capacitance retention against cycle numbers.	128

List of Abbreviations

AAO	anodic aluminum oxide
BE	binding energy
CNTs	carbon nanotubes
CV	cyclic voltammetry
ECs	electrochemical capacitors
EDL	electric double layer
EDLCs	electric double layer capacitors
EDX	energy-dispersive X-ray spectroscopy
EG	exfoliated graphite
EXAFS	extended X-ray absorption fine structure
FTIR	Fourier transform infrared spectroscopy
GO	graphene oxides
GO_x	glucose oxidase
GS	graphene sheets
HEVs	hybrid electric vehicles
HRTEM	high resolution transmission electron microscope
JCPDS	Joint Committee on Powder Diffraction Standards
LSV	linear sweep voltammetry
NTs	nanotubes
rGO	reduced graphene oxides
SAED	selected area electron diffraction
SEM	scanning electron microscope
TEM	transmission electron microscope
UV-Vis	Ultraviolet–visible spectroscopy
VLS	vapor-liquid-solid
XANES	X-ray absorption near edge structure
XPS	X-ray photoelectron spectroscopy
XRD	X-ray diffraction

List of Publications

First-author publications

1. Lee, K. K., Loh, P. Y., Sow, C. H., & Chin, W. S. CoOOH nanosheet electrodes: Simple fabrication for sensitive electrochemical sensing of hydrogen peroxide and hydrazine. *Biosensors and Bioelectronics,* **2013***, 39*, 255-260. **(Chapter 2 & 5)**

2. Lee, K. K., Loh, P. Y., Sow, C. H., & Chin, W. S. CoOOH nanosheets on cobalt substrate as a non-enzymatic glucose sensor. *Electrochemistry Communications,* **2012**, *20*, 128-132. **(Chapter 4)**

3. Lee, K. K.#, Deng, S.#, Fan, H. M., Mhaisalkar, S., Tan, H. R., Tok, E. S., Loh, K. P., Chin, W. S, Sow, C. H. α-Fe_2O_3 nanotubes-reduced graphene oxide composites as synergistic electrochemical capacitor materials. *Nanoscale,* **2012**, *4*, 2958-2961. (# equal contribution). **(Chapter 6)**

4. Lee, K. K., Ng, R. W. Y., She, K. K., Chin, W. S., Sow, C. H. Vertically aligned iron (III) oxyhydroxide/oxide nanosheets grown on iron substrates for electrochemical charge storage. *Materials Letters*, 2014, *118*, 150–153. **(Chapter 7)**

First-author manuscripts submitted or in preparation

5. Lee, K. K., Chin, W. S., Sow, C. H. Cobalt-based compounds and composites as electrode materials for high-performance electrochemical capacitors (a review). *Submitted.*

Co-author contributions

6. Teoh H. F., Dung P., Lim W. Q. , Chua J. H, Lee, K. K., Hu Z., Tan H. R., Tok E. S., Sow C. H. Microlandscaping on Graphene Oxide Film via Localized Decoration of Ag Nanoparticles. *Nanoscale* **2014**, accepted, DOI: 10.1039/C3NR05373C.

7. Wei, D., Xie L., Lee, K. K., Hu Z., Tan, S., Chen, W., Sow, C. H., Chen, K., Liu, Y., Wee, A. T. S. Controllable unzipping for intramolecular junctions of graphene nanoribbons and single walled carbon nanotubes. *Nature Communications,* **2013**, 4, 1374.

8. Xie, X. N., Lee, K. K., Wang, J., & Loh, K. P. Polarizable energy-storage membrane based on ionic condensation and decondensation. *Energy & Environmental Science,* **2011**, *4*, 3960-3965. (Highlighted by *Nature*, Energy technology: Supersizing a supercapacitor, **2011**, 477, 9; Top ten most-read *EES* articles in October 2011)

9. Xie, X. N., Wang, J., Lee, K. K., & Loh, K. P. Supercapacitive energy storage based on ion-conducting channels in hydrophilized organic network. *Journal of Polymer Science Part B-Polymer Physics,* **2011**, *49*, 1234-1240.

10. Xie, X. N., Lee, K. K., Chen, X. H., Loh, K. P., Sow, C. H., Wee, A. T. S. New scenarios of charge transport in PEDT:PSS conducting polymer: From hole resonant tunneling to cationic motion and relaxation. *Organic Electronics,* **2010***, 11*, 1432-1438.

11. Xie, X. N., Lim, S. X., Wang, Y. Z., Gao, X. Y., Lee, K. K., Sow, C. H., Chen, X., Loh, K. P., Wee, A. T. S. A Nanosegregant Approach to Superwettable and Water-Attracting Surfaces. *Macromolecular Chemistry and Physics,* **2010**, *211*, 2187-2192.

12. Xie, X. N., Wang, Y. Z., Gao, X. Y., Lee, K. K., Sow, C. H., Loh, K. P., Wee, A. T. S. Embedded organic hetero-junction and negative-differential-resistance photocurrent based on bias-assisted natural-drying of organic drops. *Organic Electronics,* **2010**, *11*, 1543-1548.

13. Yusof, A. M., Lee, K. K., Ibrahim, Z., Majid, Z. A., & Nizam, N. A. Kinetic and equilibrium studies of the removal of ammonium ions from aqueous solution by rice husk ash-synthesized zeolite Y and powdered and granulated forms of mordenite. *Journal of Hazardous materials,* **2010**, *174*, 380-385.

14. Tang, Z., Poh, C. K., Lee, K. K., Tian, Z. Q., Chua, D. H. C., & Lin, J. Y. Enhanced catalytic properties from platinum nanodots covered carbon nanotubes for proton-exchange membrane fuel cells. *Journal of Power Sources,* **2010**, *195*, 155-159.

List of Conference Presentations

1. Lee, K. K., Loh, P. Y., Sow, C. H., Chin, W. S. Cobalt oxyhydroxide nanosheets as sensitive electrochemical sensors. The 7th International Chemical Conference (**SICC**) and 12th Asia Pacific International Symposium on Capillary Electrophoresis and Microscale Separation and Analysis (**APCE**), 16-19 December 2012, University Town, National University of Singapore, Singapore.

2. Loh, P. Y., Lee, K. K., Sow, C. H., & Chin, W. S. Co-Al layered double hydroxides nanowire-nanoflakes and its pseudocapacitance. The 7th International Chemical Conference (**SICC**) and 12th Asia Pacific International Symposium on Capillary Electrophoresis and Microscale Separation and Analysis (**APCE**), 16-19 December 2012, University Town, National University of Singapore, Singapore.

3. Lee, K. K., Deng S., Chin, W. S., Sow, C. H. Fe_2O_3 nanotubes-reduced graphene oxide composites as synergistic electrochemical capacitor materials. International Conference of Young Researchers on Advanced Materials (**ICYRAM 2012**), 1-6 July, 2012, Biopolis, Singapore.

4. Lee, K. K., Loh, P. Y., Mak, W. F., Srinivasan, M.[4], Mhaisalkar, S., Chin, W. S., Sow, C. H. Oriented growth of CoOOH and Co_3O_4 nanosheets on cobalt substrates for renewable energy. International Conference on Materials for Advanced Technologies (**ICMAT 2011**), 26 Jun-1 July, 2011, Suntec, Singapore.

5. Lee, K. K., Sow, C. H. Fabrication of one-dimensional CuO nanostructures by direct heating of Cu-sputtered silicons and their field emission properties, The 2008 Asian Conference on Nanoscience and Nanotechnology (**AsiaNANO 2008**), Nov 3-6, 2008 Biopolis, Singapore.

Chapter 1 – Introduction

1.1 The role of nanoscience in renewable energy

The decreasing availability of fossil fuels, as well as environmental and ecological effects (e.g. CO_2 emission) due to the combustion of fossil fuels, require society to move towards green, renewable and sustainable energy resources[1, 2]. At current stage, 80 % of the global primary power consumptions (14 terawatt) are coming from the CO_2-emitting fossil fuel of oil, coal and natural gas[3]. Less than 1 % of power consumptions are coming from carbon-free renewable power sources such as geothermal, wind and solar power. Global temperature raise, associated with the CO_2 emission, results in irreversible and serious threats to the various aspects of environment with adverse impact on human health, agriculture, water resources and so on. Realization of carbon-free energy resources requires a massive effort on the research and development of new technologies and solutions. Advancements in nanoscience and nanotechnology possess a good potential to solve these various aspects of the energy problems.

As the length scales for energy carriers (photons, electrons, phonons, molecules/ions) in different phases are generally of the order of 1 to 100 nm (Table 1), revolutionary improvements in the energy delivery can be achieved by innovating nanoscale design of materials, energy conversion processes and systems [4-8]. For instance, in the case of nanoscale materials, quantum confinement of electronic particles in nanocrystals produces unique electronic and optical properties that can be further utilized to improve the power efficiency of photovoltaic solar cells[5]. The use of appropriate nanoscale building blocks, void space and deliberate disorder to integrate a multifunctional three-dimensional nanoarchitecture for energy storage devices, enabling the small areal footprint and accompanying improvement in power and energy density[7]. Certainly not all energy technologies can be improved by nanoscience (e.g. wind and hydroelectric technologies), the renewable technologies can be revolutionalized by nanoscale design are listed as below:

a.) *Energy conversion*: solar photovoltaics (solar cells), solar photocatalysis (solar fuels), solar thermal energy (solar thermophotovoltaic and thermoelectric conversion), electrochemical energy (fuel cells).

b.) *Energy storage*: biochemical storage (biofuels), chemical storage (hydrogen), electrochemical storage (batteries and capacitors).

c.) *Energy conservation*: thermoelectrics, thermal insulation and thermal management, solid state lighting.

d.) *Environmental aspects of energy*: carbon dioxide capture and storage (CCS).

Table 1.1. Characteristic length and time scales for energy carriers under ambient conditions[3].

	Wavelength (nm)	**Mean free path (nm)**	**Relaxation time (ns)**
PHOTONS (solar/ thermal radiation			
• in liquid/ gases	~100–30,000 ^{a}	>1000 ^{b}	$>10^{-6}$
• in semiconductors	~25–30,000 ^{a}	>10 ^{b}	$\sim10^{-7}$–10^{-6}
• in conductors/ metals	–	~0.1–10 ^{b}	$\sim10^{-10}$–10^{-9}
ELECTRONS			
• in semiconductors/ dielectrics	~1–50	~1–500	$\sim(1–10) \times 10^{-3}$
• in conductors/ metals	~0.1–1	~1–10	$\sim(10–100) \times 10^{-6}$
PHONONS			
• in semiconductors/ dielectrics	~0.5-10	~1-500	$\sim10^{-3}$–1
MOLECULES/ IONS			
• in gas/ plasma	10^{-2}–1 ^{c}	$\sim10^{3}$-10^{7}	~1-100
• in liquid/ electrolyte	–	~0.1–1	$\sim10^{-3}$
• in solid/ electrolyte	–	~0.1–1	$\sim10^{-3}$

^{a} refers to exciton electronic-vibration modes. ^{b} refers to skin penetration depth. ^{c} refers to de Broglie wavelength).

1.2 Electrochemical storage: electrochemical capacitors

In parallel with the development of energy generation from renewable resources such as wind and solar, efficient electrochemical energy storage systems such as batteries and electrochemical capacitors are present at the forefront [9-19]. These electrochemical storage technologies have been profoundly benefited by nanoscience, particularly in the design and fabrication of advanced nanomaterials[8, 20-32]. Electrochemical capacitors (ECs) are also commonly referred to as supercapacitors or ultracapacitors. These are power devices that can be fully charged and discharged in seconds. In a Ragone plot (a plot of specific power vs. specific energy) as shown in Figure 1, ECs fall in the gap between batteries and conventional capacitors (e.g. electrolytic capacitors or metalized film capacitors)[26]. ECs' energy density is lower than those in batteries but a much higher power density can be achieved for shorter time. This feature highlights their role in complementing batteries in energy storage such as uninterruptible power supplies and load-leveling. Besides, ECs are expected to enhance batteries and fuel cells in the hybrid electric vehicle (HEVs) to provide the power for acceleration and recovery of brake energy[9].

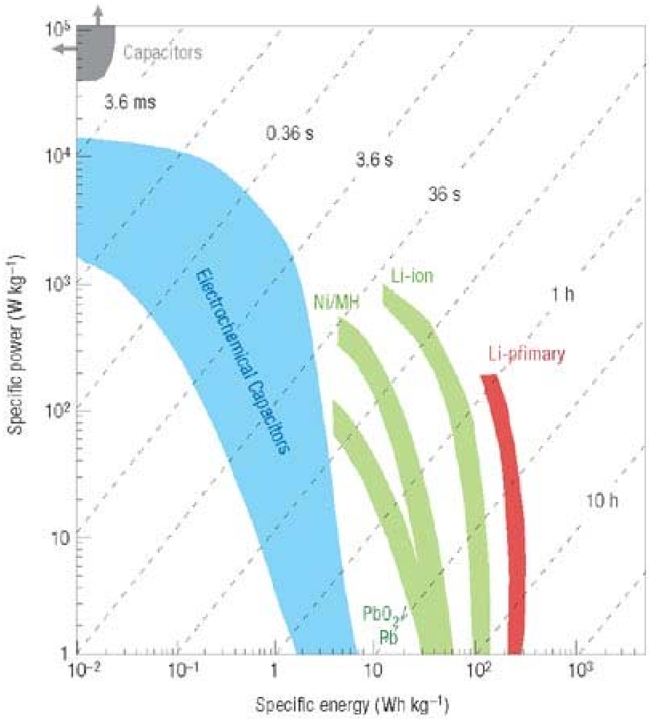

Figure 1.1. Ragone plot for various electric energy storage devices[26]. Reprinted by permission from Macmillan Publishers Ltd: P. Simon and Y. Gogotsi, *Nat. Mater.*, 2008, **7**, 845-854, copyright (2007).

1.2.1 Electric double layer capacitors (EDLC) vs. pseudocapacitors

ECs store energy using either ion adsorption (electric double layer capacitance) or fast surface redox reactions (pseudocapacitance/ redox capacitance)[26]. Electric double layer capacitors (EDLCs) are mostly based on high surface area carbon materials. EDLCs store the electric charge directly across the double layers of the electrode. The mechanism of surface charge generation can be generalized as: surface dissociation, ion adsorption from solution and crystal lattice defect. As charges builds up on the electrode surface, ions of the opposite charge build up in the electrolyte near the electrode/ electrolyte interface in order to provide electroneutrality.

Pseudocapacitors use fast, reversible, and potential-dependent faradaic reactions on the electrode surface or near surface for charge storage. When a potential is applied to a pseudocapacitor, current is induced from three types of processes: 1) reversible electrosorption, 2) oxidation-reduction (redox) of transition metal oxides, and 3) reversible electrochemical doping-dedoping in conductive polymers [33]. Pseudocapacitance behavior can be identified using cyclic voltammetry (CV). Materials with pure double-layer capacitance exhibit parallelogram-shaped CV curves while irregular peaks are observed for pseudocapacitive materials. Pseudocapacitance can be superimposed on any electric double layer (EDL) capacitance. Hence pseudocapacitors can provide a higher energy density than EDLCs, for instance in some transition metal oxides, multiple oxidation states can be accessed.

Operation of EDLCs is based on physical charge storage, so there is no associated chemical and phase changes during cycling, resulting in a highly reversible storage mechanism where cycling stability is greater than 10^6. Pseudocapacitive materials undergo physical changes (e.g. dissolution of manganese oxides in electrolyte) during prolonged charge/ discharge cycles, they have relatively poorer durability than EDLCs.

1.2.2 *Research trends in development of the electrode materials for electrochemical capacitors (ECs)*

One of the key challenges for ECs is the limited energy density, which hindered their wider applications. In order to improve the ECs' performance substantially to fulfill the higher requirement of future systems ranging from portable electronics to hybrid electric vehicles and industrial equipments, development of novel and advanced electrode materials is crucial. Two key research directions in EC electrode materials development are:

1.) ***Nanostructured materials***

Nanostructured materials are becoming increasingly important for electrochemical energy storage to achieve notable improvement in performance. Various nanostructures such as nanowires, nanotubes, nanospheres, nanosheets and so forth have been explored. The advantages of nanostructured materials can be summarized as below [29, 33] :

a.) Reduced dimensions of the nanostructures can provide higher specific surface area, thus significantly enlarge the electrode-electrolyte contact area per unit mass, and provide more ion adsorption sites or electroactive reaction sites and charge-transfer reactions. Porosity and pore size distribution in certain materials can be engineered to optimize the electrode-electrolyte interactions.

b.) Reduction of the tortuous ionic and electronic diffusion distance through porous and nanostructured electrodes, leading to shorter transport or diffusion times and thus fast kinetics and high rate charge-discharge capability. Three dimensional nanoarchitectures are examples to maximize the accessible surface area and the kinetics of electrode-electrolyte interactions.

c.) The confinement of material dimensions to the nanoscale in the electrodesresults in deviations from their equilibrium structure and modifies phase transformations upon ion insertion/extraction reactions. Improved cycling performance can be observed by minimizing the pulverization problem of electrode materials, as well as by enhancing the mechanical strength to ease strain and structural distortion.

2.) *Nanohybrid materials*

Different forms of nanohybrid materials such as nanocomposites, mixed oxides, nanoheterostructures, etc. can be prepared via various physical and chemical methods. The rationale is to tackle problems of the individual components and combine the advantages of all components. Based on the different choices of materials, synergistic effects can be achieved through minimizing particle sizes, minimizing clustering and agglomerations of particles, increasing the electrochemically accessible area, facilitating electron and proton conduction, extending the potential window, enhancing the mechanical strength and stability, introducing additional pseudocapacitance, improving cycling stability and rate capability. However it should be noted that rational structural design and optimum ratio of the respective components of the nanohybrids are important to ensure the maximum synergistic effects.

1.3 Transition metal oxides/ oxyhydroxides nanostructures in electrochemical sensing

Electrochemical sensors are the devices composed of an active sensing material with a signal transducer based on principles of electrochemistry. Electrochemical sensors are electrochemical systems that employ two or three-electrode arrangement. The applied current or potential for electrochemical sensors may be varied to enhance the sensitivity and selectivity of the sensor. Based on the type of electrical signals, electrochemical sensors generally can be categorized as conductivity/ capacitance, potentiometric, amperometric, and voltammetric sensors. Within these sensors, the active sensing material on the electrode acts as a catalyst that catalyzes the reaction of particular analytes (chemical or biochemical compounds) to obtain the output electrical signals[34].

In recent years, much effort have been made to utilize various nanostructures such as nanowires, nanoparticles and nanotubes for new electrode development. Nanostructured materials offer efficient transport of electrons and optical excitation, making them beneficial for the integration of nanoscale devices. Compared to conventional macroelectrodes, nanostructures display several unique advantages when used for electrochemical analysis: enhancement for mass transport, catalysis, high effective surface area and control over electrode microenvironment[35, 36]. Nanostructured electrode allows a higher rate of mass transport to the surface of the electrode. Thus, the catalytic properties of some nanostructures can decrease the overpotential needed for an electrochemical reaction to become kinetically viable, leading to a more reversible reaction. Furthermore, the enhanced catalytic and mass transport properties are dominating the peak potential, causing a change in the voltammetry peak potential associated with analytes of interest. This feature can improve the selectivity of electroanalysis by separating from the peaks due to common interferences.

Electrochemical glucose biosensors based on glucose oxidase (GO_x) are the most important electrochemical sensors invented since 1960s and they served as a model to inspire further developments for other types of electrochemical biosensors[37]. In recent years, various nanomaterials such as metal oxides, carbon nanotubes, and various nanocomposites were employed as immobilization hosts for enzymes to enhance the sensitivity and selectivity of the sensors. However, enzyme-based electrochemical sensors suffered from various disadvantages such as complicated enzyme immobilization, delicate operating conditions (temperatures below 44°C, ambient humidity levels and pH ranges of 2-8), chemical instability and high cost[38].

In order to overcome the drawbacks of enzymatic electrode, non-enzymatic electrochemical glucose sensors are introduced as a new generation glucose sensors. In overall, non-enzymatic glucose sensors offer advantages of stability, simplicity, reproducibility and free from oxygen limitation[39]. Non-enzymatic sensors avoid the need of facilitating a delicate enzyme. They operate by directly oxidizing glucose or other relevant analytes in the samples. The main problems hindering the commercial applications of these types of sensors are the lack of selectivity at the electrode, the slow kinetics of glucose oxidation, fouling of the electrode by real sample constituents, and the non-applicability of the systems in physiological pH[38].

In the earlier stage of research, materials of (i) inert noble metals, e.g. Pt, Au; (ii) metal alloys containing noble metals such as Pt, Au, Ir, Ru and Pd; and (iii) noble metal-dispersed in carbon nanotubes (CNTs) framework were used as non-enzymatic glucose sensors. However, these materials are unsatisfactory in terms of sensitivity and selectivity, high cost, quick loss of activity by adsorption and accumulation of intermediates or chloride ions[40]. Beside reducing the cost significantly, base transition metal oxides or hydroxides (e.g CuO, NiOOH, NiO,

Co_3O_4) are found to be able to catalyze the direct oxidation of glucose. These materials exhibit very high sensitivity (as high as $mAmM^{-1}cm^{-2}$) among the non-enzymatic electrode materials, as well as free from chloride ion poisoning. However, transition metal oxides electrode is prone to low selectivity. The oxidation potential is indiscriminate against other electroactive species such as ascorbic acid, uric acid and other types of sugar in the samples. Consequently, there remains opportunity for further improvement and development for this type of electrode materials.

1.4 Oxidation routes to in situ growth of nanostructures

Corrosion is defined as an irreversible interfacial reaction of a material with its environment, resulting in the loss of material or in the dissolution of one of the constituents of the environment into the material[41]. The annual cost of corrosion in the United States was US$276 billion in 2001 and accounted for ~3.2 % of the nation's gross domestic product[42]. Corrosion caused a terrible waste of natural resources and may cause all types of unacceptable ecological damage, thus tremendous efforts have been made to reduce the huge cost of corrosion, particularly on metal protection.

Most metals are not thermodynamically stable in contact with the environments (e.g. atmosphere or water), thus they should spontaneously corrode since the corroded state is the more stable state. Thus in nature, metals are found in their oxidized state as oxide or sulfide minerals. An oxidation reaction takes place when a metal combines with atoms or with a molecular group and loses electrons, or when it is transposed from one valency to a higher one[43].

Basically, corrosion can be categorized into two types: dry corrosion and wet corrosion. Dry corrosion takes place in the absence of conducting (aqueous) medium. An example of dry corrosion is the reaction between metal and oxygen (atmosphere) at elevated temperatures in perfectly dry conditions. The differences in the rate of dry corrosion vary from metal to metal as a result of the mechanisms involved. The oxidation rates also depend on the conductivity of the oxides because ions have to move through the oxide layer. Dry corrosion occurs faster as temperature increases due to an increase in the mobility of ions within the oxide layer. The basic reaction involved in dry corrosion is:

$$M \rightarrow M^{n+} + n \times e^{-1}$$

where M is a metal element. The metal loses electrons to form an ion and free electrons. The ionic species can react with oxygen in the air to form a metal oxide.

Wet corrosion of metals occurs through electron transfer in an electrochemical cell, involving two half-cell reactions, oxidation (anodic reaction) and reduction (cathodic reaction). At the anode, the metals lose electrons when they are oxidized to ions. At the cathode, the surrounding environment (other metal, liquid or gas) then gains the electrons in reduction. In wet corrosion, an electrolyte must be present to allow for migration of ions between the cathode and anode and participate in the formation of corrosion products.

Anode: $M \rightarrow M^{n+} + n \times e^{-1}$

Cathode: $O_2 + H_2O + 4e^- \rightarrow 4OH^-$ or $2H^+ + 2e^- \rightarrow H_2$

Metal corrosion is influenced by various factors such as oxygen content, ion concentration, atmosphere, pH value, temperature, presence of other elements, ions or compounds. The corrosion process may be utilized to fabricate functional nanostructured materials by controlling the environment and the reaction between a metal with the environment. In an appropriately designed environment, controlled metal corrosion provides a sustainable supply of metal ions for nanostructures growth directly on the metal substrate.

Classically, nanostructure arrays were fabricated by the use of templates such as anodic aluminum oxide membrane (AAO)[44]. Although the template method is general, the removal of template is a cumbersome process and often accompanied with contamination or aggregation of nanostructure arrays. Besides, vapor-liquid-solid (VLS) is another method of choice to fabricate nanostructure arrays on substrates[45]. However, the VLS approaches require catalyst and high temperature with more complicated setup. In comparison, metal corrosion or oxidation routes offer a simpler synthesis method without templates and catalysts to fabricate nanostructure arrays on metal substrates. Importantly, the conductive metal substrates hosting the nanostructures provide a convenient path way for electrical addressing, control, and detection. This feature has allowed exploration of their potential applications in diverse areas such as field electron emission, electrochemical energy storage (e.g. Li-ion batteries, electrochemical capacitors), photoelectrochemical applications (e.g. water splitting), electrocatalysis, sensing etc. Some examples prepared by this synthesis strategy were reviewed by Yang *et. al.*[46] and Han *et. al.*[47].

1.5 Properties of cobalt compounds relevant to electrochemical applications

1.5.1 Electrochemical capacitance and electrochemistry of cobalt compounds

Early electrochemical studies on cobalt hydroxide or oxide electrodes were motivated by the chemical similarities between cobalt and nickel[48, 49]. The utilization of pseudocapacitance from transition metal oxides for electrochemical energy storage was demonstrated by the pioneering work of Conway and co-workers in 1990s[50-52]. In 1997, Srinivasan and Weidner electrodeposited metal hydroxide films followed by heating in air to obtain porous metal oxide films[53]. Cobalt oxides electrodes exhibited a specific capacitance of ~10 F/g based on a two-electrode device. High surface area cobalt hydroxide xerogel powder were prepared by Lin et al.[54] in 1998 using a sol-gel process. Amorphous $Co(OH)_2$ heated at 150 °C exhibited the highest surface area (198 m^2/g) and largest pore volume (0.43 cm^3/g), thus presenting the highest capacitance of 291 F/g. The capacitance was attributed to a surface redox mechanism, considering the one-electron exchange redox reaction taking place on the particle surfaces.

The electrochemical reactions and formation of different cobalt phases at the cobalt-compound electrodes can be interpreted by comparing the equilibrium potentials of the current peaks with those calculated from thermodynamics and potential-pH diagram (Pourbaix diagram)[55-57]. The electrode potentials calculated by Behl and Toni[58] as well as the half cell reactions were presented in Table 1.2. In the lower potential range, the redox reaction should be related to Co(II)/ Co(III) system. At higher potential preceding oxygen evolution reaction (OER), the Co(III)/ Co(IV) should predominate. Notably, the oxidation peak of $CoOOH \rightarrow CoO_2$ is often hidden by the polarization curve of OER[58-60].

Table 1.2. Standard equilibrium potentials in the Co/KOH system[58].

Electrode couple	Half-cell reaction	V vs. Hg/HgO
$Co(OH)_2/Co_3O_4$	$3Co(OH)_2 + 2OH^- \leftrightarrow Co_3O_4 + 4H_2O + 2e-$	-0.192
CoO/Co_3O_4	$3CoO + 2OH^- \leftrightarrow Co_3O_4 + H_2O + 2e-$	-0.369
$Co(OH)_2/CoOOH$	$Co(OH)_2 + OH^- \leftrightarrow CoOOH + H_2O + e-$	-0.054
CoO/CoOOH	$CoO + OH^- \leftrightarrow CoOOH + e-$	-0.172
$Co_3O_4/CoOOH$	$Co_3O_4 + OH^- + H_2O \leftrightarrow 3CoOOH + e-$	+0.222
$Co(OH)_2/CoO_2$	$Co(OH)_2 + 2OH^- \leftrightarrow CoO_2 + 2H_2O + 2e-$	+0.254
CoO/CoO_2	$CoO + 2OH^- \leftrightarrow CoO_2 + H_2O + 2e-$	+0.195

The redox reactions involved at $Co(OH)_2$ and Co_3O_4 electrodes in alkaline electrolytes can be generalized as below:[58-69]

For $Co(OH)_2$: $Co(OH)_2 + OH^- \leftrightarrow CoOOH + H_2O + e^-$ (1)

$CoOOH + OH^- \leftrightarrow CoO_2 + H_2O + e^-$ (2)

For Co_3O_4: $Co_3O_4 + H_2O + OH_- \leftrightarrow 3\ CoOOH + e^-$ (3)

$CoOOH + OH^- \leftrightarrow CoO_2 + H_2O + e^-$ (2)

1.5.2 Oxidation mechanism of different cobalt compounds and topotactic relationship

Understanding of the oxidation mechanism[1,70-72] between different cobalt compounds is crucial due to two reasons: 1.) the synthesis of cobalt oxide and oxyhydroxide nanomaterials often involve the transformation of intermediate phases such as cobalt hydroxide,[73-86] cobalt oxyhydroxides,[87-89] and cobalt carbonates;[78] 2.) the oxidation mechanism is relevant to the electrochemical cycling rate and stability, as well as thermal stability of the electrodes.

Benson et al.[80] observed the phase transition of blue $Co(OH)_2$ (α form) to black CoOOH via anodic oxidation, while atmospheric oxidation of blue $Co(OH)_2$ in

KOH solution yielded brown CoOOH. The different forms of CoOOH were possibly due to two different types of mechanism: 1.) nucleation of new phase via a solution intermediate corresponding to the slow atmospheric oxidation and 2.) transformation of the lattice by electron and proton migration through the solid phase corresponding to the anodic oxidation.

By isothermal heating in an air flow or water suspension, Figlarz et. al.[70] studied the solid evolution of β-$Co(OH)_2$ (rose color) to CoOOH. Isothermal heating of $Co(OH)_2$ at 60 °C in an air flow produced CoOOH particles with fine porosity and cracks. The decreased crystallite sizes deduced from the $10\bar{1}1$ based on Scherrer formula were 8, 6, 7 nm at 60, 80 and 100 °C respectively. Furthermore, the phase transformation was *topotactic* as revealed by SAED. The hexagonal unit cell axes of CoOOH were parallel to the unit cell axes of $Co(OH)_2$ although the CoOOH crystallites were more misoriented.

The oxidation mechanism via different routes was further investigated systematically[71]. The positive $Co(OH)_2$ electrode dismantled from a charged $Co(OH)_2$/Cd cell (electrolyte: 5 M KOH) over 20 h was evaluated. It was found that the oxidation reaction was biphasic. The final product was β-CoOOH particles with irregular contours. This transformation is referred as *metasomatic* process, where dissolved chemical species react on the external surface of a solid. On the other hand, chemical oxidation of $Co(OH)_2$ to β-CoOOH with NaClO (8 M) in 5 M KOH was *pseudomorphic*, the phase change did not change the particle morphology. Accordingly, a single particle domain consisted of several slightly disoriented coherent diffraction domains. In addition, SAED pattern of partly transformed particles indicated the topotactic relationship between the $Co(OH)_2$ precursor and oxidized β-CoOOH product: the [001] and [110] axis directions of the β-$Co(OH)_2$

phase were parallel to the [003] and [110] directions of the β-CoOOH phase, respectively. Both pseudomorphic retention and topotactic relationship implied that the reaction most likely occurred in the solid state. The mosaic texture was due to the induced strain within the particles during solid state growth caused by the unit cell mismatch between the β-$Co(OH)_2$ and β-CoOOH.

Chemical oxidation of $Co(OH)_2$ in 5 M KOH under hydrothermal condition (oxygen pressure of 20 bar) produced hexagonal β-CoOOH with irregular contours possessed high porosity and granular internally. The oxidation reaction followed in two steps: 1.) partial dissolution of $Co(OH)_2$ and growth step of CoOOH on the external part or grain boundaries of the partially dissolved Co(OH); 2.) the initial platelet core undergoing solid state transformation which involved a proton diffusion process. The misfit due to strain produced an internal mosaic structure.

Based on XRD result, CoOOH was totally decomposed to Co_3O_4 by heating in air at 250 °C.[72] The major morphology of the CoOOH was retained, however the inhomogeneous porosity of CoOOH turned to Co_3O_4 of regular porosity with tiny round pores. According to SAED pattern, the thermal transformation was a topotactic reaction with [001] and [111] axis directions of CoOOH phase parallel to [110] and [110] axis directions of Co_3O_4 phase. Moreover, the {110} CoOOH reflections were not separated from the {440} Co_3O_4 reflections due to the very close value of their interplanar spacings (1.425 Å for CoOOH d_{110} and 1.429 Å for Co_3O_4 d_{440}).

Additional to topotactic relationship of the $Co(OH)_2 \rightarrow CoOOH$ and $CoOOH \rightarrow Co_3O_4$, topotactic transformation of $Co(OH)_2 \rightarrow CoO$[90] and $Co(OH)_2 \rightarrow Co_3O_4$[84, 91] has also been reported. β-$Co(OH)_2$ has a brucite-like layered structure with a interlayer spacing of 4.65 Å, while spinel Co_3O_4 has cubic structure with 3-fold symmetry viewed along [111]. Thus, β-$Co(OH)_2$ to Co_3O_4 transition is topotactic with the relationship [001] $Co(OH)_2$//[111] Co_3O_4.

1.6 Iron oxides/ oxyhydroxides in electrochemical capacitors

Table 1.3 summarizes the reported electrochemical capacitance performances of various iron oxide and iron oxide-based composite materials in aqueous electrolyte. As far as the electrolytes are concerned, in comparison with organic electrolytes, aqueous electrolyte used in ECs have the advantages of high ionic conductivity, low cost, non-flammability, good safety, and convenient assembly in air. Prior studies on the electrochemical capacitance of various iron oxide or hydroxide based electrodes in aqueous electrolytes have reported the specific capacitances ranging from 5 to 150 F/g. A few exceptions were reported by Wu *et al.* [92] and Zhitomirsky *et al.*[93] Zhitomirsky *et al.* [93] achieved high specific capacitance of 210 F/g for porous γ- Fe_2O_3 in $Na_2S_2O_3$ electrolyte, under very strict conditions: at very low weight loading of 0.1 mg/cm^2. Wu *et al.* [92] achieved a specific capacitance of 170 F/g for electroplated Fe_3O_4 granules in Na_2SO_3 electrolyte. Sulfite based aqueous electrolyte is not ideal for asymmetric ECs due to interference from the electrochemical oxidation of the sulfite anion, which will limit the available potential window at the positive electrode of an asymmetric EC[94]. Moreover, iron oxide-based ECs commonly suffered from cycling stability due to the reductive dissolution of the iron oxides when cycled to progressively negative potentials, especially when weak acidic Li_2SO_4 electrolyte was used[94-97]. Long *et al.* proposed the use of borate-buffered Li_2SO_4 to reduce this problem[94].

To further optimize the capacitance, cycling stability, and high rate property of iron oxide compounds, it is a current research trend to fabricate composites of iron oxides with electroactive and conducting materials (e.g. conducting polymers and carbon nanomaterials). Zhao *et al.*[98] demonstrated that by treating Fe_3O_4 nanowires with pyrrole, the specific capacitance in 0.1 M Na_2SO_3 electrolyte can be improved from 106 F/g to 190 F/g, as well as better capacitance retention upon 500 cycles (from 75 % to 84 %). In addition, PANI-Fe_3O_4 in 1 M H_2SO_4 electrolyte was able to exhibit high specific capacitance of 213 F/g and 146 F/g at current density of 1 mA/cm^2 and 5 mA/cm^2. However, the capacitance was found to reduce to 85 % after 300 cycles, probably due to the unfavorable strong acidic electrolyte. Most recently, Yan *et al.*[99] reported a markedly high specific capacitance of 890 F/g and 480 F/g at current density of 1 A/g and 5 A/g, respectively, for the spray deposited Fe_3O_4-rGO composite.

Wu and co-workers studied the capacitance mechanisms of electroplated Fe_3O_4 in aqueous electrolytes of Na_2SO_3, Na_2SO_4 and KOH by electrochemical quartz-crystal microbalance (EQCM) analysis, cyclic voltammetry (CV) and X-ray photoelectron spectroscopy (XPS)[92]. The Fe_3O_4 thin film electrode presented specific capacitances of ~170, 25 and 3 F/g in 1 M Na_2SO_3, Na_2SO_4 and KOH respectively. Strong specific adsorption of anions from all the electrolytes onto the electrode was evidenced by static EQCM study. Both the sulfate and sulfite anion played a much more important role in specific adsorption than sodium cation. Based on the combined results, the pseudocapacitance of Fe_3O_4 electrode in Na_2SO_3 in the potential range of -0.8 to -0.1 V (vs. Ag/AgCl) was attributed to the successive reduction of the absorbed sulfite ions and their reverse oxidation, in addition to electric double layer capacitance (EDLC). For Fe_3O_4 electrode in Na_2SO_4, the EDLC mechanism was operative for the applied potential range of -0.15 to 0.45 V (vs.

Ag/AgCl). On the other hand, the small capacitance of Fe_3O_4 in KOH was due to the surface oxidation of Fe_3O_4 to form an insulating Fe_2O_3 layer.

In addition, *in situ* X-ray absorption spectroscopy under electrochemical control was performed by Long's group to elucidate the charge-storage mechanism of the amorphous FeOOH-carbon nanofoam electrode in aqueous 2.5 M Li_2SO_4 [94]. After charging and discharging at specific potentials ranging from +0.2 to -0.8 V (vs. Ag/AgCl), the X-ray absorption near-edge structure (XANES) and extended X-ray absorption fine-structure (EXAFS) spectra for the FeOOH-carbon nanofoam electrode were collected. Upon discharging from +0.2 to -0.8 V, the edge energy shifted from 7124.12 to 7122.83 eV indicating reduction of Fe^{3+}. The change in oxidation state of Fe upon discharging is -0.29, associated to the reduction of a fraction of Fe^{3+} to Fe^{2+}. On the other hand, upon recharging the electrode from -0.8 to +0.2 V, the XANES spectra exhibited that the Fe oxidation state reversibly toggled between ~3.0 and 2.7. In sum, the XANES data revealed the pseudocapacitance of the amorphous FeOOH arises from a reversible Fe^{3+}/Fe^{2+} redox couple.

Table 1.3. Electrochemical capacitance performance of various iron oxides and iron oxide based composite materials in aqueous electrolytes.

Iron oxides	Electrolyte	V vs. Ag/AgCl	C_m (F/g)	Method	Cycle life	Ref.
Fe_3O_4 electrocoagulated powder	1 M Na_2SO_4	-0.75 to 0.50	5.3	GS 15 mA/g	--	100
Fe_3O_4 electrocoagulated powder	1 M Na_2SO_3 1 M Na_2SO_4 1 M KOH	0 to 1.2	27.0 5.7 5.3	GS 15 mA/g	2000 (78 %)	101
Fe_3O_4 precipitated powder	0.1 M Na_2SO_4	-0.80 to 0.25	75	CV 10 mV/s	--	102, 103
Fe_3O_4 electrodeposited porous film	1 M Na_2SO_4	-0.60 to 0	105	CV 20 mV/s	--	104
Fe_3O_4 electroplated granules	1 M Na_2SO_3 1 M Na_2SO_4 1 M KOH	-0.70 to -0.20	170 25 3	CV 2 mV/s	--	92
Fe_3O_4 nanoparticles	1 M Na_2SO_4	-0.08 to 0.92	82	CV 50 mV/s	1000 (~60 %)	105
Fe_3O_4 octadecahedrons	1 M Na_2SO_3	-1.28 to 0.12	118	GS 6 mA	500 (~89 %)	106
Fe_3O_4 nanoparticles Fe_3O_4 nanowires Pyrrole treated-Fe_3O_4 nanowires	0.1 M Na_2SO_3	-1.28 to -0.08	12 106 190	GS 0.1 mA/cm^2	-- 500 (~75%) 500 (~84%)	98
γ-Fe_2O_3 porous film	0.25 M Na_2SO_4 0.25 M $Na_2S_2O_3$ 0.25 M $Na_2S_2O_3$	-0.98 to -0.18	43 82 210	CV 100 mV/s CV 2 mV/s	100 (~68 %)	93
α-Fe_2O_3 electrodeposited nanosheets	1 M Li_2SO_4	-0.98 to -0.18	135	CV 10 mV/s	500 (~70 %)	95, 96
α-Fe_2O_3 mesoporous nanostructures	1 M Li_2SO_4	-0.68 to -0.08	116	GS 0.75 A/g	1000 (~74 %)	97
β-FeOOH nanocolumns	1 M Li_2SO_4	-0.93 to -0.18	116	GS 0.5 A/g	--	107
α-LiFeO2 nanoparticles	0.5 M Li_2SO_4	-0.78 to -0.08	50	CV 10 mV/s	500 (~100 %)	108
PANI-Fe_3O_4 composites	1 M H_2SO_4	-0.08 to 0.67	213	GS 1 mA/cm^2	300 (~85 %)	109
FeOOH-coated carbon nanofoams	2.5 M Li_2SO_4 Buffered 2.5 M Li_2SO_4	-0.80 to 0.20	84 72	CV 5 mV/s	200 (~58 %) 1000 (~81%)	94
Fe_3O_4 nanoparticles rGO Fe_3O_4-rGO Fe_3O_4-rGO	1 M KOH	-0.88 to 0.12	104 139 480 890	GS 5 A/g GS 5 A/g GS 5 A/g GS 1 A/g	10000 (~100 %)	99
α-Fe_2O_3 nanotubes α-Fe_2O_3 NTs-rGO	1 M Na_2SO_4	-1.00 to 0	30 216	CV 2.5 mV/s	2000 (~92%) 2000 (~100%)	Chap. 6

1.7 Objectives, scope and structure of thesis

In the past years, our research group has been working on alternative strategy to simultaneously integrate the growth and assembly of nanostructures on metal substrates. The growth of the nanostructures lies on the basic principles of dry corrosion or thermal oxidation. The important characteristic of this strategy is that the metal substrates itself is part of the precursor to sustain the nanostructure growth. The nanostructures grow as vertical arrays directly from the metal substrates. The robust connection of nanostructures on a conductive substrate allows the electrical addressing, control and detection. Versatile metal oxide nanostructures such as CuO nanowires[110], Co_3O_4 nanowires and nanowalls[111, 112], CuO-ZnO nanostructures[113], α-Fe_2O_3 nanoflakes[114, 115] and NiO nanowalls[116] were synthesized by our co-workers via thermal oxidation method, most notably by an innovative "hotplate method". Data retrieved on 24 Jan 2013 found that the seven key papers published in 2005-2008 has received an impressive citation of 723 times, confirming the scientific impact and significance of these works.

Inspired by a natural process of rusting, another colleague, Chin explored the large scale synthesis of Fe_3O_4 nanosheets by wet corrosion or wet oxidation[117]. Comparatively, wet oxidation offers several advantages compared to thermal oxidation. Thermal oxidation requires high temperatures between 300-500 °C, longer duration from hours to days and thus higher synthesis costs. In addition, by thermal oxidation in air, the end products are commonly the most thermodynamically stable oxide products such as α-Fe_2O_3 and Co_3O_4. On the other hand, by carefully exploiting the *in situ* chemistry between a metal substrate and a formulated solution, synthesis of nanostructures on metal substrates can be achieved at very low temperature, even close to room temperature. Furthermore, various phases of metal hydroxides/ oxyhydroxides/ oxides/ chalcogenides can be conveniently obtained by tuning the chemical oxidation conditions.

With this background, this thesis focuses on two main goals: (1) to further expand the potential applications of metal oxide nanostructures previously synthesized by our co-workers, especially in the emerging type of electrochemical energy storage device, namely electrochemical capacitor; (2) to develop new method to synthesize nanostructures by wet oxidation and to explore their potential electrochemical applications. The specific research activities and aims of each chapter in this thesis are summarized as below:

Chapter 2
- to investigate the electrochemical capacitances of Co_3O_4 nanowalls synthesized by a hotplate method.

Chapter 3
- to develop a new wet oxidation method for synthesizing CoOOH nanosheets at room temperature.
- to synthesize Co_3O_4 nanosheets by using CoOOH nanosheets as precursors.
- to study the comparative physical characteristics and electrochemical properties of CoOOH and Co_3O_4 nanosheets.

Chapter 4
- to evaluate CoOOH nanosheets as an electrochemical sensor for glucose.

Chapter 5
- to evaluate CoOOH nanosheets as electrochemical sensors for hydrazine and hydrogen peroxide.

Chapter 6
- to prepare α-Fe_2O_3 nanotubes and α-Fe_2O_3 nanotubes-reduced graphene oxide for electrochemical capacitors.

Chapter 7
- to study electrochemical capacitances of γ-FeOOH nanosheets in different electrolytes

Overall, this thesis is written in the form of a comprehensive account from a PhD research. At the same time, for the benefits of broader readership, each result chapter (2-7) is prepared in the way that the individual chapters can be easily followed separately and independently. This approach unavoidably causes some redundancies between the different chapters and the author sincerely apologizes for this.

1.8 References

1. G. Crabtree and J. Sarrao, *Phys. World*, 2009, **22**, 24-30.
2. V. S. Arunachalam and E. L. Fleischer, *MRS Bulletin*, 2008, **33**, 261-263.
3. J. Baxter, Z. X. Bian, G. Chen, D. Danielson, M. S. Dresselhaus, A. G. Fedorov, T. S. Fisher, C. W. Jones, E. Maginn, U. Kortshagen, A. Manthiram, A. Nozik, D. R. Rolison, T. Sands, L. Shi, D. Sholl and Y. Y. Wu, *Energy Environ. Sci.*, 2009, **2**, 559-588.
4. Y. M. Li and G. A. Somorjai, *Nano Lett.*, 2010, **10**, 2289-2295.
5. A. J. Nozik, *Nano Lett.*, 2010, **10**, 2735-2741.
6. A. I. Hochbaum and P. D. Yang, *Chem. Rev.*, 2010, **110**, 527-546.
7. D. R. Rolison, R. W. Long, J. C. Lytle, A. E. Fischer, C. P. Rhodes, T. M. McEvoy, M. E. Bourga and A. M. Lubers, *Chem. Soc. Rev.*, 2009, **38**, 226-252.
8. A. S. Arico, P. Bruce, B. Scrosati, J. M. Tarascon and W. Van Schalkwijk, *Nat. Mater.*, 2005, **4**, 366-377.
9. R. Kotz and M. Carlen, *Electrochim. Acta*, 2000, **45**, 2483-2498.
10. J. M. Tarascon and M. Armand, *Nature*, 2001, **414**, 359-367.
11. A. Patil, V. Patil, D. W. Shin, J. W. Choi, D. S. Paik and S. J. Yoon, *Mater. Res. Bull.*, 2008, **43**, 1913-1942.
12. M. Winter and R. J. Brodd, *Chem. Rev.*, 2004, **104**, 4245-4269.
13. A. Burke, *Electrochim. Acta*, 2007, **53**, 1083-1091.
14. M. Armand and J. M. Tarascon, *Nature*, 2008, **451**, 652-657.
15. M. R. Palacin, *Chem. Soc. Rev.*, 2009, **38**, 2565-2575.
16. J. R. Miller and P. Simon, *Science*, 2008, **321**, 651-652.
17. H. Li, Z. Wang, L. Chen and X. Huang, *Adv. Mater.*, 2009, **21**, 4593-4607.
18. C. D. Lokhande, D. P. Dubal and O.-S. Joo, *Curr. Appl. Phys.*, 2011, **11**, 255-270.
19. Y. Zhang, H. Feng, X. Wu, L. Wang, A. Zhang, T. Xia, H. Dong, X. Li and L. Zhang, *Int. J. Hydrogen Energ.*, 2009, **34**, 4889-4899.
20. K. T. Lee and J. Cho, *Nano Today*, 2011, **6**, 28-41.
21. C. H. Jiang, E. Hosono and H. S. Zhou, *Nano Today*, 2006, **1**, 28-33.
22. H. K. Liu, G. X. Wang, Z. P. Guo, J. Z. Wang and K. Konstantinov, *J. Nanosci. Nanotechnol.*, 2006, **6**, 1-15.

23. P. G. Bruce, B. Scrosati and J. M. Tarascon, *Angew. Chem. Int. Ed.*, 2008, **47**, 2930-2946.

24. Y. Wang and G. Z. Cao, *Adv. Mater.*, 2008, **20**, 2251-2269.

25. D. W. Liu and G. Z. Cao, *Energy Environ. Sci.*, 2010, **3**, 1218-1237.

26. P. Simon and Y. Gogotsi, *Nat. Mater.*, 2008, **7**, 845-854.

27. C. Liu, F. Li, L. P. Ma and H. M. Cheng, *Adv. Mater.*, 2010, **22**, E28-62.

28. P. J. Hall, M. Mirzaeian, S. I. Fletcher, F. B. Sillars, A. J. R. Rennie, G. O. Shitta-Bey, G. Wilson, A. Cruden and R. Carter, *Energy Environ. Sci.*, 2010, **3**, 1238-1251.

29. X. Z. X. Zhao, B. M. Sanchez, P. J. Dobson and P. S. Grant, *Nanoscale*, 2011, **3**, 839-855.

30. W. Zhang, K. Huo, Y. Jiang, L. Hu, R. Chen and P. K. Chu, *Microchim. Acta*, 2011, **175**, 137-143.

31. J. Jiang, Y. Li, J. Liu and X. Huang, *Nanoscale*, 2011, **3**, 45-58.

32. W. Wei, X. Cui, W. Chen and D. G. Ivey, *Chem. Soc. Rev.*, 2011, **40**, 1697-1721.

33. G. Wang, L. Zhang, J. Zhang, *Chem. Soc. Rev.*, 2011, **41**, 797-828

34. U. Yogeswaran and S. M. Chen, *Sensors*, 2008, **8**, 290-313.

35. E. Katz, I. Willner and J. Wang, *Electroanalysis*, 2004, **16**, 19-44.

36. C. W. Welch and R. G. Compton, *Anal. Bioanal. Chem.*, 2006, **384**, 601-619.

37. J. Wang, *Chem. Rev.*, 2008, **108**, 814-825.

38. K. E. Toghill and R. G. Compton, *Int. J. Electrochem. Sci.*, 2010, **5**, 1246-1301.

39. S. Park, H. Boo and T. D. Chung, *Anal. Chim. Acta*, 2006, **556**, 46-57.

40. M. M. Rahman, A. J. S. Ahammad, J.-H. Jin, S. J. Ahn and J.-J. Lee, *Sensors*, 2010, **10**, 4855-4886.

41. K. E. Heusler, D. Landolt and S. Trasatti, *Pure Appl. Chem.*, 1989, **61**, 19-22.

42. G. H. Koch, M. P. H. Brongers, N. G. Thompson, Y. P. Virmani and J. H. Payer, NACE International 2002.

43. J. C. Scully, *The fundamentals of corrosion*, Pergamon Press, Oxford, England, 1990.

44. C. R. Martin, *Science*, 1994, **266**, 1961-1966.

45. M. H. Huang, Y. Wu, H. Feick, N. Tran, E. Weber and P. Yang, *Adv. Mater.*, 2001, **13**, 113-116.

46. W. Zhang and S. Yang, *Acc. Chem. Res.*, 2009, **42**, 1617-1627.

47. H.-D. Yu, Z. Zhang and M.-Y. Han, *Small*, 2012, **8**, 2621-2635.

48. P. Benson, G. W. D. Briggs and W. F. K. Wynne-Jones, *Electrochim. Acta*, 1964, **9**, 275-280.

49. P. Benson, G. W. D. Briggs and W. F. K. Wynne-Jones, *Electrochim. Acta*, 1964, **9**, 281-288.

50. B. E. Conway, *J. Electrochem. Soc.*, 1991, **138**, 1539-1548.

51. B. E. Conway, V. Birss and J. Wojtowicz, *J. Power Sources*, 1997, **66**, 1-14.

52. T. C. Liu, W. G. Pell and B. E. Conway, *Electrochim. Acta*, 1999, **44**, 2829-2842.

53. V. Srinivasan and J. W. Weidner, *J. Electrochem. Soc.*, 1997, **144**, L210-L213.

54. C. Lin, J. A. Ritter and B. N. Popov, *J. Electrochem. Soc.*, 1998, **145**, 4097-4103.

55. M. Pourbaix, *Atlas of Electrochemical Equilibria in Aqueous Solutions*, National Association of Corrosion Engineers, Houston, Tex., 1974.

56. J. Chivot, L. Mendoza, C. Mansour, T. Pauporté and M. Cassir, *Corros. Sci.*, 2008, **50**, 62-69.

57. P. Delahay, M. Pourbaix and P. Van Rysselberghe, *J. Chem. Educ.*, 1950, **27**, 683.

58. W. K. Behl and J. E. Toni, *J. Electroanal. Chem. Interf. Electrochem.*, 1971, **31**, 63-75.

59. C. N. P. Dafonseca, M. A. Depaoli and A. Gorenstein, *Sol. Energy Mater. Sol. Cells*, 1994, **33**, 73-81.

60. H. G. Meier, J. R. Vilche and A. J. Arvía, *J. Electroanal. Chem. Interf. Electrochem.*, 1982, **138**, 367-379.

61. R. Boggio, A. Carugati and S. Trasatti, *J. Appl. Electrochem.*, 1987, **17**, 828-840.

62. F. Svegl, B. Orel, M. G. Hutchins and K. Kalcher, *J. Electrochem. Soc.*, 1996, **143**, 1532-1539.

63. M. Longhi and L. Formaro, *J. Electroanal. Chem.*, 1999, **464**, 149-157.

64. T. Kessler, A. Visintin, M. R. Dechialvo, W. E. Triaca and A. J. Arvia, *J. Electroanal. Chem.*, 1989, **261**, 315-329.

65. J. Ismail, M. F. Ahmed and P. V. Kamath, *J. Power Sources*, 1991, **36**, 507-516.

66. L. D. Burke, M. E. Lyons and O. J. Murphy, *J. Electroanal. Chem.*, 1982, **132**, 247-261.

67. G. Larramona and C. Gutierrez, *J. Electroanal. Chem.*, 1990, **293**, 237-252.

68. R. D. Cowling and Riddifor.Ac, *Electrochim. Acta*, 1969, **14**, 981-&.

69. I. G. Casella and M. R. Guascito, *J. Electroanal. Chem.*, 1999, **476**, 54-63.

70. M. Figlarz, J. Guenot and Tournemo.Jn, *J. Mater. Sci.*, 1974, **9**, 772-776.

71. V. Pralong, A. Delahaye-Vidal, B. Beaudoin, B. Gerand and J. M. Tarascon, *J. Mater. Chem.*, 1999, **9**, 955-960.

72. M. Figlarz, J. Guenot and F. Fievetvincent, *J. Mater. Sci.*, 1976, **11**, 2267-2270.

73. E. Hosono, S. Fujihara, I. Honma and H. S. Zhou, *J. Mater. Chem.*, 2005, **15**, 1938-1945.

74. Y. L. Hou, H. Kondoh, M. Shimojo, T. Kogure and T. Ohta, *J. Phys. Chem. B*, 2005, **109**, 19094-19098.

75. L.-X. Yang, Y.-J. Zhu, L. Li, L. Zhang, H. Tong, W.-W. Wang, G.-F. Cheng and J.-F. Zhu, *Eur. J. Inorg. Chem.*, 2006, **2006**, 4787-4792.

76. X. Liu, R. Yi, N. Zhang, R. Shi, X. Li and G. Qiu, *Chem-Asian J.*, 2008, **3**, 732-738.

77. Y. Ding, L. Xu, C. Chen, X. Shen and S. L. Suib, *J. Phys. Chem. C*, 2008, **112**, 8177-8183.

78. L. Hu, Q. Peng and Y. Li, *J. Am. Chem. Soc.*, 2008, **130**, 16136-16137.

79. Y. Shao, J. Sun and L. Gao, *J. Phys. Chem. C*, 2009, **113**, 6566-6572.

80. Q. D. Wu, S. Liu, S. M. Yao and X. P. Gao, *Electrochem. Solid-State Lett.*, 2008, **11**, A215-A218.

81. C. C. Li, X. M. Yin, Q. H. Li, L. B. Chen and T. H. Wang, *Chem.– Eur. J.*, 2011, **17**, 1596-1604.

82. Y. Fan, H. Shao, J. Wang, L. Liu, J. Zhang and C. Cao, *Chem. Commun.*, 2011, **47**, 3469-3471.

83. J. Yang, H. W. Liu, W. N. Martens and R. L. Frost, *J. Phys. Chem. C*, 2010, **114**, 111-119.

84. X. W. Lou, D. Deng, J. Y. Lee, J. Feng and L. A. Archer, *Adv. Mater.*, 2008, **20**, 258-262.

85. F. Zhan, B. Geng and Y. Guo, *Chem.– Eur. J.*, 2009, **15**, 6169-6174.

86. Y. Zhu, H. Li, Y. Koltypin and A. Gedanken, *J. Mater. Chem.*, 2002, **12**, 729-733.

87. C.-H. Chen, S. F. Abbas, A. Morey, S. Sithambaram, L.-P. Xu, H. F. Garces, W. A. Hines and S. L. Suib, *Adv. Mater.*, 2008, **20**, 1205-1209.

88. B. Geng, F. Zhan, C. Fang and N. Yu, *J. Mater. Chem.*, 2008, **18**, 4977-4984.

89. S. R. Alvarado, Y. Guo, T. P. A. Ruberu, A. Bakac and J. Vela, *J. Phys. Chem. C*, 2012, **116**, 10382-10389.

90. J. T. Sampanthar and H. C. Zeng, *J. Am. Chem. Soc.*, 2002, **124**, 6668-6675.

91. Y. Li, B. Tan and Y. Wu, *J. Am. Chem. Soc.*, 2006, **128**, 14258-14259.

92. S. Y. Wang, K. C. Ho, S. L. Kuo and N. L. Wu, *J. Electrochem. Soc.*, 2006, **153**, A75-A80.

93. N. Nagarajan and I. Zhitomirsky, *J. Appl. Electrochem.*, 2006, **36**, 1399-1405.

94. M. B. Sassin, A. N. Mansour, K. A. Pettigrew, D. R. Rolison and J. W. Long, *ACS Nano*, 2010, **4**, 4505-4514.

95. M.-S. Wu, R.-H. Lee, J.-J. Jow, W.-D. Yang, C.-Y. Hsieh and B.-J. Weng, *Electrochem. Solid-State Lett.*, 2009, **12**, A1-A4.

96. M.-S. Wu and R.-H. Lee, *J. Electrochem. Soc.*, 2009, **156**, A737-A743.

97. D. Wang, Q. Wang and T. Wang, *Nanotechnology*, 2011, **22**.

98. X. Zhao, C. Johnston, A. Crossley and P. S. Grant, *J. Mater. Chem.*, 2010, **20**, 7637-7644.

99. W. Shi, J. Zhu, D. H. Sim, Y. Y. Tay, Z. Lu, X. Zhang, Y. Sharma, M. Srinivasan, H. Zhang, H. H. Hng and Q. Yan, *J. Mater. Chem.*, 2011, **21**, 3422-3427.

100. N.-L. Wu, S.-Y. Wang, C.-Y. Han, D.-S. Wu and L.-R. Shiue, *J. Power Sources*, 2003, **113**, 173-178.

101. S. Y. Wang and N. L. Wu, *J. Appl. Electrochem.*, 2003, **33**, 345-348.

102. T. Brousse and D. Belanger, *Electrochem. Solid-State Lett.*, 2003, **6**, A244-A248.

103. T. Cottineau, M. Toupin, T. Delahaye, T. Brousse and D. Belanger, *Appl. Phys. A-Mater.*, 2006, **82**, 599-606.

104. K. W. Chung, K. B. Kim, S. H. Han and H. Lee, *Electrochem. Solid-State Lett.*, 2005, **8**, A259-A262.

105. S. C. Pang, W. H. Khoh and S. F. Chin, *J. Mater. Sci.*, 2010, **45**, 5598-5604.

106. J. Chen, K. Huang and S. Liu, *Electrochim. Acta*, 2009, **55**, 1-5.

107. W.-H. Jin, G.-T. Cao and J.-Y. Sun, *J. Power Sources*, 2008, **175**, 686-691.

108. J. Santos-Peña, O. Crosnier and T. Brousse, *Electrochim. Acta*, 2010, **55**, 7511-7515.

109. S. Radhakrishnan, S. Prakash, C. R. K. Rao and M. Vijayan, *Electrochem. Solid-State Lett.*, 2009, **12**, A84-A87.

110. Y. W. Zhu, T. Yu, F. C. Cheong, X. J. Xu, C. T. Lim, V. B. C. Tan, J. T. L. Thong and C. H. Sow, *Nanotechnology*, 2005, **16**, 88-92.

111. B. Varghese, C. H. Teo, Y. Zhu, M. V. Reddy, B. V. R. Chowdari, A. T. S. Wee, V. B. C. Tan, C. T. Lim and C. H. Sow, *Adv. Funct. Mater.*, 2007, **17**, 1932-1939.
112. T. Yu, Y. W. Zhu, X. J. Xu, Z. X. Shen, P. Chen, C. T. Lim, J. T. L. Thong and C. H. Sow, *Adv. Mater.*, 2005, **17**, 1595-1599.
113. Y. Zhu, C.-H. Sow, T. Yu, Q. Zhao, P. Li, Z. Shen, D. Yu and J. T.-L. Thong, *Adv. Funct. Mater.*, 2006, **16**, 2415-2422.
114. T. Yu, Y. W. Zhu, X. J. Xu, K. S. Yeong, Z. X. Shen, P. Chen, C. T. Lim, J. T. L. Thong and C. H. Sow, *Small*, 2006, **2**, 80-84.
115. M. V. Reddy, T. Yu, C.-H. Sow, Z. X. Shen, C. T. Lim, G. V. S. Rao and B. V. R. Chowdari, *Adv. Funct. Mater.*, 2007, **17**, 2792-2799.
116. B. Varghese, M. V. Reddy, Z. Yanwu, C. S. Lit, T. C. Hoong, G. V. Subba Rao, B. V. R. Chowdari, A. T. S. Wee, C. T. Lim and C.-H. Sow, *Chem. Mater.*, 2008, **20**, 3360-3367.
117. K. C. Chin, G. L. Chong, C. K. Poh, L. H. Van, C. H. Sow, J. Lin and A. T. S. Wee, *J. Phys. Chem. C*, 2007, **111**, 9136-9141.

Chapter 2 – Co_3O_4 nanowalls synthesized via thermal oxidation for electrochemical capacitor

2.1 Introduction

Ruthenium oxide, RuO_2, is studied extensively as redox supercapacitors due to its high specific capacitance.[1] However, the high cost of ruthenium is a major drawback for it to be available commercially. Consequently, alternative less costly transition metal oxides were researched as electrode materials in supercapacitors. Among them are MnO_2,[2] NiO,[3] Fe_2O_3,[4] Co_3O_4[5] which have been recognized as potential electrode materials for supercapacitor. Liu *et al.* reported that Co_3O_4 is a good electrode candidate for electrochemical capacitors because of its pseudocapacitance properties arising from its highly reversible redox reaction.[5] Following that, many research groups have investigated the electrochemical properties and the reversible faradic redox reaction occurring on Co_3O_4.[6-8]

Numerous synthesis methods have been used to prepare pseudocapacitive cobalt oxides. These methods include electrochemical deposition,[6] chemical spray pyrolysis,[9] sol-gel method,[10] thermal decomposition,[11] chemical precipitation[12] *etc*. Recently, *in situ* growth approaches of Co_3O_4[13-14] and CoOOH nanostructures by thermal oxidation and wet oxidation appear as interesting alternative synthesis routes. Notably, these nanostructures were grown directly from and on the conducting metal substrates, which allow them to be used as self-supported and binder-less electrode in electrochemical capacitor and lithium ion battery[15-16].

Conventionally, an electrode of electrochemical capacitors is prepared from mixing homogeneous slurry of active materials with ancillary conducting carbon and polymer binder (mostly insulating), then the slurry is pasted onto the current collectors. These conventional electrodes possess obvious disadvantages such as poor electron transport, unfavourable electrochemical accessibility and diffusion of electrolyte to active materials, and extra weight loading of additives (20-30 %) which reduce the specific capacity.[17] In this study, the potential applications of cobalt oxide nanostructures grown via thermal oxidation of cobalt foil were evaluated as additive-free and binder-less electrode materials for electrochemical capacitors. These electrode materials eliminate post-fabrication step in conventional composite electrode preparation and present a robust adhesion of pseudocapacitive material to substrate, leading to a high cycling stability. Besides, the additive-free feature allows the high surface area of nanostructures to be fully utilized and the total weight of electrode can be reduced.

2.2 Experimental Section

2.2.1 Synthesis of cobalt oxide nanostructures

Cobalt oxide nanostructures were synthesized by oxidizing cobalt substrate on a hotplate under ambient condition based on a reported method.[13] Cobalt metal foils (Sigma Aldrich, 99.95 % purity) with a thickness of 0.1 mm and a dimension of 1 cm × 1 cm was first polished both side with sand papers (grit size 500 and 100) to remove the native oxide layer on the surface of the foil. Next, dust created during polishing was removed under a flow of purified nitrogen gas over the metal surface. The cleaned metal foil was heated at ~350 ºC or ~450 ºC for various durations (8 h, 16 h, 24 h and 48 h) directly on a Cimarec hotplate. After heating, the foil was cooled to room temperature. The mass of cobalt foil before and after heating was weighed with a Shimadzu electronic micro-balance (AEM-5200).

2.2.2 Characterizations

Scanning electron microscopy (SEM) was performed by using JEOL JSM-6400 Field Emission Scanning Electron Microscope. The morphologies of the cobalt oxide nanostructure were studied by operating the SEM at 10 kV under vacuum (9:63 × 10^{-5} Pa). Raman spectra of the cobalt oxide nanostructures were recorded by computer controlled Renishaw system 2000 at excitation wavelength of 532 nm at room temperature. X-ray photoelectron spectroscopy (XPS) measurements were performed on an ESCA MK II X-ray Photoelectron Spectrometer with a Mg Kα excitation source. The crystallographic structures and chemical composition of the cobalt oxide nanostructures were identified by X-ray diffraction (XRD). The XRD pattern were taken with a Philips Diffractometer using monochromatic Cu Kα (λ = 1.540598 Å) radiation and scanning over 2θ from 10º to 90º. The morphologies and crystalline structures of the as-grown surface layer were also examined with high resolution transmission electron microscopy (HRTEM) on a JEOL JEM-2010F instrument at 200 kV, combined with an energy dispersive X-ray analyzer.

2.2.3 Electrochemical studies

Electrochemical measurements were performed in a conventional three electrode electrochemical cell with platinum rod as the counter electrode and Ag/AgCl as the reference electrode. All potentials were referred to the reference electrode. The cobalt foil with cobalt oxide nanostructures on it served as the working electrode with an effective surface area of 1 cm^2 as one side of the cobalt foil was covered by carbon tape. All electrochemical measurements were carried out at room temperature in aqueous 3 M KOH solution. The measurement of cyclic voltammetry (CV), galvanostatic charge and discharge experiments were performed with Autolab PGSTAT30 controlled by GPES software.

2.3 Results and Discussion

2.3.1 Synthesis and characterizations of cobalt oxide nanostructures

After pre-cleaning, the cobalt foils appeared to be more reflective and shinny, indicating that the native oxide layer has been removed. Heating temperature under 350 ºC do not oxidize the cobalt foil sufficiently while the maximum temperature can be achieved by a hotplate is 450 ºC. For cobalt foils heated at 350 ºC, the shinny surfaces become dull and dark in colour after heating. For cobalt foils heated at 450 ºC, the shinny surfaces become dull but not darkened. In both cases, no crack was found on the surface during visual inspection after the cooling process. Figure 2.1a-d show cobalt foils heated at 350 ºC with surface uniformly covered with large quantities of vertically orientated nanowalls. Significantly different morphologies were observed in Co foils heated at 450 ºC, as shown in Figure 2.1e-f. In the latter case, the nanostructures appear as "collapsed" structures laying on the substrate. These results reveal that the morphologies of the cobalt oxide nanostructures are temperature dependent and less sensitive to the heating duration. Co foils that were heated at 350 ºC for durations ranging from 8 h to 48 h were consistently populated with cobalt oxide nanowalls. When the temperature was increased at 450 ºC, the morphologies remarkably changed even for short heating duration of 8 hours.

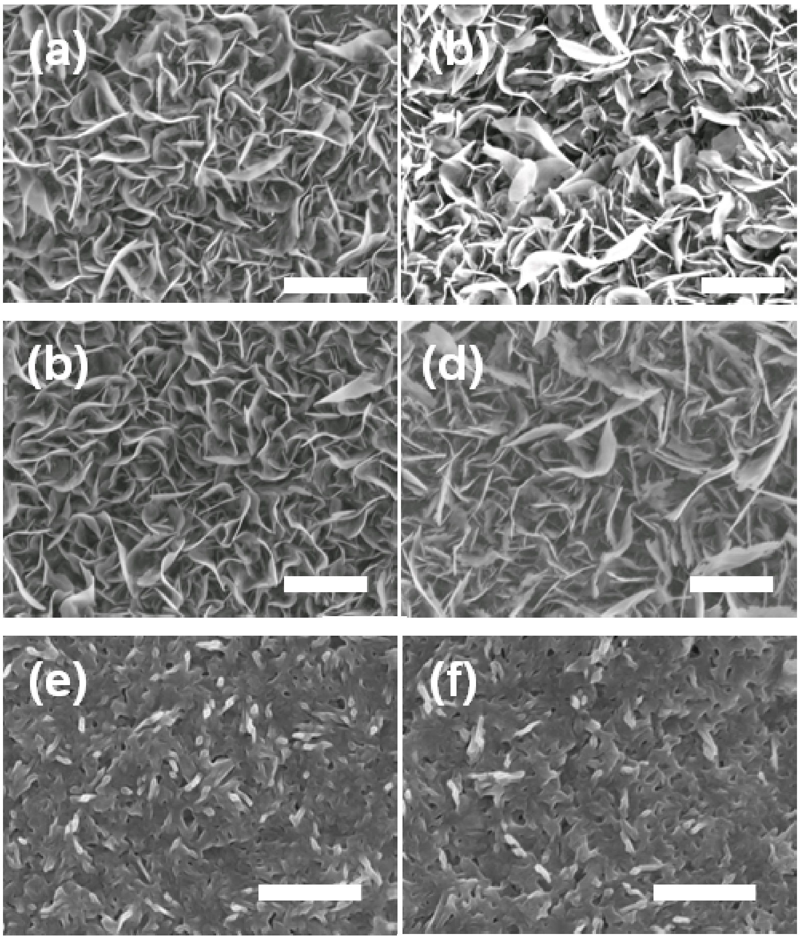

Figure 2.1. SEM images of cobalt foils heated at 350 °C for (a) 8 h, (b) 16 h, (c) 24 h, (d) 48 h and 450 °C for (e) 8 h, (f) 24 h (all scale bars = 1 μm).

The crystal structure of the as-prepared cobalt oxide nanostructures were examined by XRD. All diffraction lines can be indexed to cubic Co_3O_4 and cubic CoO (Co_3O_4: JCPDS 04-006-3982; CoO: JCPDS 01-071-4749). As displayed in inset of Figure 2.2a, the XRD patterns of cobalt foils that were heated at 350 ºC exhibit an extraordinarily high intensity at the (400) crystallographic plane of Co_3O_4. Detailed inspections on the other reflection peaks of sample heated for 24 h have to be performed by magnifying the XRD spectra as shown in Figure 2.2a. The detailed patterns remain the same for samples heated at other durations. As shown in Figure 2.2b, different XRD patterns were obtained when Co foils were heated to 450 ºC. The most distinct difference is the attenuation of the (400) peak corresponding to

Co_3O_4. This notable difference, together with their corresponding SEM images as shown in Figure 2.1, suggests that the vertically orientated nanowalls are related to this (400) peak of Co_3O_4 species. Two phases of cobalt oxide, Co_3O_4 and CoO, are present in our samples while no peak attributed to Co is detected. The presence of sub-oxide (CoO) is a common observation for the growth of Co_3O_4 nanostructures as the sub-oxide has been proposed to be the intermediate for the subsequent growth to the final Co_3O_4 nanowalls.[18]

Cobalt oxide nanostructures formed from different heating durations and temperatures gave similar Raman spectra with four typical peaks as shown in Figure 2.3. The four prominent peaks at 693 cm^{-1}, 622 cm^{-1}, 523 cm^{-1}, and 483 cm^{-1} correspond to the A_{1g}, F_{2g}, F_{2g}, and E_g modes of the crystalline Co_3O_4 phase respectively.[20] Repeated measurements of different samples gave almost identical spectra. These Raman spectra are in a good agreement with the result from XRD, which confirms that Co_3O_4 is the main cobalt oxide species formed. CoO does not have active vibrational Raman mode and thus is not shown in the Raman spectra.

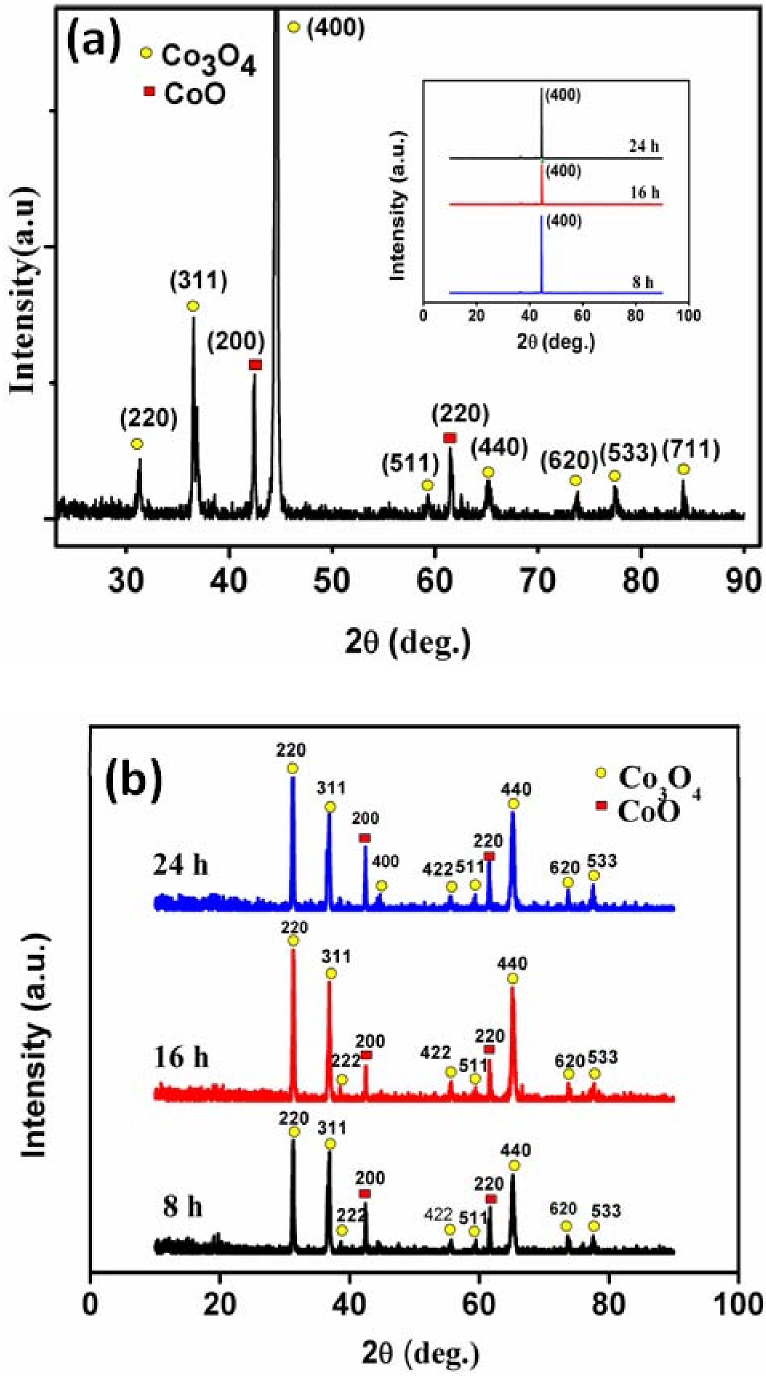

Figure 2.2. (a) XRD patterns of cobalt foil heated at 350 °C for various durations (inset) and the magnified XRD pattern of cobalt foil heated at 350 °C for 24 h, (b) XRD patterns of cobalt foil heated at 450 °C for various durations.

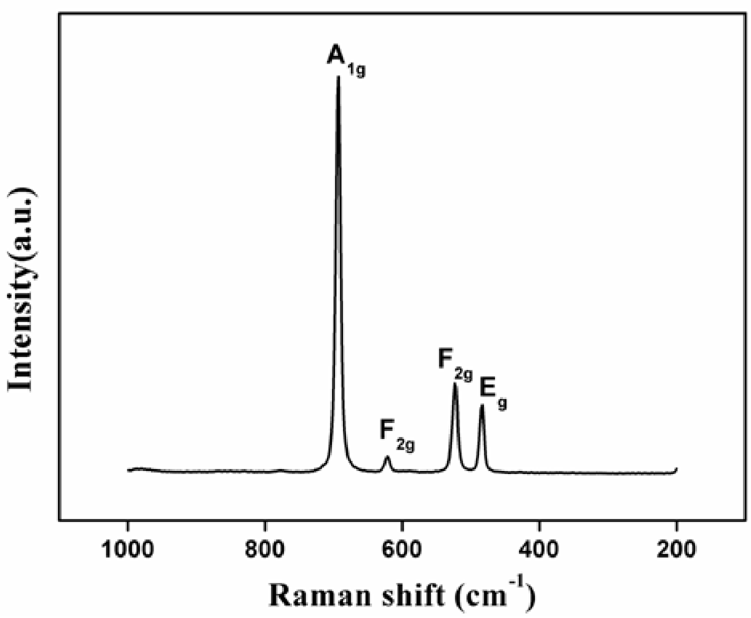

Figure 2.3. Representative Raman spectrum of the heated cobalt foil.

Figure 2.4a-b show TEM images of the isolated Co_3O_4 nanowalls. In Figure 2.4c, the corresponding SAED pattern reveals that the as-synthesized Co_3O_4 nanowalls are highly crystalline. The diffraction pattern can be readily indexed with the lattice parameters of the Co_3O_4 phase. The measured lattice spacing in HRTEM (Figure 2.4d) is 0.289 nm, corresponding to the interlayer spacing of the (220) planes of Co_3O_4 (d = 0.285 nm). Energy dispersive X-ray (EDX) analysis (Figure 2.5) indicates that the composition of nanowalls consist of cobalt and oxide. The copper, carbon and silicon peaks are originated from the TEM grid.

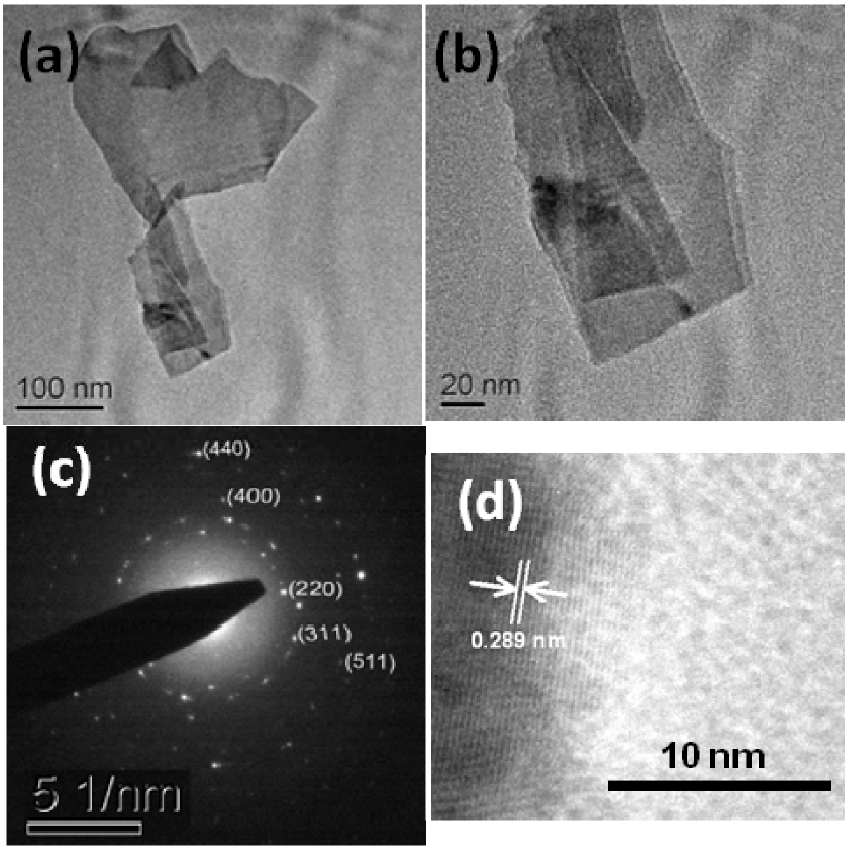

Figure 2.4. (a, b) TEM images of isolated cobalt oxide nanowalls, (c) SAED of cobalt oxide nanowalls, (d) HRTEM image of cobalt oxide nanowalls.

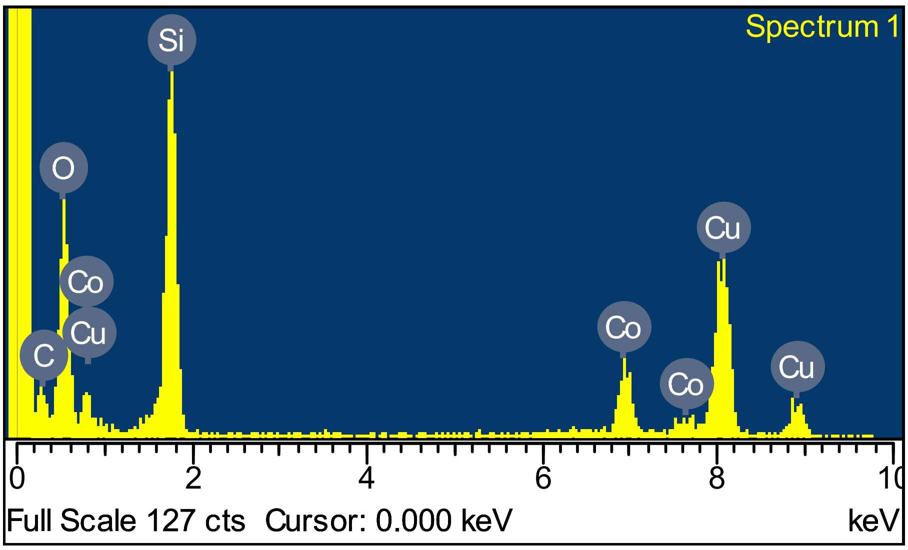

Figure 2.5. EDX spectrum of the Co_3O_4 nanowalls.

The wide scan XPS spectrum of Co_3O_4 nanowalls is displayed in Figure 2.6a. All of the peaks shown in the spectrum correspond to the binding energy (BE) ranges of Co 2p, 3s, 3p and O 1s, as well as C 1s coming from the atmosphere. Consistent with the result from EDX (Figure 2.5), the samples do not contain other inorganic contaminants. The peak at Co 2p region (Figure 2.6b) shows spin-orbit splitting into $2p_{1/2}$ (795.2 eV) and $2p_{3/2}$ (780.2 eV) components. The XPS spectrum exhibits tail at higher BE, indicating the mixed Co^{3+} and Co^{2+} oxidation state in the cobalt oxide. The O 1s XPS peaks of the Co_3O_4 nanowalls (Figure 2.6c) can be fitted to three components which are consistent with our recently reported XPS peaks of Co_3O_4 nanosheets prepared via thermal conversion from CoOOH. The intense O 1s XPS peak at 529.7 eV corresponds to oxygen species in the spinel cobalt oxide phase. The weak tailing off at higher BE peak suggests that OH (hydroxyl) species are present and it may come from moisture adsorbs on the surface. Combining these results with XRD analysis, it is clear that the nanowalls composed of Co_3O_4.

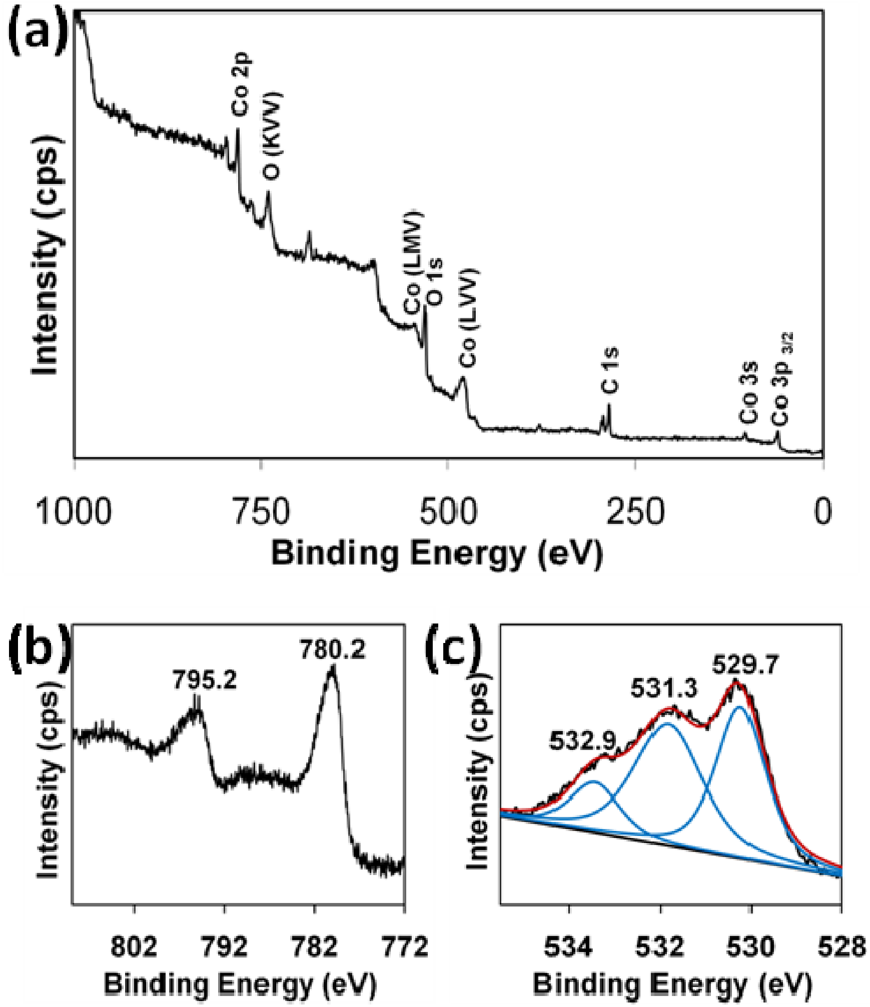

Figure 2.6. (a) Wide scan XPS spectrum, (b) XPS spectrum of the Co 2p region, (c) XPS spectrum of the O 1s of Co_3O_4 nanowalls.

According to XRD result, it is clear that Co_3O_4 and CoO co-exist in the sample after heating. Li *et al.*[20] and Wang *et al.*[21] have calculated the weight of NiO formed on Ni based on the weight difference of Ni foam before and after oxidation. By employing similar method, we can estimate the mass of Co_3O_4 based on the mass difference of Co foil before and after heating. However, we need to consider the additional existence of CoO. Thus, we determined the ratio of Co_3O_4 to CoO from the relative intensity of their diffraction peaks in the XRD spectra. The peak area of the most intense XRD peak for Co_3O_4 was compared with that for CoO, this provides a good estimation of the ratio of Co_3O_4 to CoO. Details of the mass calculation can be found *vide infra* in Section 2.3.2 "Detailed calculation procedures of Co_3O_4 mass on cobalt foil" while the mass of Co_3O_4 for different samples prepared under different conditions are summarised in Table 2.1.

Table 2.1. Mass of Co_3O_4 on Co foils heated to different temperature and durations.

	Mass of Co_3O_4 (mg)	
Duration (h)	**Co-350[a]**	**Co-450[b]**
8	0.737	3.783
16	1.303	5.960
24	1.383	4.936
48	1.589	--

[a]Co-350: Cobalt foils heated at 350 °C
[b]Co-450: Cobalt foils heated at 450 °C

Table 2.1 indicates that the mass of Co_3O_4 ranged from 0.7 mg to 6 mg. The typical mass of the Co foil before heating is around 103 mg. These results show that only the top layer of the cobalt foil is converted into the oxide form. This is consistent with the proposed growth mechanism of cobalt oxide nanostructures.[13] According to the mechanism, only the surface layer of the metal melts, forming a liquid media. Oxygen in the air will dissolve in the liquid Co and oxidize Co to CoO (sub-oxide). This sub-oxide acts as a precursor for the subsequent growth of Co_3O_4 nanostructures. At a fixed temperature, the mass of Co_3O_4 increases with the heating duration. The results imply that, given a longer heating time, more cobalt can be oxidized which eventually lead to more Co_3O_4 nanostructures. However, when the Co foil was heated at 450 ºC for 24 h, the mass appeared to be lower than foils that were heated at 450 °C for 16 h. Further investigations need to be carried out to verify this supposition. When the temperature was increased from 350 °C to 450 °C, the mass of Co_3O_4 increases significantly (around 3 times higher). Nonetheless, as will be discussed in the following section, the higher mass of Co_3O_4 in cobalt foils heated to 450 °C does not give the best morphology for the Co_3O_4 nanostructures to serve as better electrode materials for supercapacitors.

2.3.2 Detailed calculation procedures of Co_3O_4 mass on cobalt foil

The ratio of Co_3O_4 to CoO was determined from the relative intensity of the diffraction peaks in XRD spectra. The most intense peak of Co_3O_4 was compared with the most intense peak of CoO and this provides an estimation for the ratio of Co_3O_4 to CoO. Relative intensity was used instead of absolute intensity because absolute intensity can be affected by instrumental and experimental parameters. In the measurement of peak intensity, peak areas are better than peak height. Early research by Yu *et al.*[13] reveals that the CoO component is underneath the Co_3O_4 nanowalls but the estimation of ratio through the XRD peak intensity is still fairly reasonable. One potential source of error is due to the fact that X-ray diffracted from CoO will need to pass through the nanowalls and become attenuated before it reaches the detector. However, this problem can be neglected since a very energetic monochromatic Cu Kα (λ = 1.540598nm) radiation is employed in the XRD measurement.

The step by step calculation of mass is demonstrated as follows. The mass difference (Δm) of Co foil before and after heating is related to the mass of oxygen present in the sample due to oxidation. From here, the number of oxygen atoms can be determined from Equation 2.1,where N_A is the Avogadro constant:

$$\text{Total oxygen atoms} = \frac{\Delta m}{\text{molar mass of oxygen}} \times N_A \qquad (2.1)$$

The ratio of Co_3O_4 to CoO was determined from XRD and suppose the ratio is:

$$Co_3O_4 : CoO = x : y$$

This is related to the ratio of the oxygen atom attached to each molecule by:

Oxygen atoms attached to Co_3O_4 : oxygen atoms attached to CoO = 4x : y

From here, the number of oxygen atoms attached to Co_3O_4 can be deduced by direct proportionality as in Equation 2.2.

$$\text{Number of oxygen atoms attached to } Co_3O_4 = \text{ total oxygen atom } \times \frac{4x}{4x+y} \quad (2.2)$$

Once the number of oxygen atom attached to Co_3O_4 is known, the number of Co_3O_4 molecules can be estimated by simply dividing the number of oxygen atom attached to Co_3O_4 by 4. Finally, the mass of Co_3O_4 can be calculated by Equation 2.3

$$M = \frac{\text{No of } Co_3O_4 \text{ molecules} \times \text{molar mass of } Co_3O_4}{N_A} \quad (2.3)$$

2.3.3 Electrochemical studies of cobalt oxide nanostructures

CV analysis of the cobalt oxide sample was performed in KOH electrolytes at different concentrations of 1 M to 5 M. Results in Figure 2.7 shows that at concentration higher than 3 M, oxygen evolution occurs at lower potential which limits the potential window for the material. Therefore, the concentration of electrolyte was chosen to be 3 M in the subsequent studies.

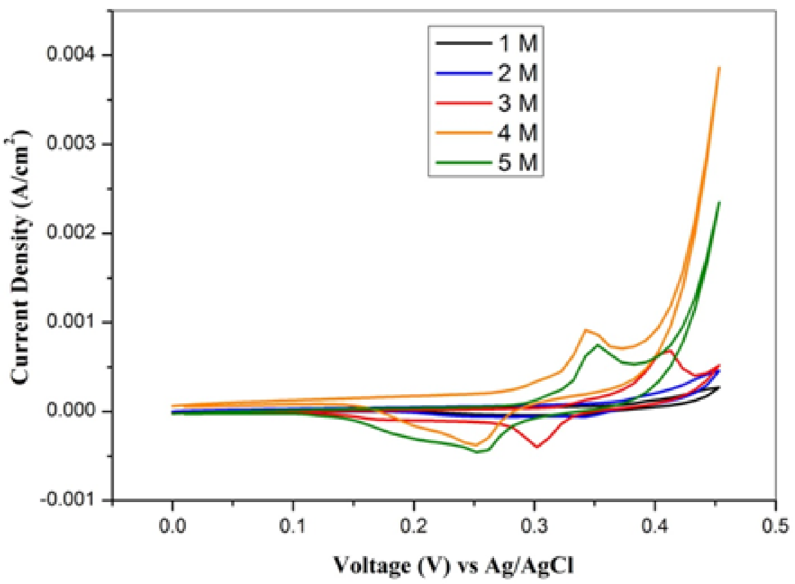

Figure 2.7. CV curves of a cobalt oxide sample performed in KOH electrolyte at different concentrations of 1 M to 5 M.

The mass of Co_3O_4 obtained from Co-450 samples (cobalt foils heated at 450 °C) is significantly higher than that formed on Co-350 samples (Table 2.1). Nevertheless, Co-450 samples do not show advantages in terms of capacitance in spite of their remarkably higher mass of Co_3O_4. Figure 2.8a compares the CV curves of Co-350 (cobalt foils heated at 350 °C) sample and Co-450 sample (of same sample size) heated to 24 h. Apparently the Co-350 sample and Co-450 sample have similar CV integral area. However, since the mass of Co_3O_4 in Co-450 is about 3-4 times higher than Co-350, this implies that Co-350 sample showed better specific capacitance than Co-450. This result is consistent with TEM analysis (Figure 2.1), which showed that the Co-350 samples consisted of nanowalls morphologies with higher surface area and a looser structure. Higher exposed surface area will increase the active site for the pseudocapacitance and facilitate the movement of OH^- ions within the electrode.[6] In line with this, further studies of electrochemical capacitor behaviour presented below will focus on the Co-350 samples.

Figure 2.8b presents the CV curves obtained at scan rate of 10 mV s^{-1} for Co-350 samples heated for various durations. The result illustrates that all samples have similar CV curves and their areas under the curve increase accordingly with the heating duration. The capacitive characteristic of Co_3O_4 nanowalls is different from that of electric double layer capacitance. A pair of pronounced redox peaks is observed for Co_3O_4 electrode. The capacitive behavior could be attributed to the following reaction:[10]

$$Co_3O_4 + OH^- + H_2O \rightarrow 3\ CoOOH + e^-$$

Furthermore, the specific capacitances C_m can be calculated from the CV curved based on Equation 2.4:

$$C_m = \frac{1}{mR\Delta V} \int I(V)dV \quad (2.4)$$

where m is the mass of the active material, R is the scan rate, ΔV is the potential window of scanning, and I(V) the integral area under the CV curve. The calculated specific capacitances from CVs obtained at 10 mV s^{-1} for the Co-350 samples prepared at 16 h, 24 h and 48 h are 32 F g^{-1}, 38 F g^{-1} and 39 F g^{-1}, respectively. As seen from Figure 2.8c, the overall shape of the CV curves are maintained at a wide ranging scan rates from 5 mV s^{-1} to 200 mV s^{-1}. This indicates a good high-rate performance of the electrode materials, most probably due to the nanometre to micrometre scale of the nanowalls structures, as well as the direct connection of the nanomaterials to the conducting substrate. Correlation between the anodic peak current and cathodic peak current against (scan rate)$^{1/2}$ gives a linear relationship (Figure 2.8d), suggesting a diffusion-controlled process.

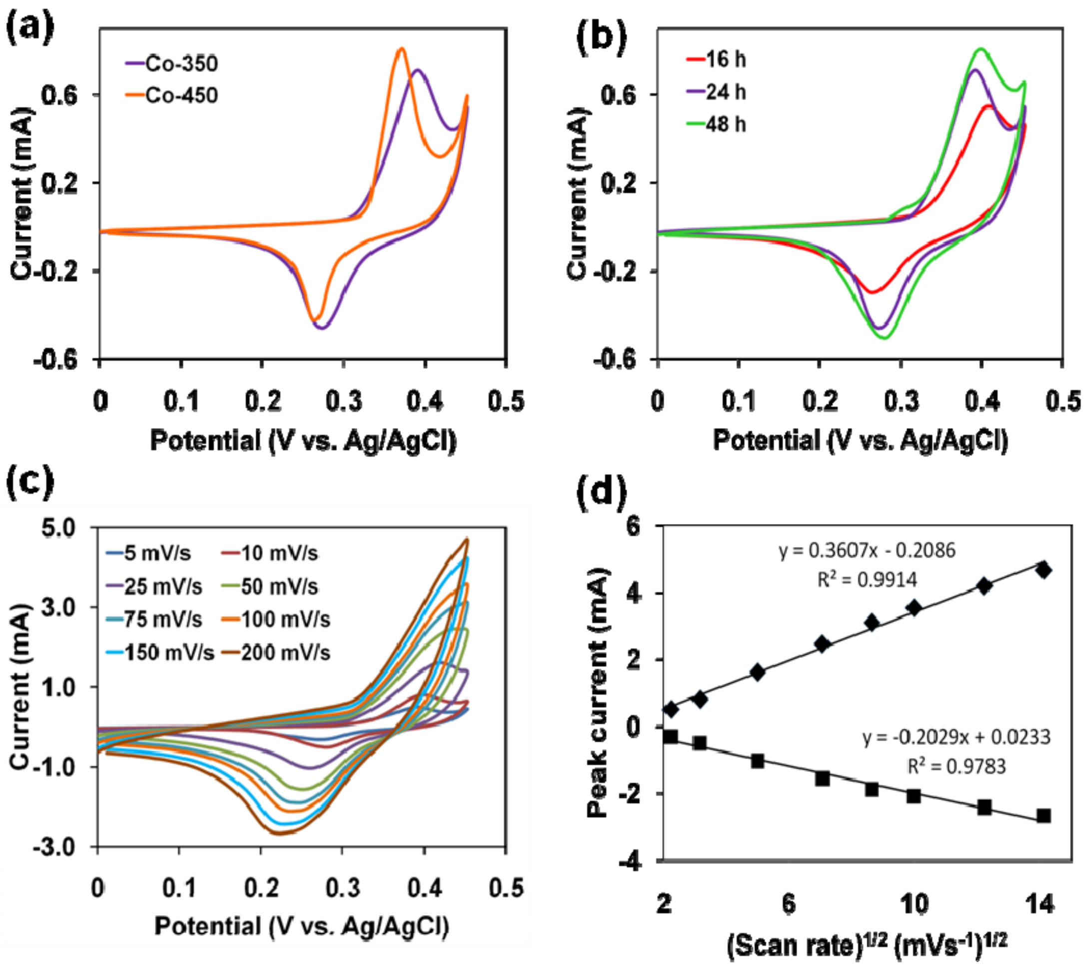

Figure 2.8. (a) CV curves of Co_3O_4 prepared at 350 °C (Co-350) and 450 °C (Co-450) for 24 h, (b) CV curves of Co-350 sample for different heating durations, (c) CV curves of Co-350 sample at different scan rates, (d) plots of peak currents from (c).

Figure 2.9a displays the galvanostatic charge-discharge curves of cobalt oxide nanowalls at different current densities. The discharge curves are made up of two sections: a sudden potential drop representing the voltage change due to internal resistance, and a slow potential decay which is the voltage change arising from the change of energy within the capacitor. The specific capacitances C_m were also calculated from the galvanostatic discharge curves using Equation 2.5 as follows:

$$C_m = \frac{I \times \Delta t}{m \times \Delta V} \quad (2.5)$$

where ΔV is the potential window during discharging, Δt is the discharging time, m is the mass of active material and I is the discharging current. As shown in Figure 2.9b, The Co_3O_4 nanowalls presented a specific capacitance of 35 F g^{-1} at a discharge current density of 0.25 mA cm^{-2} (~0.3 A g^{-1}) and remained at 22 F g^{-1} at a discharge current density of 1.50 mA cm^{-2} (~2 A g^{-1}). At the lower current density, the diffusion of ion from the electrolyte can gain access to the maximum surface area of the active materials, therefore produce a higher C_m. With the increment of current density, the effective interaction between the ions and electrode is reduced resulting in a reduction in capacitance. Besides, this may also be due to the ohmic resistance resulting from poorer electrolyte diffusion within the Co_3O_4 nanowalls at high charging-discharging rate. It is important to mention that in the above electrochemical experiments, the electrical contacts were formed by simply attaching Co_3O_4 (on cobalt substrate) to crocodile clips. This resulted in high value of resistance due to the low conductivity of Co_3O_4. Thus, there is significant scope for further optimizing the contact resistance and improving the specific capacitance.

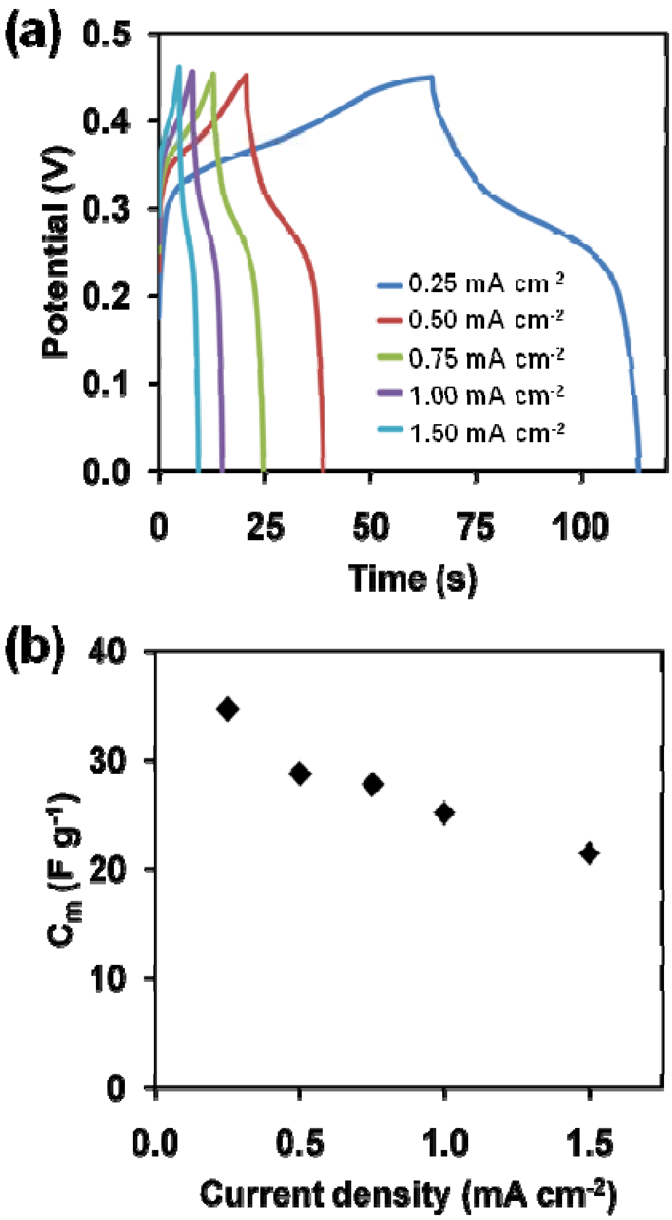

Figure 2.9. (a) Galvanostatic charge-discharge curves at different current densities for Co_3O_4 nanowalls, (b) the corresponding derived specific capacitances from discharge curves at different scan rates.

Cycling life is another crucial aspect for electrochemical capacitor. The cycling life evaluation over continuous 1500 cycles for the Co_3O_4 nanowalls (Co-350) at a current density of 0.50 mA cm^{-2} (~0.6 A g^{-1}) was carried out using galvanostatic charge-discharge cycling techniques in the potential window ranging from 0 to 0.45 V. Figure 2.10 presents the specific capacitance retention of the

Co_3O_4 nanowalls as a function of discharge cycling numbers. The electrode showed a stable specific capacitance with no apparent reduction after 1500 charge-discharge cycles. The last 10 cycles (right inset in Figure 2.10) remained almost the same shape as charge-discharge curves from the 11th to 20th cycles (left inset in Figure 2.10), illustrating the excellent long term cycling life of the nanowalls electrode.

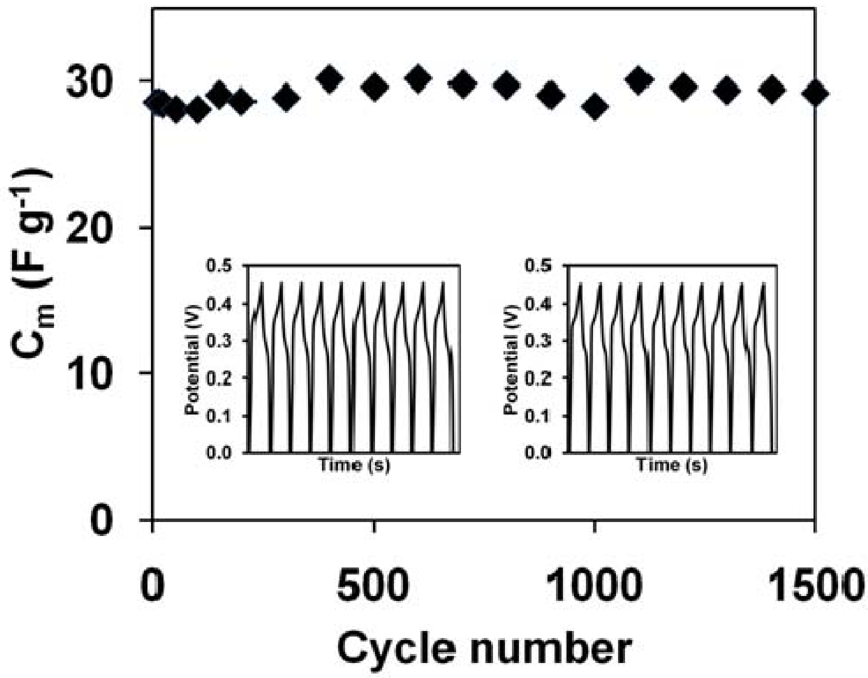

Figure 2.10. Cycling life data at a discharge current of 0.5 mA cm^{-2}, insets shown are the charge-discharge curves of the 11th-20th cycles (left inset) and charge-discharge curves of the 1490th-1500th cycles (right inset).

2.4 Conclusions

We demonstrated a simple, one-step approach to synthesize cobalt oxide nanostructures that can be used as electrochemical capacitors. By varying the growth temperature, two different morphologies of Co_3O_4 nanostructures were obtained which subsequently affect the electrochemical performance. Experimental results also showed that the growth durations will increase the mass of Co_3O_4 and eventually increase the capacitance of Co_3O_4 nanowalls. One major issue with most metal oxide electrodes in electrochemical capacitors is the relatively poor cycling stability compared to carbon materials, which partially results from the dissolution of metal oxides in electrolyte, and loss of adhesion between the active materials and the current collectors. Direct growth of metal oxide on conducting metal substrates as demonstrated in this Chapter has demonstrated the robust connection of active materials to current collectors, enabling a remarkable cycle life. However, further effort is required to enhance the conductivity of the above nanostructured metal oxide so as to increase the specific capacitance. As only the top surface of the cobalt foil is converted into the oxide nanostructures, this implies that this simple thermal oxidation route to synthesize metal oxide nanostructures can be extended to metal film-coated substrates.[15]

2.5 References

1. Simon P and Gogotsi Y 2008 *Nat. Mater.* **7** 845-854.
2. Cottineau T, Toupin M, Delahaye T, Brousse T and Bélanger D 2006 *Appl. Phys. A* **82** 599-606.
3. Zhang F, Zhou Y and Li H. 2004 *Mater. Chem. Phys.* **83** 260-264.
4. Wu M and Lee R 2009 *J. Electrochem. Soc.* **156** A737-A743.
5. Liu T C, Pell W G and Conway B E 1999 *Electrochim. Acta* **44** 2829-2842.
6. Deng M, Huang F and Sun I 2009 *Nanotechnology* **20** 175602-175607.
7. Kandalkar S, Dhawale D, Kim C and Lokhande C 2010 *Synth. Met.* **160** 1299-1302.
8. Srinivasan V and Weidner J 2002 *J. Power Sources* **108** 15-20.
9. Shinde V, Mahadik S, Gujar T and Lokhande C 2006 *Appl. Surf. Sci.* **252** 7487-7492.
10. Lin C, Ritter J A and Popov B N 1998 *J. Electrochem. Soc.* **145** 4097-4103.
11. Da Silva L, De Faria L and Boodts J 2002 *J. Electroanal. Chem.* **532** 141-150.
12. Cao L, Lu M and Li H.2005 *J. Electrochem. Soc.* **152** A871-A875.
13. Yu T, Zhu Y W, Xu X J, Shen Z X, Chen P, Lim C T, Thong J T L and Sow C H 2005 *Adv. Mater.* **17** 1595-1599.
14. Varghese B, Teo C H, Zhu Y W, Reddy M V, Chowdari B V R, Wee AT S, Tan B C V, Lim C T and Sow C H 2007 *Adv. Funct. Mater.* **17** 1932-1939.

15. Reddy M V, Yu T, Sow C H, Shen Z X, Lim C T, Rao G V S and Chowdari B V R 2007 *Adv. Funct. Mater.* **17** 2792-2799.

16. Varghese B, Reddy M V, Zhu Y W, Chang S L, Teo C H, Rao G V S, Chowdari B V R, Wee A T S, Lim C T and Sow C H 2008 *Chem. Mater.* **20** 3360-3367.

17. Jiang J, Li Y, Liu J, Huang X 2011 *Nanoscale* **3** 45-58.

18. Zhu Y and Sow C H 2009 Hotplate techniques for nanomaterials *Selected Topics in Nanoscience and Nanotechnology* ed Wee A T S (Singapore: World Scientific) pp 149-169.

19. Tang C W, Wang C B and Chien S H 2008 *Thermochim. Acta* **473** 68-73.

20. Li X, Dhanabalan A, Bechtold K and Wang C 2010 *Electrochem. Commun.* **12** 1222-1225.

21. Wang X, Li X, Sun X, Li F, Liu Q, Wang Q and He D 2011 *J. Mater. Chem.* **21** 3571-3573.

22. Xiong S, Yuan C, Zhang X, Xi B and Qian, Y. 2009 *Chem. Eur. J.* **15** 5320-5326.

Chapter 3 – Fabrication of CoOOH and Co_3O_4 nanosheets and their comparative electrochemical capacitance studies

3.1 Introduction

Among the metal oxides, pseudocapacitive behavior of ruthenium oxide (RuO_2) has been the most widely studied system in the past 30 years[1]. Despite its conductive nature, high specific capacitance and specific power, the application of RuO_2 is limited by its high cost. As the alternatives, less expensive oxides of manganese, cobalt, nickel, vanadium, iron, molybdenum and tin have been investigated[1-3]. A variety of cobalt compounds, including $Co(OH)_2$ (both α and β phase)[4-14] and Co_3O_4 [15-27], have also been explored because of their high redox activity and reversibility. Notably, there were only a few reports on the pseudocapacitance of CoOOH in the literature[28-30]. CoOOH is known as a highly conductive material (5 S cm^{-1})[28] and widely used as an additive in nickel-based alkaline secondary batteries (e.g. Ni-Cd and Ni-metal hydride batteries) to improve their electrochemical performances[31, 32]. Considering the conductivity and redox properties of CoOOH, CoOOH is a viable candidate in supercapacitors with high rate properties and good capacitance. However, the controlled synthesis of CoOOH remains a big challenge. Contrary to $Co(OH)_2$ and Co_3O_4, CoOOH consists predominantly of Co^{3+} oxidation states, which is less stable than Co^{2+} in most situations. Typically, CoOOH has been synthesized via the conventional solution method at high alkaline concentration, using high temperature and/or long reaction time. Considering the above constraints, it is thus worthwhile to develop a direct and simple synthetic route to prepare CoOOH and investigate its pseudocapacitive properties.

Nanostructured materials are becoming increasingly important for electrochemical energy storage and, sometimes, a notable improvement in performance has been achieved[3, 33, 34]. The capability of electrode materials is significantly influenced by its surface area and morphology. High surface area offers more reaction sites, better utilization of materials and rapid diffusion of the electrolyte. Previously, our group has successfully prepared various metal oxide nanostructures directly from and on metal substrates via simple thermal treatments[35-41] and a low temperature oxidation process[42, 43]. These approaches enable the synthesis and assembly of nanostructured materials in one step to provide the desired functionalities.

In this study, we introduce a simple strategy to prepare nanostructured CoOOH on metal substrate via a single step at room temperature. We also demonstrate a conversion of CoOOH to Co_3O_4 via direct thermal treatment, with the unique nanosheet structures preserved. Comprehensive electrochemical studies by cyclic voltammetry (CV) and galvanostatic charge-discharge experiments were performed to investigate the pseudocapacitive behavior of the self-supported and binderless CoOOH and Co_3O_4 nanosheet arrays electrodes. Interesting and informative results were obtained from the comparative studies, revealing different electrochemical properties and performance for the morphologically similar but compositionally different CoOOH and Co_3O_4 compounds.

3.2 Experimental Section

3.2.1 Synthesis of CoOOH nanosheets

Cobalt foils (Sigma Aldrich, 99.95 %) with thickness of 0.1 mm were used both as supporting substrate as well as the source of metal precursor for the growth of CoOOH. A stock of 2.5 M NaOH solution was first prepared by dissolving 50 g of NaOH pellets (Merck) in 500 mL distilled water. Prior to the reaction, the Co metal foil (dimension of 1 × 1 cm^2, 1.2 × 1.2 cm^2 or 1.5 × 1.5 cm^2) was sonicated (Elmasonic E30H) in 10 mL of 1 M HCl for 15 minutes to remove the native oxide layer. The foil was then rinsed several times with distilled water and dried under a pure N_2 flow. To prepare CoOOH nanosheet arrays on this substrate, 10 mL of the 2.5 M NaOH solution was loaded into a small glass bottle, and the pre-cleaned metal foil was immersed into the solution. The Co foil is magnetic by nature, it was attached to a small magnetic bar and rotated continuously at 300 rpm at room temperature. After 9 h, the synthesized sample with dark brown surface color on both sides was obtained. It was rinsed several times with distilled water and dried under N_2 flow.

3.2.2 Thermal conversion of CoOOH to Co_3O_4 nanosheets

The as-synthesized CoOOH nanosheets on cobalt foil was placed on a ceramic top digital hot plate (Barnstead Thermolyne, model Cimarec) and heated to the maximum operating temperature of 300°C in ambient atmosphere for 4 h. After cooling down naturally to room temperature, Co_3O_4 sample was obtained.

3.2.3 Characterizations

The morphologies of the nanostructures were examined with a JEOL JSM-6400F Field Emission Scanning Electron Microscope (FESEM), operating at 5 kV in high vacuum. X-ray diffraction (XRD) patterns were recorded on a Philips Diffractometer using Cu Kα radiation (λ = 1.54187 Å), scanning in the 2θ range of 10—100°. Raman spectra were measured by a Renishaw 2000 system at 532 nm wavelength under ambient conditions. Transmission electron microscopy (TEM), energy dispersive X-ray spectroscopy (EDX), and selected area electron diffraction (SAED) were carried out to examine the morphology and crystalline structures using TEM JEOL-3010F operated at 300 kV. Fourier-transform infrared (FT-IR) spectra were obtained by a Varian spectrometer in the range of 400-1000 cm^{-1}. The sample scratched from cobalt foil was diluted with 100 mg of IR-grade KBr powder and subjected to a pressure of 10 tons.

3.2.4 Electrochemical studies

CoOOH nanosheets were formed on both sides of the cobalt substrate. To prepare a conductive surface, one side of the sample was carefully removed by a 2 M HCl wetted wipers and cleaned. The conductive side was placed onto a circular gold plate, and sealed tightly in a Teflon holder with an O-ring of 1 cm diameter (geometric area of electrode = 0.785 cm^2). A three-electrode cell was assembled with the CoOOH nanosheets as the working electrode, platinum wire as the counter electrode and Ag/AgCl as the reference electrode. All potentials were referenced to the Ag/AgCl (3 M KCl) electrode. NaOH aqueous solution (0.1 M) was used as the electrolyte. Chronoamperometric measurements were carried out under constant magnetic stirring. All measurements were carried out using an Autolab PGSTAT 30 potentiostat/ galvanostat at room temperature.

3.3 Results and Discussion

3.3.1 Formation and characterizations of CoOOH nanosheets

The shiny Co surface turned to dark brown color after the treatment with NaOH, suggesting the formation of CoOOH on the cobalt surface. Other possible phases such as α-$Co(OH)_2$ and β-$Co(OH)_2$ are known to appear as green-bluish and pink to rose-red color respectively[44, 45]. The treated surface showed the formation of dense and continuous nanosheet networks on the Co substrate (Figure 3.1).

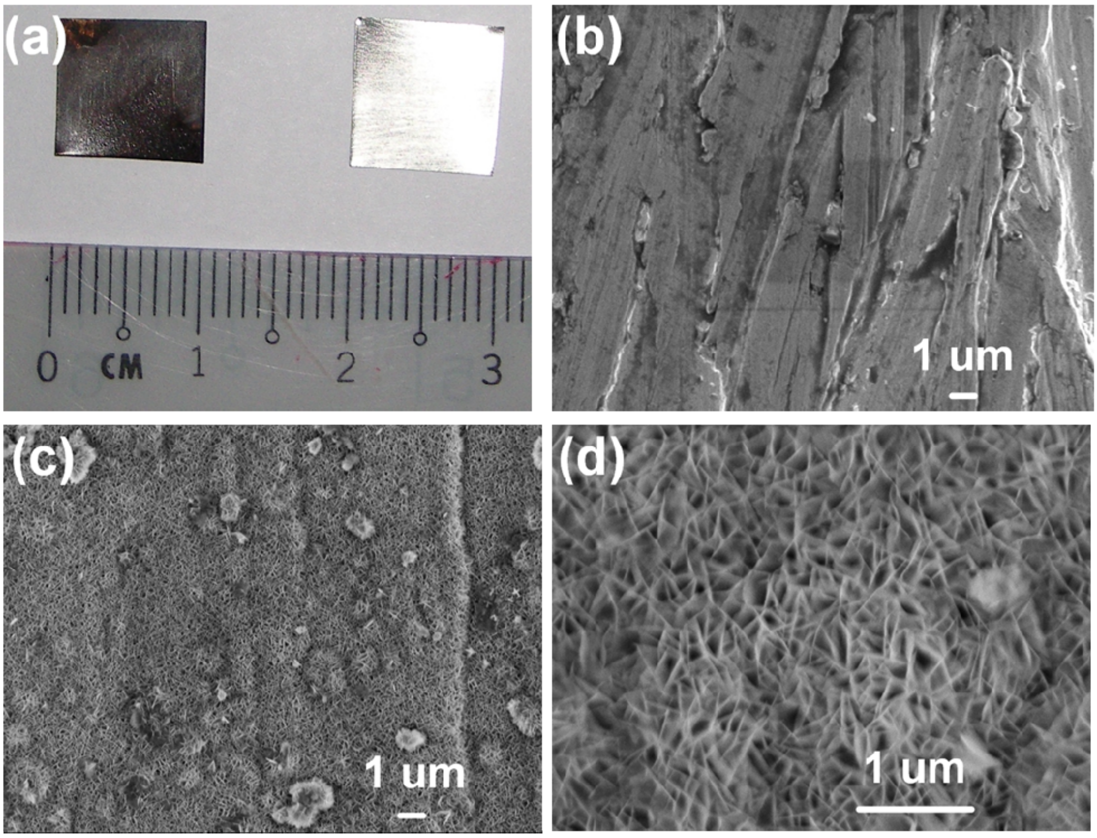

Figure 3.1. (a) Photographs showing the appearance of a cobalt foil before (right) and after (left) NaOH treatment. (b) SEM image of Co foil before NaOH treatment. (c and d) SEM images of CoOOH nanosheet arrays grown on the Co foil at (c) low and (d) high magnification.

The composition and crystal structures of the nanosheets were analyzed with XRD and Raman spectroscopy. Figure 3.2a presents a typical XRD pattern of the sample. Besides the characteristic peaks from the cobalt substrate (JCPDS card no.: 05-0727), other diffraction peaks at 19.3°, 38.2°, 39.0°, 51.7°, 62.7°, 65.5° and 70.0° can be indexed respectively to the (003), (101), (012), (015), (009), (110) and (113) planes of CoOOH (JCPDS card no.: 07-0169). These planes clearly confirm the formation of CoOOH with rhombohedral heterogenite-3R structure with cell parameters a = 2.855 Å and c = 13.156 Å. The positions and the relative intensity ratios of the diffraction peaks closely matched with published results of CoOOH[46-51].

In order to further confirm the nature of the nanosheets, Raman spectrum of the prepared sample was measured in the range of 200-1000 cm^{-1}. Typical Raman spectrum in Figure 3.2b exhibited one strong vibration at 499 cm^{-1} and two weaker vibrations at 575 and 634 cm^{-1}, which agree well with that of the CoOOH film prepared by potentiostatic electrolysis[52] and the CoOOH hollow spheres synthesized via hydrothermal method[50]. Heterogenite is a naturally occurring mineral; there are at least three different polytypes (1R, 3R and 2H) of heterogenite. Hence different Raman peaks may be observed as discussed by Yang *et al.*[50]. The Raman spectrum we obtained is distinctly different from the Raman spectrum of $Co(OH)_2$[50] and Co_3O_4[36, 39], thus ruling out the formation of these phases. Complimentary to the Raman spectrum, Figure 3.2c shows the FTIR absorption spectrum of the CoOOH sample. The FTIR spectrum displayed a single strong band at 585 cm^{-1}, which can be attributed to cobalt ion in octahedral holes, i.e. in an oxygen octahedral environment[53].

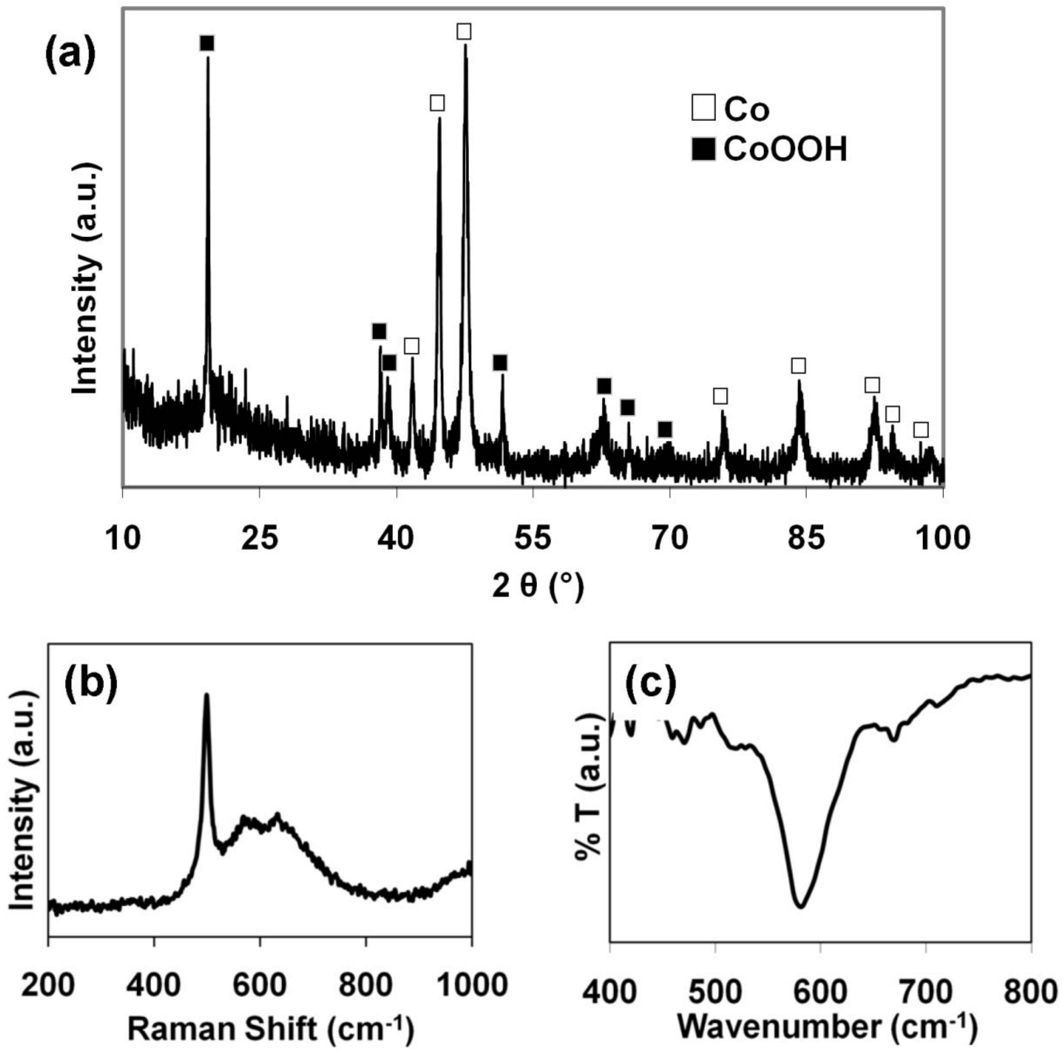

Figure 3.2. (a) XRD pattern of the as-prepared nanosheet arrays on cobalt substrate. The standard XRD patterns from database JCPDS 05-0727 of cobalt and JCPDS 07-0169 of CoOOH were denoted, (b) Raman spectrum of the as-grown CoOOH nanosheet arrays. One strong peak at 499 cm^{-1} and two weaker vibrations at 575 and 634 cm^{-1} were observed, (c) FTIR spectrum of the as-grown CoOOH nanosheet arrays.

Figure 3.3a presents a typical TEM image of the isolated CoOOH nanosheets with the corresponding SAED pattern in Figure 3.3b. The SAED pattern clearly confirmed the good crystallinity of the sample with diffraction spots indexed to the rhombohedral heterogenite (CoOOH) phase. The high resolution TEM image in Figure 3.3c reveals lattice spacing of 0.225 nm, which corresponded to [012] direction. Figure 3.3d also revealed that the nanosheets consist of cobalt and oxygen, as well as copper signal attributable to the Cu grid used.

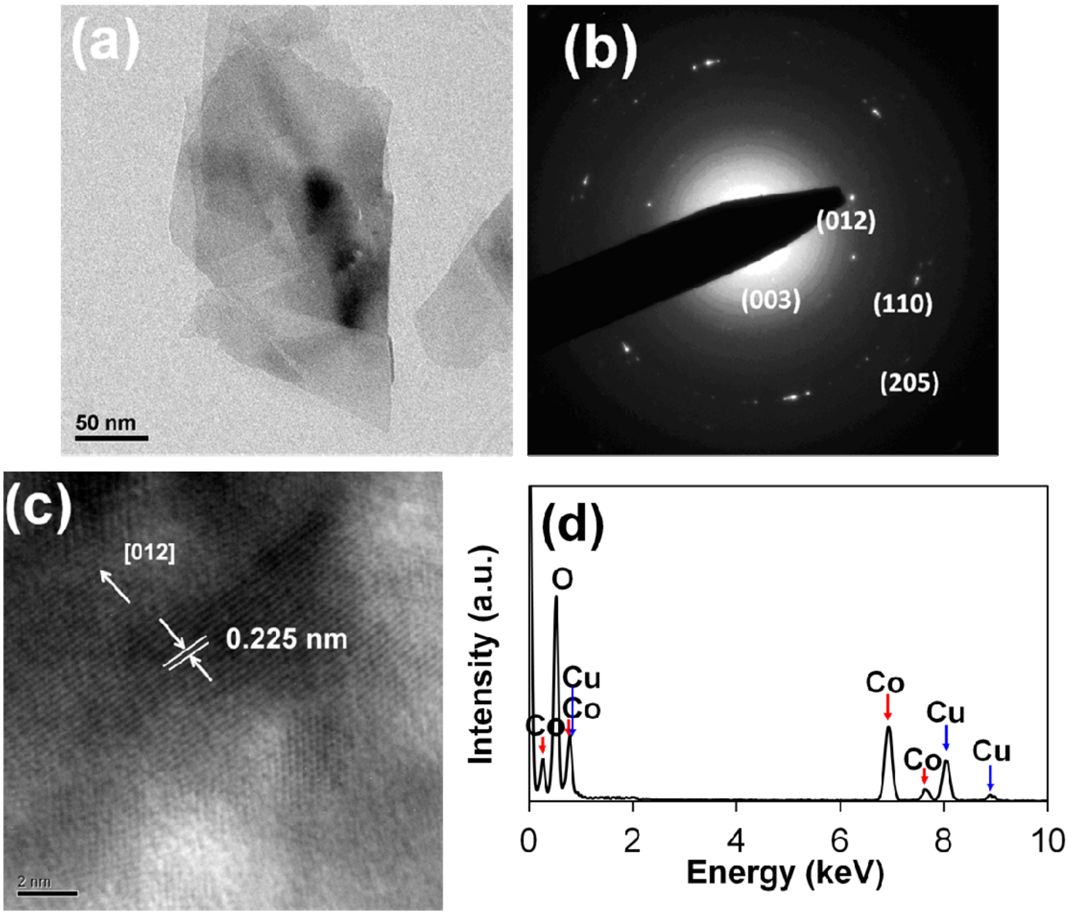

Figure 3.3. (a) TEM image of some isolated CoOOH nanosheets peeled off from the Co foil, (b) the corresponding SAED pattern and (c) typical HRTEM image. (d) The corresponding electron dispersive X-ray spectrum of the nanosheets.

In Figure 3.4, we attempted to monitor the evolution of reaction both visually and with UV-Vis absorption spectroscopy. It is noted that after ~2 hours of immersion in the alkaline solution, metallic cobalt on the substrate surface slowly dissolves to give the blue color of the solution. The corresponding UV-Vis spectra of the solutions (Figure 3.4b) illustrated the typical absorption spectra of tetrahedral Co^{2+}-complexes between 450 and 700 nm, arising from $^4F\ (\Gamma_2) \rightarrow {}^4P\ (\Gamma_4)$ transition that splits up due to (L, S) coupling effects[54]. After 5 hours, the appearance of precipitates increased the absorbance in all wavelengths as shown by the UV-Vis spectrum (420 min). Eventually, after 9 hours, the precipitates essentially blocked the light (UV-Vis spectrum at 540 min).

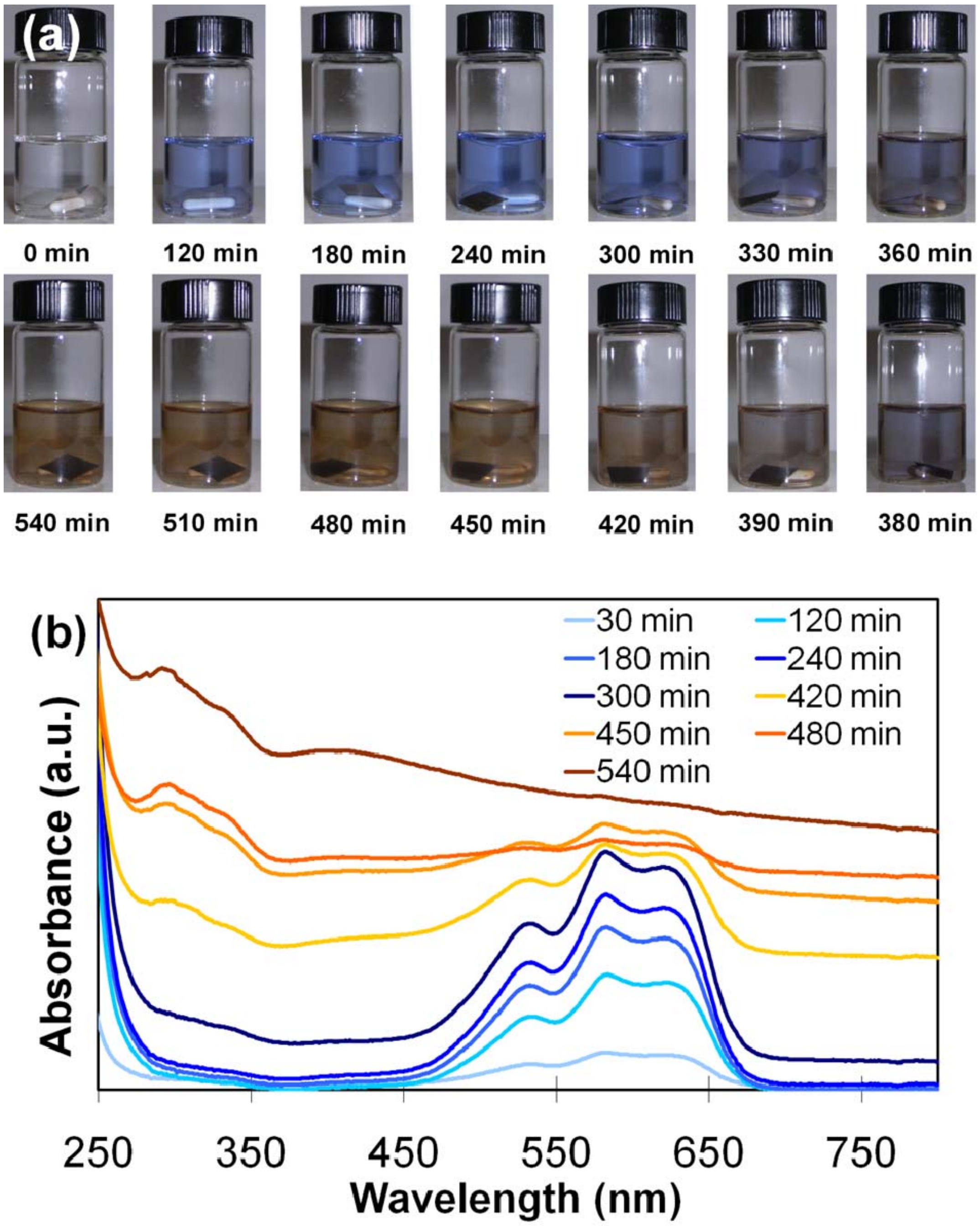

Figure 3.4. (a) Evolution of solution color during the growth of CoOOH on cobalt foil in 2.5 M NaOH solution monitored at various intervals; and (b) the corresponding UV-Vis spectra.

As shown by the potential-pH diagram of Co species[55], cobalt ions readily dissolves in an alkaline media yielding the blue colored $Co(OH)_4^{2-}$, which is illustrated from the increasing color intensity of the solution. In alkaline solution, $Co(OH)_4^{2-}$ is readily oxidized to insoluble brown CoOOH, which appeared as the final product. Furthermore, continuous magnetic stirring provided additional dissolved oxygen for the oxidation process. During the oxidation of $Co(OH)_4^{2-}$ to CoOOH, it can be observed that the blue color of the solution slowly disappears, followed by the formation of insoluble brown CoOOH. The proposed sequence of reaction is thus:

$$Co \rightarrow Co^{2+} + 2e^- \qquad (1)$$

$$Co^{2+} + 4OH^- \rightarrow Co(OH)_4^{2-} \qquad (2)$$

$$Co(OH)_4^{2-} \rightarrow CoOOH + H_2O + OH^- + e- \qquad (3)$$

In order to verify our proposed mechanism, we analyzed the brown precipitate formed in the solution. The sample was collected through filtration after the reaction, rinsed with distilled water and dried in air for a few days. SEM observation shows that the collected sample has the same nanosheet morphology as in Figure 3.1. The corresponding Raman spectrum also exhibits the same features as that of CoOOH nanosheet arrays formed on the cobalt foil. Thus, CoOOH nanosheets were formed via the proposed mechanism both in the solution and on the cobalt substrate.

3.3.2 Thermal conversion of CoOOH to Co_3O_4 nanosheets

The possibility of using the as-synthesized CoOOH nanosheets as a precursor template to produce nanostructures of cobalt oxide was explored. In the literature, Figlarz *et al.*[56] have found that hexagonal Co_3O_4 was obtained by the decomposition of CoOOH at approximately 250 °C, while Yang *et al.*[50] have demonstrated that CoOOH decomposed to Co_3O_4 at 252 °C via thermogravimetric analysis. They both suggested that the thermal decomposition reaction involved is: 12 CoOOH → 4 Co_3O_4 + O_2 + 6 H_2O.

Thus, the CoOOH nanosheets as prepared on Co foil above were heated on a ceramic hot plate at 300 °C for 4 h. SEM analysis (Figure 3.5a-d) indicated clearly there is no significant morphology change nor collapse of the nanosheets, even though the crystal structure has transformed from CoOOH to Co_3O_4 (as confirmed by XRD in Figure 3.6a). High resolution TEM image (Figure 3.5f) reveals lattice fringes with interplanar spacing of 0.286 nm, corresponding to the (220) lattice planes of the spinel Co_3O_4 structure.

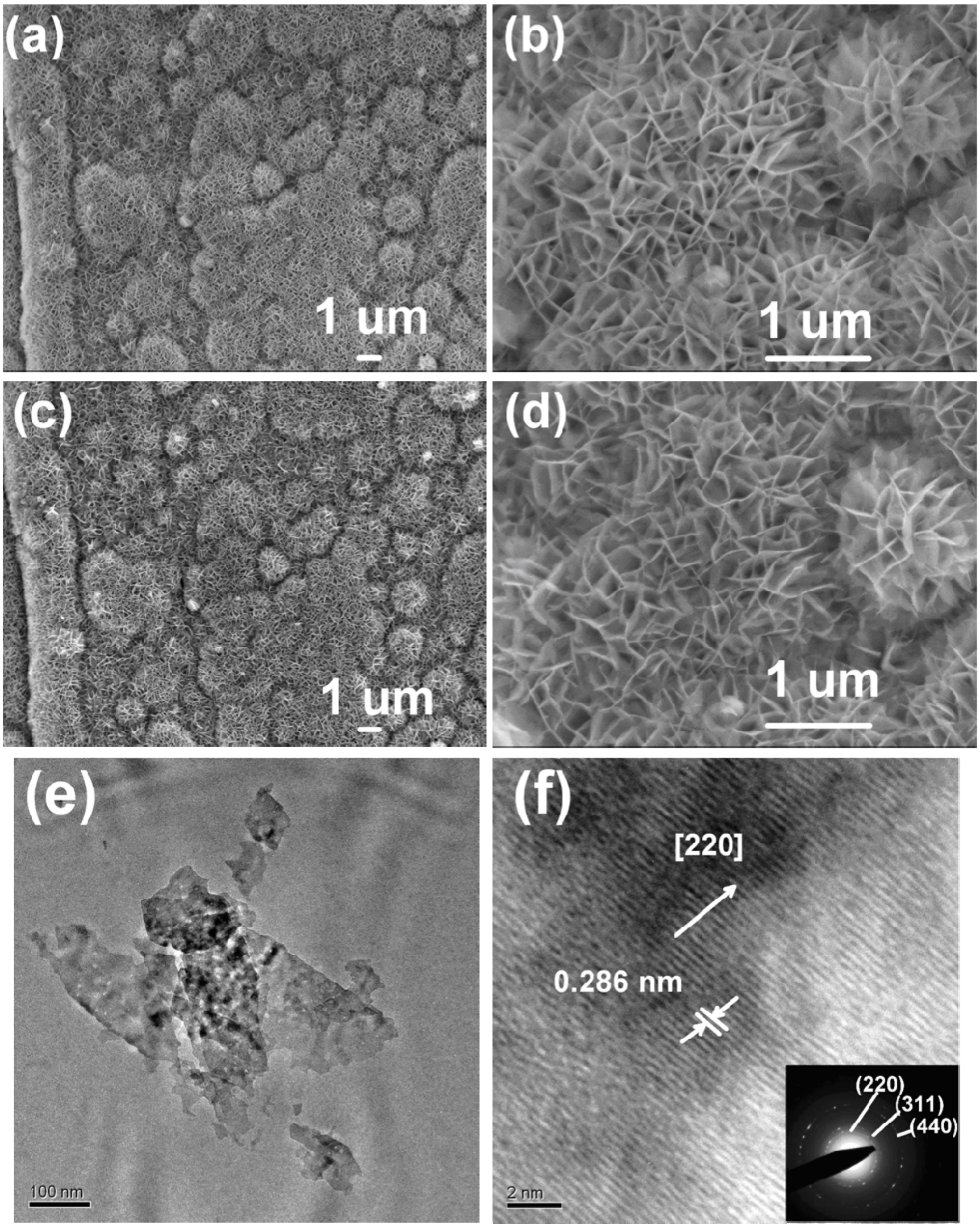

Figure 3.5. SEM images of the as-synthesized CoOOH nanosheet arrays before (a & b) and after (c & d) heat treatment at 300 °C for 4 h. The images were taken at the same spot of sample. (e) Low resolution TEM image showing the porosity and (f) HRTEM showing the lattice planes of the resultant Co_3O_4 product. Inset shows the SAED pattern.

The phase transformation from CoOOH to Co_3O_4 was confirmed by XRD, FTIR and Raman spectroscopy as shown in Figure 3.6. The Raman spectrum of the Co_3O_4 phase (Figure 3.6b) displays intense bands at 487, 525 and 693 cm^{-1} with a much weaker band at 620 cm^{-1}. These four prominent Raman peaks correspond to A_{1g} (693 cm^{-1}), F_{2g} (620 cm^{-1}), F_{2g} (525 cm^{-1}) and E_g (487 cm^{-1}) modes of crystalline Co_3O_4 phase according to report by Hadjiev *et al.*[57]. The FTIR spectrum of Co_3O_4 (Figure 3.6c) displays two distinct bands that originate from the stretching vibrations of the cobalt-oxygen bonds. The first band at 567 cm^{-1} is associated with the OCo^{3+} vibration in the spinel lattice, where Co^{3+} is located in an octahedral hole. The second band at 664 cm^{-1} is associated with the $Co^{2+}Co^{3+}O_3$ vibration, where Co^{2+} is located in a tetrahedral hole[58].

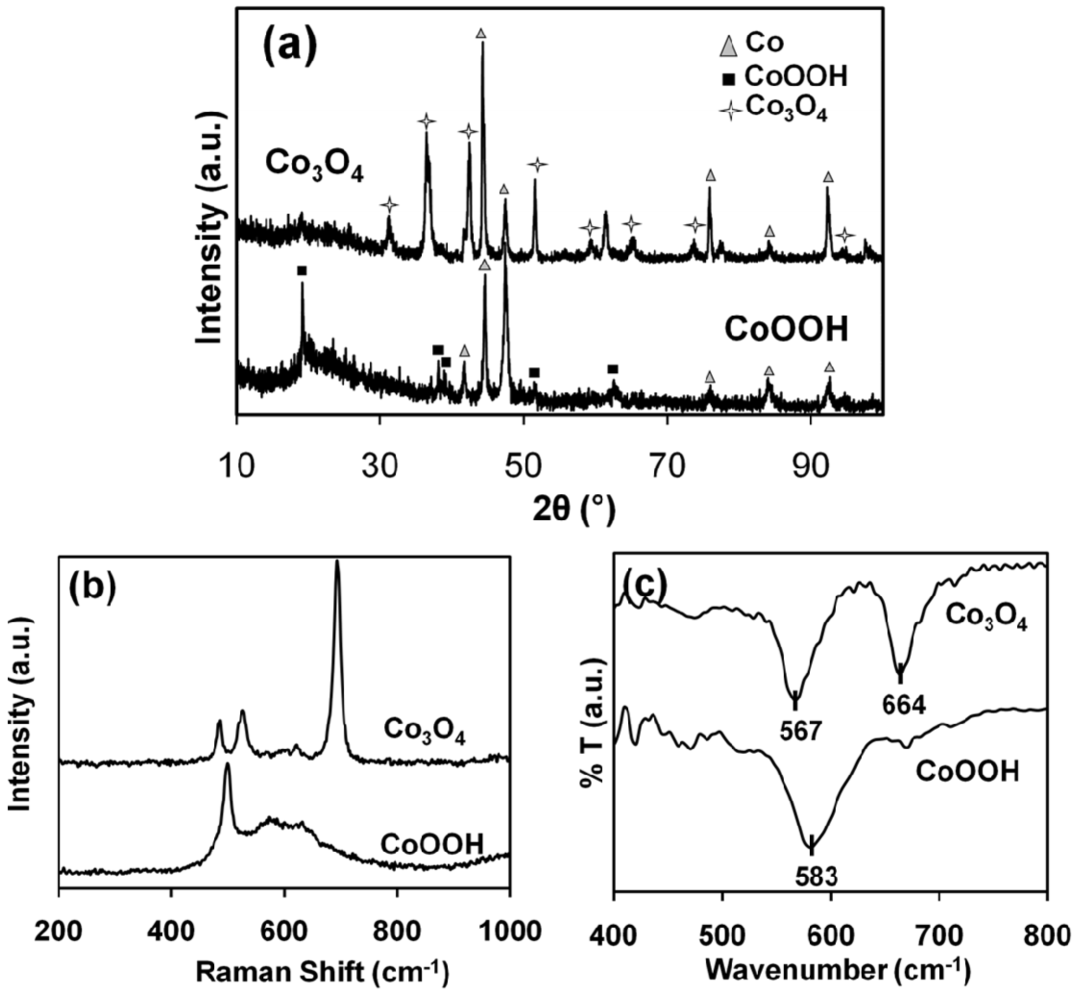

Figure 3.6. Comparison of the (a) XRD patterns, (b) Raman spectra and (c) FTIR spectra of CoOOH nanosheets (before heat treatment) and Co_3O_4 sample (after heat treatment). The XRD patterns were indexed to Co (JCPDS 05-0727), CoOOH (JCPDS 07-0169) and Co_3O_4 (JCPDS 43-1003).

The Co $2p_{3/2}$ and O 1s XPS peaks of the CoOOH and Co_3O_4 nanosheet arrays are respectively shown in Figure 3.7. Typically, Co $2p_{3/2}$ signal shows a complex structure broaden by the multiplet splitting effect. It is also known that most cobalt oxides and hydroxides (i.e. CoO, Co_2O_3, Co_3O_4, and CoOOH) have rather similar binding energies (BE). Thus, assignment of cobalt oxidation states is commonly achieved through a detailed analysis of the Co 2p shake up structure at BE higher than the main $2p_{3/2}$ lines[59]. Since Co (II) compounds are high spin complexes (s = 3/2) while Co (III) compounds are diamagnetic (s = 0), Co (II) compounds generally show intense shake-up satellites, whereas these additional broad peaks are absence for diamagnetic Co (III) complexes[60, 61]. In Figure 3.7a, the Co $2p_{3/2}$ signal of CoOOH sample exhibits an asymmetric peak at ~780.5 eV, without any shake-up structure. While at similar BE, the Co $2p_{3/2}$ signal of the Co_3O_4 sample (Figure 3.7b) displays a relatively more significant tail at higher BE, indicating the mixed Co^{3+} and Co^{2+} oxidation state. The O 1s XPS peaks of the two samples are clearly distinct and consistent with the recently reported XPS peaks of CoOOH and Co_3O_4 nanoplates prepared via precipitation method[50]. The broader O 1s peak of CoOOH (Figure 3.7c) can be curve-fitted to three components. The two intense peaks at 531.3 eV and 530.1 eV correspond to the hydroxyl oxygen and the oxide oxygen, respectively. Area analysis of these two types of oxygen gave 1:1 ratio, which is consistent with their atomic ratio in CoOOH. The intense O 1s peak at BE 530.2 eV for Co_3O_4 (Figure 3.7d) is attributable to oxygen species in the spinel cobalt oxide phase. The weak tailing off at higher BE may be due to the presence of small amount of hydroxyl species absorbed on the surface.

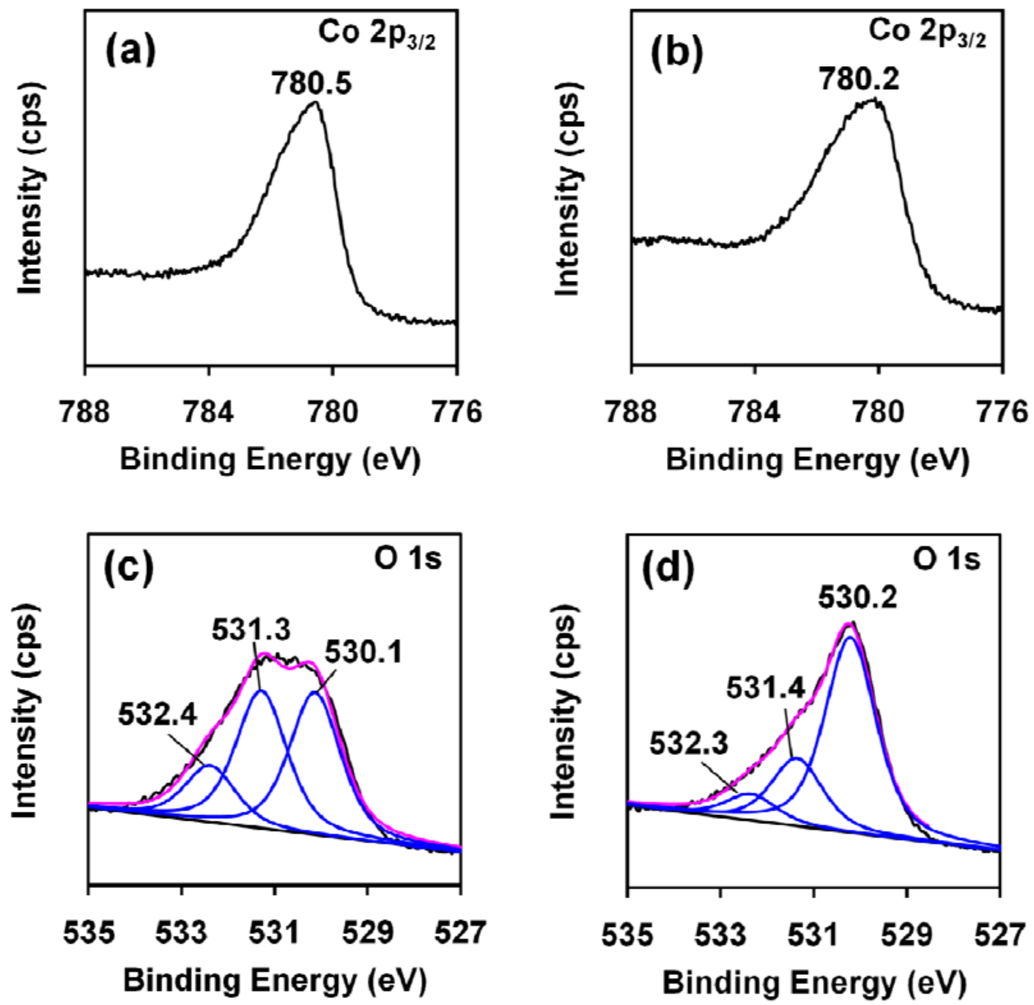

Figure 3.7. XPS measurements of Co $2p_{3/2}$ (upper spectra) and O 1s (lower spectra) core levels for CoOOH (a and c) and Co_3O_4 (b and d) nanosheet arrays, respectively.

3.3.3 Comparative electrochemical studies of CoOOH and Co_3O_4 nanosheets

CV curves of CoOOH and Co_3O_4 electrodes scanned in NaOH of different concentrations (0.5, 1, 3 and 6 M) are presented in Figure 3.8. It is observed that by decreasing the electrolyte concentration, both the anodic and cathodic peak potentials shift toward the positive direction. Correspondingly, the potential associated to the start of oxygen evolution reaction (OER) for both electrodes increased obviously. For instance, the OER potential (estimated as the potential when the current achieved 1.2 mA) for the Co_3O_4 electrode is about 0.48 V in 6 M KOH, whereas it is about 0.58 V in 0.5 M KOH. As the energy density (*E*) of an electrochemical capacitor is proportional to the square of potential window (i.e. E = *specific capacitance* × $\Delta V^2/2$), the use of NaOH at lower concentration is preferred so as to enlarge the working potential window. In order to achieve an optimum electrochemical performance when choosing electrolyte concentration, a balance between the working potential window, stability of electrode and the capacitance should be considered. Based on these considerations, subsequent electrochemical studies were performed by using 0.5 M NaOH for CoOOH electrode at working potential of -0.15 to 0.55 V, and 3 M NaOH for Co_3O_4 electrode at working potential of -0.15 to 0.48 V.

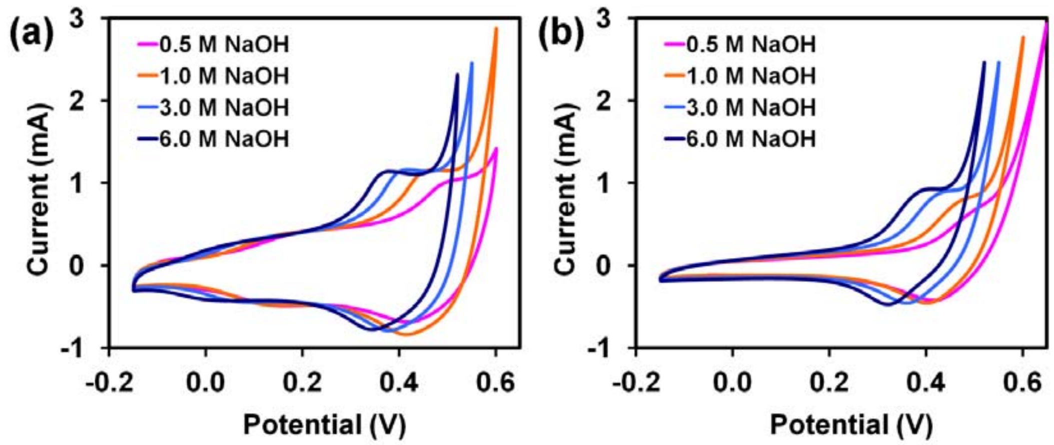

Figure 3.8. CV curves obtained using (a) CoOOH and (b) Co_3O_4 electrodes in NaOH electrolyte of different concentrations scanned at 10 mV/s.

To further evaluate the relationship between scan rate/(scan rate)$^{1/2}$ and cathodic peak currents, the CV curves at different scan rates for CoOOH and Co_3O_4 electrodes were obtained in 0.5 M and 3 M NaOH, respectively (Figure 3.9). For CoOOH electrode, there are two observable cathodic peaks, c1 and c2, corresponding to redox couples $Co^{3+} \leftrightarrow Co^{4+}$ and $Co^{2+} \leftrightarrow Co^{3+}$. As shown in Figure 3.9c (upper), the cathodic peak currents for c1 (i_{pc1}) presented a linear relationship with the square root of scan rates ($v^{1/2}$) in the range of 10 to 150 mV/s (the peak currents are unclear for 175 and 200 mV/s), indicating a diffusion-controlled electrochemical process. Meanwhile, the cathodic peak currents for c2 (i_{pc2}) exhibited a linear relationship with the scan rates (v) as depicted in Figure 3.9c (lower). In addition, the plot of log (i_{pc2}) against log (v) is linear with a slope of about 1, which is an ideal value of surface-controlled electrochemical process. For the Co_3O_4 electrode, only one cathodic peak is observable from the CV curves. Both the plots of cathodic peak currents (i_{pc}) against the square root of scan rates ($v^{1/2}$) and i_{pc} against scan rates are shown in Figure 3.9d. At lower scan rates (10 to 75 mV/s), the i_{pc} appeared linear to $v^{1/2}$; while at higher scan rates (> 100 mV/s), the i_{pc} appeared linear to v, showing two different electrochemical processes dominating at different regions of scan rates.

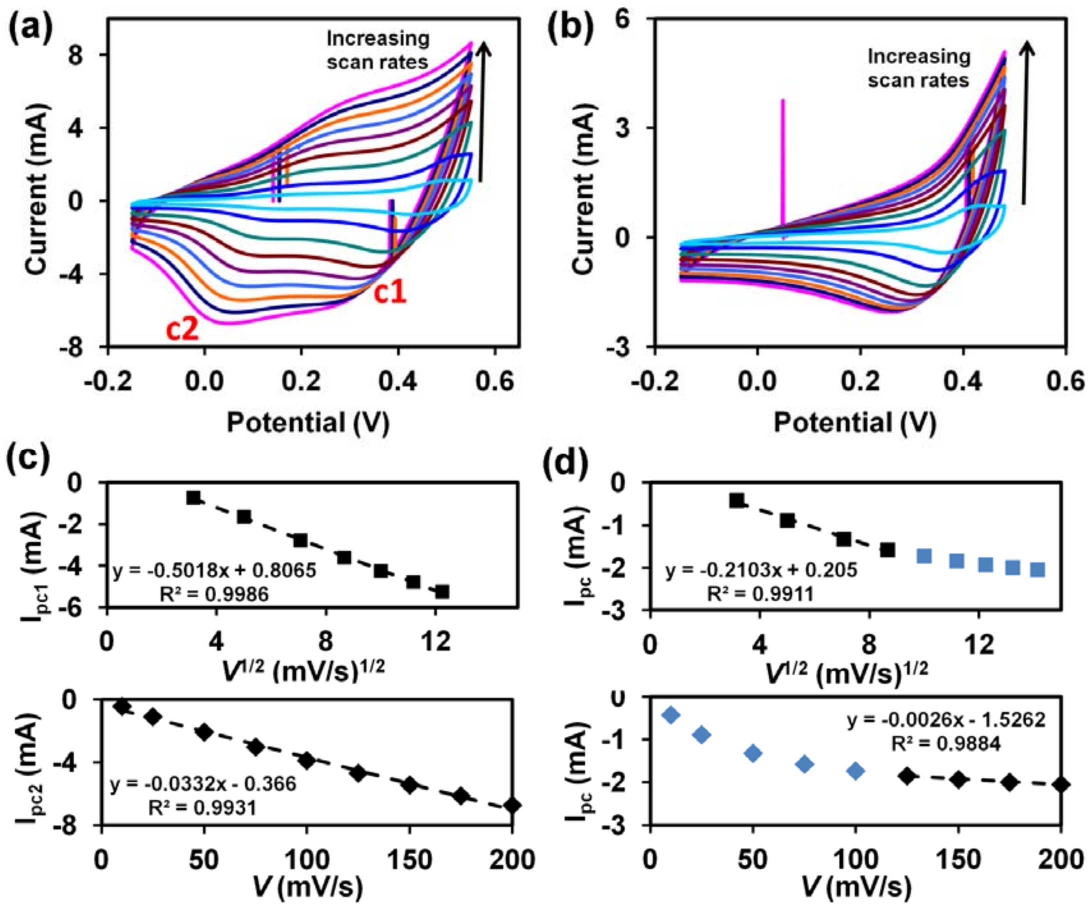

Figure 3.9. CV curves of (a) CoOOH electrode in 0.5 M NaOH and (b) Co_3O_4 electrode in 3 M NaOH electrolyte scanned at different scan rates; (c) Cathodic peak currents I_{pc1} and I_{pc2} of CoOOH obtained at different scan rates were plotted against (scan rate)$^{1/2}$ and scan rate, respectively, and their corresponding linear curves; (d) Cathodic peak currents (I_p) of Co_3O_4 obtained at different scan rates were plotted against (scan rate)$^{1/2}$ and scan rate.

Figure 3.10a and b present the galvanostatic charge-discharge curves of CoOOH and Co_3O_4 electrodes at different current densities. The areal capacitances of the electrodes were calculated based on the galvanostatic charge-discharge curves and presented in Figure 3.10c. Comparatively, the CoOOH electrode shows a much higher areal capacitance than Co_3O_4. At current density of 0.5 mA/cm^2, the areal capacitances for CoOOH and Co_3O_4 electrodes were 74.5 and 34.8 mF/cm^2, respectively. Additionally, when the current density was increased ten times to 5 mA/cm^2, the areal capacitances for CoOOH and Co_3O_4 electrodes dropped to 58.3

and 15.8 mF/cm^2, respectively. The capacitance retention for the CoOOH and Co_3O_4 electrodes were 78 % and 45 % at 5 mA/cm^2, indicating a much better rate capability of CoOOH electrode. This comparative result shows that the CoOOH electrode possessed a more efficient charge transfer during the electrochemical processes.

Cycling studies were performed for a continuous 5000 cycles for both the CoOOH and Co_3O_4 electrodes (Figure 3.10d). In 0.5 M NaOH, the CoOOH electrode suffered from a continuous loss of capacitance during extensive cycling. After 5000 cycles, the capacitance of the CoOOH electrode remained at 86 %. The galvanostatic charge-discharge curves at different cycles are shown in Figure 3.10e. It is noted that the shape of the charge-discharge curves is similar, suggesting the capacitance loss was not due to phase transformation but likely due to loss of active material via dissolution in the alkaline medium. In contrast, the Co_3O_4 electrode was very stable upon cycling in 3 M NaOH. After 5000 cycles, the areal capacitance increased 10 % from its original areal capacitance. The galvanostatic charge-discharge curves at the end of cycling were almost identical to the earlier cycles (Figure 3.10f).

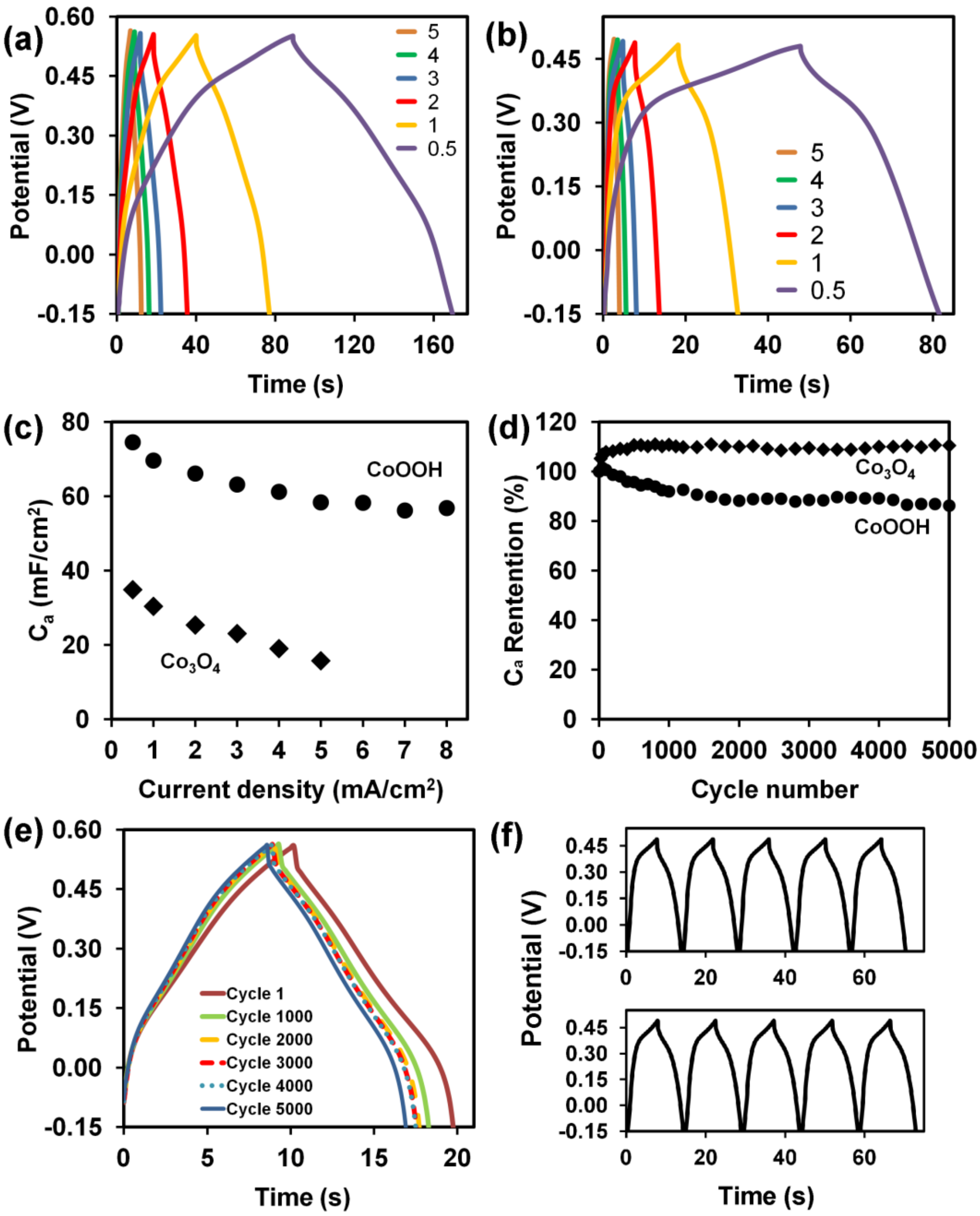

Figure 3.10. Typical galvanostatic charge-discharge profiles of (a) CoOOH and (b) Co_3O_4 electrodes at different current densities (mA/cm^2), (c) calculated areal capacitance of CoOOH and Co_3O_4 electrodes based on the galvanostatic discharge profiles, (d) Capacitance retention (cycling stability) of CoOOH (at a current density of 3 mA/cm^2) and Co_3O_4 (at a current density of 2 mA/cm^2) electrodes computed from the galvanostatic discharge curve for continuous 5000 cycles, (e) comparison of galvanostatic charge-discharge profiles of CoOOH electrode at different cycles, (f) comparison of galvanostatic charge-discharge profiles of Co_3O_4 electrode at cycle 100-105 and cycle 4995-5000. Note: all electrochemical studies of CoOOH electrodes were performed in 0.5 M NaOH.

3.4 Conclusions

A simple synthesis method was developed to fabricate CoOOH nanosheets directly on cobalt substrates via alkaline oxidation. By monitoring the growth process visually and spectroscopically, the formation sequences of CoOOH was elucidated. The CoOOH nanosheets can be thermally converted to Co_3O_4 nanosheets via a topotactic transformation, retaining the original sheet-like morphology. Both compounds were characterized comprehensively via various techniques. As the compounds were of similar morphology but different chemical phases, it provides a good basis to study the comparative electrochemical properties of the compounds. Optimum working potential window and concentration of electrolyte were obtained by studying the CV curves. Meanwhile, the CV curves at different scan rates were applied to analyze the electrochemical processes for the CoOOH and Co_3O_4 electrodes. Comparatively, CoOOH electrode exhibited much higher areal capacitance and better rate capability than Co_3O_4 electrode.

3.5 References

1. P. Simon and Y. Gogotsi, *Nat. Mater.*, 2008, **7**, 845-854.
2. Y. Zhang, H. Feng, X. Wu, L. Wang, A. Zhang, T. Xia, H. Dong, X. Li and L. Zhang, *Int. J. Hydrogen Energy*, 2009, **34**, 4889-4899.
3. C. Liu, F. Li, L.-P. Ma and H.-M. Cheng, *Adv. Mater.*, 2010, **22**, E28-E62.
4. L. Cao, F. Xu, Y. Y. Liang and H. L. Li, *Adv. Mater.*, 2004, **16**, 1853-1857.
5. V. Gupta, T. Kusahara, H. Toyama, S. Gupta and N. Miura, *Electrochem. Commun.*, 2007, **9**, 2315-2319.
6. C. Yuan, X. Zhang, B. Gao and J. Li, *Mater. Chem. Phys.*, 2007, **101**, 148-152.
7. P. K. Nayak and N. Munichandraiah, *J. Electrochem. Soc.*, 2008, **155**, A855-A861.
8. S.-L. Chou, J.-Z. Wang, H.-K. Liu and S.-X. Dou, *J. Electrochem. Soc.*, 2008, **155**, A926-A929.
9. Q. D. Wu, S. Liu, S. M. Yao and X. P. Gao, *Electrochem. Solid-State Lett.*, 2008, **11**, A215-A218.
10. W.-J. Zhou, J. Zhang, T. Xue, D.-d. Zhao and H.-l. Li, *J. Mater. Chem.*, 2008, **18**, 905-910.

11. Z.-A. Hu, Y.-L. Xie, Y.-X. Wang, L.-J. Xie, G.-R. Fu, X.-Q. Jin, Z.-Y. Zhang, Y.-Y. Yang and H.-Y. Wu, *J. Phys. Chem. C*, 2009, **113**, 12502-12508.
12. Z. Hu, L. Mo, X. Feng, J. Shi, Y. Wang and Y. Xie, *Mater. Chem. Phys.*, 2009, **114**, 53-57.
13. W.-J. Zhou, M.-W. Xu, D.-D. Zhao, C.-L. Xu and H.-L. Li, *Microporous Mesoporous Mater.*, 2009, **117**, 55-60.
14. J.-K. Chang, C.-M. Wu and I. W. Sun, *J. Mater. Chem.*, 2010, **20**, 3729-3735.
15. C. Lin, J. A. Ritter and B. N. Popov, *J. Electrochem. Soc.*, 1998, **145**, 4097-4103.
16. T. C. Liu, W. G. Pell and B. E. Conway, *Electrochim. Acta*, 1999, **44**, 2829-2842.
17. H.-K. Kim, T.-Y. Seong, J.-H. Lim, W. Ii Cho and Y. Soo Yoon, *J. Power Sources*, 2001, **102**, 167-171.
18. V. Srinivasan and J. W. Weidner, *J. Power Sources*, 2002, **108**, 15-20.
19. L. Cao, M. Lu and H. L. Li, *J. Electrochem. Soc.*, 2005, **152**, A871-A875.
20. V. R. Shinde, S. B. Mahadik, T. P. Gujar and C. D. Lokhande, *Appl. Surf. Sci.*, 2006, **252**, 7487-7492.
21. S. G. Kandalkar, J. L. Gunjakar and C. D. Lokhande, *Appl. Surf. Sci.*, 2008, **254**, 5540-5544.
22. G. Ji, Z. Gong, W. Zhu, M. Zheng, S. Liao, K. Shen, J. Liu and J. Cao, *J. Alloys Compd.*, 2009, **476**, 579-583.
23. S. Xiong, C. Yuan, X. Zhang, B. Xi and Y. Qian, *Chem. Eur. J.*, 2009, **15**, 5320-5326.
24. L. Cui, J. Li and X.-G. Zhang, *J. Appl. Electrochem.*, 2009, **39**, 1871-1876.
25. G. Wang, X. Shen, J. Horvat, B. Wang, H. Liu, D. Wexler and J. Yao, *J. Phys. Chem. C*, 2009, **113**, 4357-4361.
26. M-J. Deng, F-L. Huang, I-W. Sun, W-T. Tsai, J-K. Chang, *Nanotechnology*, 2009, **20**, 175602.
27. Y. Gao, S. Chen, D. Cao, G. Wang and J. Yin, *J. Power Sources*, 2010, **195**, 1757-1760.
28. E. Hosono, S. Fujihara, I. Honma, M. Ichihara and H. Zhou, *J. Power Sources*, 2006, **158**, 779-783.
29. H. Zheng, F. Tang, M. Lim, T. Rufford, A. Mukherji, L. Wang and G. Lu, *J. Power Sources*, 2009, **193**, 930-934.
30. H. Zheng, F. Tang, M. Lim, A. Mukherji, X. Yan, L. Wang and G. Q. Lu, *J. Power Sources*, 2010, **195**, 680-683.
31. F. Lichtenberg and K. Kleinsorgen, *J. Power Sources*, 1996, **62**, 207-211.
32. W. K. Hu, X. P. Gao, M. M. Geng, Z. X. Gong and D. Noréus, *J. Phys. Chem. B*, 2005, **109**, 5392-5394.
33. A. S. Arico, P. Bruce, B. Scrosati, J.-M. Tarascon and W. van Schalkwijk, *Nat Mater*, 2005, **4**, 366-377.
34. Y. Wang, H. Li, P. He, E. Hosono and H. Zhou, *Nanoscale*, 2010, **2**, 1294-1305.
35. Y. W. Zhu, T. Yu, F. C. Cheong, X. J. Xu, C. T. Lim, V. B. C. Tan, J. T. L. Thong and C. H. Sow, *Nanotechnology*, 2005, **16**, 88.
36. T. Yu, Y. W. Zhu, X. J. Xu, Z. X. Shen, P. Chen, C. T. Lim, J. T. L. Thong and C. H. Sow, *Adv. Mater.*, 2005, **17**, 1595-1599.

37. Y. Zhu, C. H. Sow, T. Yu, Q. Zhao, P. Li, Z. Shen, D. Yu and J. T. L. Thong, *Adv. Funct. Mater.*, 2006, **16**, 2415-2422.

38. T. Yu, Y. Zhu, X. Xu, K.-S. Yeong, Z. Shen, P. Chen, C.-T. Lim, J. T.-L. Thong and C.-H. Sow, *Small*, 2006, **2**, 80-84.

39. B. Varghese, C. H. Teo, Y. Zhu, M. V. Reddy, B. V. R. Chowdari, A. T. S. Wee, V. B. C. Tan, C. T. Lim and C. H. Sow, *Adv. Funct. Mater.*, 2007, **17**, 1932-1939.

40. M. V. Reddy, T. Yu, C. H. Sow, Z. X. Shen, C. T. Lim, G. V. Subba Rao and B. V. R. Chowdari, *Adv. Funct. Mater.*, 2007, **17**, 2792-2799.

41. B. Varghese, M. V. Reddy, Z. Yanwu, C. S. Lit, T. C. Hoong, G. V. Subba Rao, B. V. R. Chowdari, A. T. S. Wee, C. T. Lim and C.-H. Sow, *Chem. Mater.*, 2008, **20**, 3360-3367.

42. K. C. Chin, G. L. Chong, C. K. Poh, L. H. Van, C. H. Sow, J. Lin and A. T. S. Wee, *J. Phys. Chem. C*, 2007, **111**, 9136-9141.

43. K. C. Chin, C. K. Poh, G. L. Chong, J. Lin, C. H. Sow and A. T. S. Wee, *Appl. Phys. A*, 2008, **90**, 623-627.

44. Z. P. Xu and H. C. Zeng, *Chem. Mater.*, 1999, **11**, 67-74.

45. Z. P. Liu, R. Z. Ma, M. Osada, K. Takada and T. Sasaki, *J. Am. Chem. Soc.*, 2005, **127**, 13869-13874.

46. E. Hosono, S. Fujihara, I. Honma, M. Ichihara and H. S. Zhou, *J. Power Sources*, 2006, **158**, 779-783.

47. W. K. Hu, X. P. Gao, M. M. Geng, Z. X. Gong and D. Noreus, *J. Phys. Chem. B*, 2005, **109**, 5392-5394.

48. Y. Oaki and H. Imai, *Chem. Eur. J.*, 2007, **13**, 8564-8571.

49. J. H. Yang and T. Sasaki, *Chem. Mater.*, 2008, **20**, 2049-2056.

50. J. Yang, H. W. Liu, W. N. Martens and R. L. Frost, *J. Phys. Chem. C*, 2010, **114**, 111-119.

51. T. N. Ramesh, *Ind. Eng. Chem. Res.*, 2010, **49**, 1530-1533.

52. T. Pauporte, L. Mendoza, M. Cassir, M. C. Bernard and J. Chivot, *J. Electrochem. Soc.*, 2005, **152**, C49-C53.

53. C. W. Tang, C. B. Wang and S. H. Chien, *Thermochim. Acta*, 2008, **473**, 68-73.

54. H. Diegrubek and P. J. Plath, in *Stud. Surf. Sci. Catal.*, eds. N. I. J. P. J. P.A. Jacobs and G. Schulz-Ekloff, Elsevier, 1982, vol. Volume 12, pp. 23-32.

55. G. K. a. P. Schweitzer, L.L., *The Aqueous Chemistry of the Elements*, Oxford, 2010.

56. M. Figlarz, J. Guenot and F. Fievet-Vincent, *J. Mater. Sci.*, 1976, **11**, 2267-2270.

57. V. G. Hadjiev, M. N. Iliev and I. V. Vergilov, *J. Phys. C Solid State Phys.*, 1988, **21**, L199.

58. C.-W. Tang, C.-B. Wang and S.-H. Chien, *Thermochim. Acta*, 2008, **473**, 68-73.

59. W. F. S. J. F. Moulder, P. E. Sobol, K. D. Bomben, *Handbook of X-ray photoelectron spectroscopy: a reference book of standard spectra for identification and interpretation of XPS data*, Physical Electronics, 1992.

60. N. S. McIntyre and M. G. Cook, *Anal. Chem.*, 1975, **47**, 2208-2213.

61. I. G. Casella and M. R. Guascito, *J. Electroanal. Chem.*, 1999, **476**, 54-63.

Chapter 4 – CoOOH nanosheets electrode: Electrochemical sensing of glucose

4.1 Introduction

The development of reliable devices for monitoring glucose level has been driven since 1960s for diabetes control and treatment. Different approaches were devoted to the studies of amperometric sensors based on glucose oxidase (GOx) enzyme.[1] In spite of the low detection limit, enzymatic glucose sensors often suffer from stability issues originated from the nature of the enzymes.[2] This leads to the enormous interest in the development of enzymeless glucose sensors.[3] Enzymeless glucose sensors are expected to have advantages such as simplicity, reproducibility, good stability, and free from oxygen limitation. Various noble metals and their alloys have been explored for non-enzymatic glucose detection. However, high cost, low sensitivity, poor selectivity and poisoning by chloride ions have hindered their practical applications.

Recent advancement in the fabrication of nanomaterials has provided new platforms for both enzymatic and non-enzymatic glucose sensing applications.[4] Transition metal oxides significantly enhance the direct oxidation of glucose due to the catalytic effect originating from the multi-electron oxidation. Various nanostructured copper oxides[5-16] have been exploited to construct enzymeless glucose sensors. Recently, Ding et al.[17] reported the use of Co_3O_4 nanofibers for enzymeless glucose detection. They commented that the electrooxidation of glucose is mainly mediated by $CoOOH/CoO_2$ rather than $Co_3O_4/CoOOH$ in the alkaline medium. In this Chapter, we present the fabrication of an enzymeless amperometric sensor based on CoOOH nanosheets directly grown on cobalt substrate.

4.2 Electrochemical experiments

CoOOH nanosheets were formed on both sides of the cobalt substrate as described in Chapter 3. To prepare a conductive surface, one side of the sample was carefully removed by a 2 M HCl wetted wipers and cleaned. The conductive side was placed onto a circular gold plate, and sealed tightly in a Teflon holder with an O-ring of 1 cm diameter. Geometric electrode area of 0.785 cm^2 was used in all electrochemical experiments. A three-electrode cell was assembled with the CoOOH nanosheets as the working electrode, platinum wire as the counter electrode and Ag/AgCl as the reference electrode. All potentials were referenced to the Ag/AgCl (3 M KCl) electrode. NaOH aqueous solution (0.1 M) was used as the electrolyte. Hydrodynamic chronoamperometric measurements were carried out under magnetic stirring. All measurements were carried out using an Autolab PGSTAT 30 potentiostat/galvanostat at room temperature.

4.3 Results and Discussion

4.3.1 Electrochemical events of CoOOH nanosheets

4.3.1.1 Co (III) ↔ Co (IV)

As noted by various authors in the literature, the electrochemical behavior of cobalt compounds in alkaline solution is rather complex. The observed voltammetric features are also dependent on experimental parameters such as scan rate, potential scan range, etc. In our case, the oxidation peak of Co (III) is less obvious due to the parameters chosen.

As shown in Figure 4.1a, when the CoOOH electrode is cycled to progressively more positive potential (up to 0.80 V vs. Ag/AgCl) at 10 mV/s, the Co

(III) oxidation peak becomes slightly more pronounced (as indicated by the broad arrow). It is noted that the oxidation of Co (III) to Co (IV) ($CoOOH \rightarrow CoO_2 + H^+ + e^-$) occurs preceding the oxygen evolution reaction (OER: $CoO_2 \rightarrow CoO + \frac{1}{2} O_2$). The latter is observable with a sharp increase of anodic current as well as gas bubbles formation at the electrode surface. It can be seen in Figure 4.1a that the sharp OER peak can obscure the less pronounced Co (III) oxidation peak, unless the potential range is scanned towards more positive potentials.

When the scan rate is further reduced to 5 mV/s and when the CoOOH electrode is cycled to 0.65V, it can be seen clearly in Figure 4.1b that the Co(III) oxidation peak become more pronounced as well. Furthermore, it is noted that the cathodic peak associated with the reduction of Co (IV) to Co (III) becomes larger also when the electrode is cycled towards more positive potentials. This observation confirms that the less pronounced second oxidation peak is due to the incomplete oxidation of Co (III) to Co (IV) when the potential range was scanned only to 0.6 V.

4.3.1.2 Co (II) ↔ Co (III)

CoOOH consists mainly of trivalent cobalt ions, however, various polymorphs of CoOOH (e.g. β-, γ-) with slightly different stoichiometry can be obtained from various preparation methods.[18-19] In a structural study using synchrotron XRD and X-ray absorption fine structure (XAFS) analysis,[20] Morishita *et al.* found that the average oxidation states of cobalt in CoOOH heat-treated to different temperatures are: 2.840 (80°C), 3.222 (100°C), 3.264 (120°C), 3.241 (140°C) and 3.178 (160°C) respectively. While further XAFS study is required to confirm the oxidation state of Co in our prepared CoOOH samples, Morishita's report certainly suggested possibility of the occurrence of Co (II) ions in CoOOH samples. Rough calculation shows that an oxidation state of 2.84 is equivalent to about 1/6 of the cobalt ions being in the Co^{2+} state.

Similar assignments for the redox pairs of Co (II) ↔ Co (III) and Co (III) ↔ Co (IV) can be found in anodic electrodeposited CoOOH film reported by Wang and Diao[21] and Gorenstein *et al.*[22].

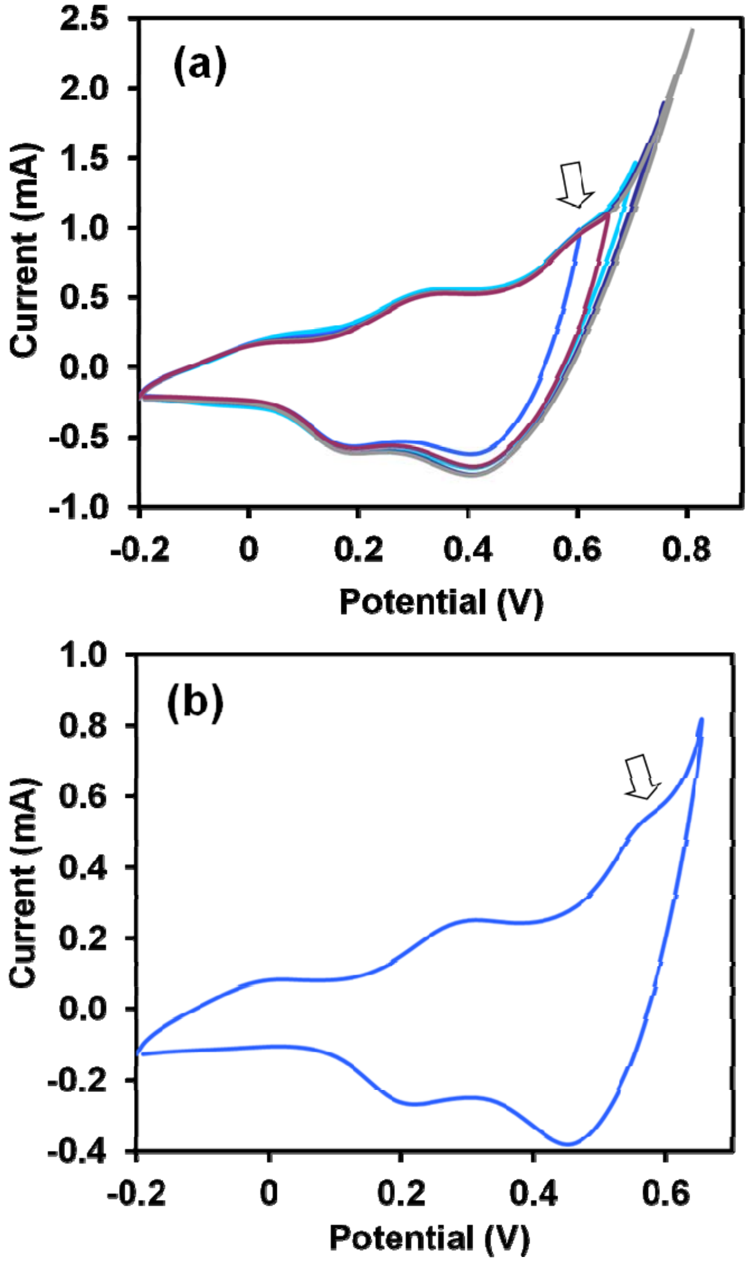

Figure 4.1. (a) CVs of CoOOH nanosheets electrode cycled to progressively more positive potential at scan rate of 10 mV/s, and (b) CV of CoOOH nanosheets electrode cycled to 0.65 V at low scan rate of 5 mV/s.

4.3.2 CoOOH nanosheets electrode as a glucose sensor

In this Section, the electrocatalytic activity of the CoOOH electrode towards the oxidation of glucose in an alkaline medium was investigated. Figure 4.2a presents the CV curves recorded at 10 mVs^{-1} in the absence or presence of glucose

(0.5 to 2.0 mM) in 0.1 M NaOH. While CoOOH is known to consist mainly of trivalent cobalt, non-stoichiometric phases of CoOOH often contain mixture Co^{2+}.[20] Thus, the redox pair appearing in the region of 0.2 V to 0.3 V can be assigned to the (quasi-)reversible redox process of Co^{2+} and Co^{3+}. Meanwhile, the increasing current from 0.4 V to 0.6 V is attributed to oxidation process of Co^{3+} to Co^{4+} (reduction shoulder at ~0.46V). Similar assignments have been suggested by Diao *et al.*[21] and Casella *et al.*[23-25]. It is clear that the CoOOH nanosheets exhibited obvious electro-oxidation of glucose starting from 0.30 V to 0.60 V upon the addition of glucose. It is well documented that glucose can be oxidized to produce gluconolactone through a 2-electron electrochemical reaction.[17, 23, 26]

Applied potentials of +0.40 V and +0.50 V were chosen to conduct enzymeless amperometric glucose sensing. A well-defined, stable and rapid change in current can be observed (Figure 4.2b) with the successive additions of 50 μM glucose. The CoOOH nanosheets exhibit sensitive and rapid current response to the glucose addition, achieving steady state current in less than 4s. As expected, the sensitivity is higher at 0.50 V applied potential compared to that at 0.40 V. However, the noise level is also higher in high glucose concentration at 0.50 V. The noise level may be associated with more intermediate species adsorbed onto the electrode due to the increased concentration and prolonged reaction time.

The amperometric current versus total glucose concentrations and the corresponding calibration curve of current versus concentration are presented in Figure 4.2c and d. The regression equation is I_{pa} (μA) = 27.588 + 0.7596c (μM), with R = 0.9967 for applied potential at +0.50 V and I_{pa} (μA) = 21.447 + 0.2680c (μM), with R = 0.9966 for applied potential at +0.40 V. At applied potential of +0.50 V, the sensor displays a linear range up to 500 μM, with a sensitivity of 967 $\mu AmM^{-1}cm^{-2}$ and a detection limit of 10.6 μM (signal/noise = 3). Larger linear range up to 700 μM was observed for amperometric response at +0.40 V with the sacrifice of sensitivity to 341 $\mu AmM^{-1}cm^{-2}$ and detection limit of 30.9 μM. For comparison, non-enzymatic glucose sensing performance based on various metal oxides/hydroxides from previous reports and our present study are shown in the Table 4.1. It is clear that the sensitivity of our CoOOH sensor is higher than most of previous studies.

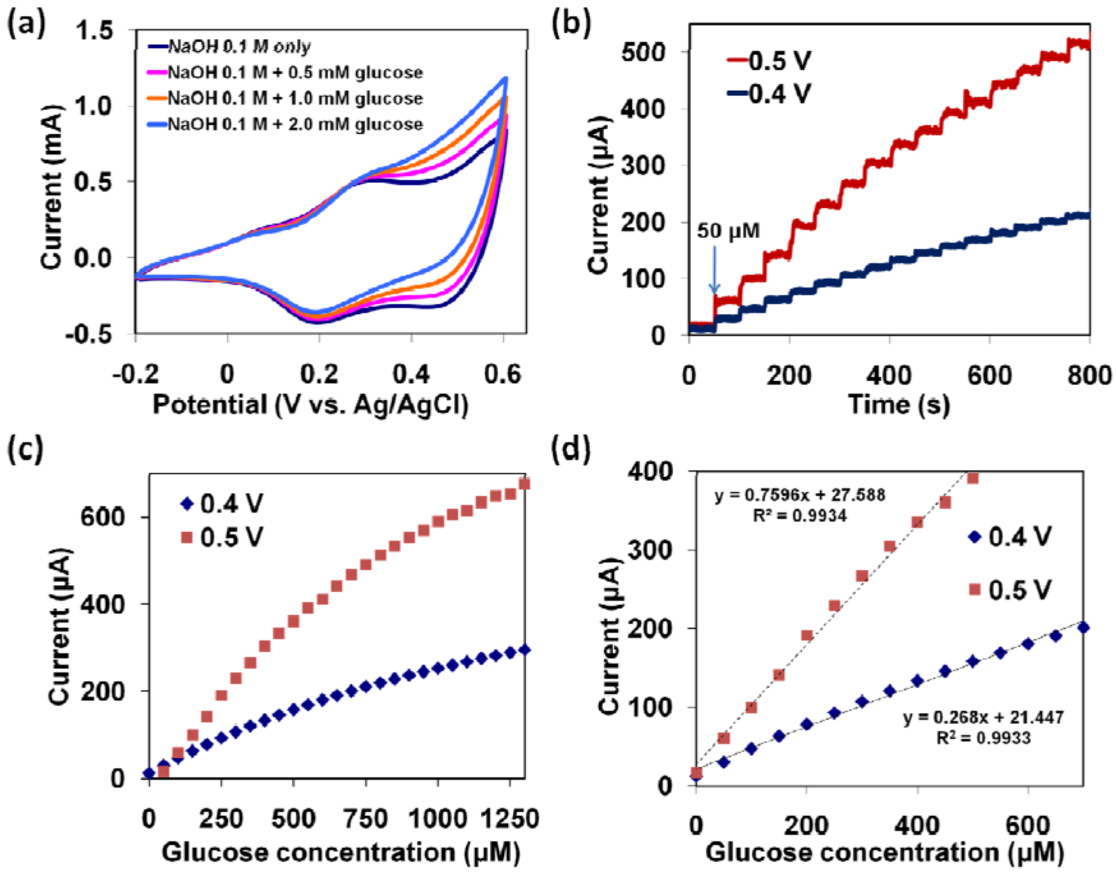

Figure 4.2. (a) CVs of CoOOH electrode in the absence or presence of glucose, (b) Amperometric responses of CoOOH electrode upon the successive addition of 50 μM glucose, (c) The amperometric current plotted vs. total glucose concentration, and (d) their corresponding linear calibration curves.

Table 4.1. Comparison of non-enzymatic glucose sensing performance based on different electrode materials of transition metal compounds.

Electrode materials	E (V vs. Ag/AgCl)	Sensitivity ($\mu AmM^{-1}cm^{-2}$)	Detection limit (μM) (S/N = 3)	Linear Range	Resp. times (s)	Ref.
CoOOH nanosheets	0.40 0.50	341 967	30.9 10.6	3×10^{-5} to 7.0×10^{-4} 1×10^{-5} to 5.0×10^{-4}	< 4	this study
Co_3O_4 nanofibers	0.59	36.25	0.97	1×10^{-6} to 2.04×10^{-3}	< 7	17
CuO nanospheres	0.60	404.53	1	1×10^{-6} to 2.55×10^{-3}	-	5
Pd (IV)-doped CuO nanofibers	0.30 (vs. SCE)	1061.4	0.019	2×10^{-7} to 2.5×10^{-3}	1	6
CuO nanofibers	0.40 (vs. SCE)	431.3	0.8	6×10^{-6} to 2.5×10^{-3}	~1	7
CuO nanorods CuO flowers	0.60	371.43 709.52	4 4	4×10^{-6} to 8×10^{-3}	< 10 ~ 15	8
CuO nanowires	0.33	490 μAmM^{-1}	0.049	4×10^{-7} to 2.0×10^{-3}	-	9
Cu_2O porous microcubes	0.60	-70.8 μAmM^{-1}	0.8	1.5×10^{-6} to 5.0×10^{-4}	< 4	10
CuO porous structures	0.65 (vs. Hg/HgO)	2900	0.14	1×10^{-6} to 2.5×10^{-3}	< 3	11
Anodised CuO	0.70	761.9	1	2×10^{-6} to 2×10^{-2}	< 1	12
Cu-CuO nanowire composites	0.30 (vs. SCE)	8.59	50	1×10^{-4} to 1.2×10^{-2}	< 5	13
Anodised CuO/C_xCuO_y	0.70	1890	0.05	2×10^{-6} to 1.5×10^{-2}	< 1	14
Cu_xO flowers	0.50	1620	49	4.9×10^{-5} to 6.0×10^{-3}	-	15
CuO nanowalls	0.20 (vs. SCE)	556.3	0.05	5×10^{-8} to 1.0×10^{-5}	< 10	16
FeOOH nanowires	≈0.40* (vs. SCE)	12.13 μAmM^{-1}	15	1.5×10^{-5} to 3×10^{-3}	-	29

4.3.3 The performance of CoOOH electrode in the presence of chloride

It has been reported that the presence of chloride ions in the solution can greatly affect the performance of non-enzymatic sensors especially for noble-metals.[2] The possibility of chloride ion poisoning to the CoOOH nanosheets electrode is thus examined by the addition of sodium chloride (0.1 M). As shown in

Figure 4.3a and b, the amperometric response at 0.50 V was found to remain almost constant, demonstrating that the electrode is still active towards glucose in the presence of chloride ions. Notably, the results show that the current response is faster in the presence of chloride, probably due to the increased ionic strength and conductivity of the electrolyte with sodium chloride.

4.3.4 The performance of CoOOH electrode in the presence of interfering compounds

Amperometric studies with successive addition of 1 mM phosphate buffer in 0.1 M NaOH containing 0.5 mM glucose were performed (Figure 4.3c). Significant linear rise in current response is observed only when the phosphate concentration is more than 11 mM. Additional analysis of the CoOOH electrode was performed in 0.1 M phosphate buffer solution (pH 7.4). Light purplish precipitate can be found on the electrode surface, likely due to the formation of insoluble cobalt phosphate on the electrode during electrochemical studies.[27] Since the normal range of phosphate content in blood sample is within 0.8-1.5 mM, we could safely say that the CoOOH electrode is suitable for glucose sensing of blood samples. However, special caution needs to be taken when the electrode is used to measure glucose in samples with high phosphate content.

The anti-interference properties of the CoOOH electrode were further investigated against uric acid and ascorbic acid. From the amperometric studies at +0.50 V, 0.04 mM uric acid (8 %) added in 0.5 mM glucose leads to 9 % increase of current, while 0.015 mM ascorbic acid (3 %) results in further 12 % increase of current. From these results, interferences of uric acid and ascorbic acid to the

CoOOH electrode cannot be denied. The interferences are minimized, however, in normal physiological conditions.

4.3.5 Effect of electrolyte concentration and reproducibly of CoOOH electrode

The effect of NaOH concentrations and pH are studied in amperometric measurements at constant glucose concentration. The amperometric currents drop correspondingly when the electrolyte concentration is reduced from 0.1 to 0.005 M (Figure 4.3d). In the Figure 4.3d, the bars are referred to left y-axis (current, μA) while the scattered symbols are referred to right y-axis (pH). The result shows that concentrated OH^- ions are important for the electrooxidation of glucose. Besides the significant lowering in amperometric responses, CV studies also indicate positive shifts of the redox couple, meaning higher applied potential is needed for amperometric sensing.

For intra-electrode reproducibility, the relative standard deviation (RSD) of repeated measurements (n = 5) is estimated to be 8.7 % for 50 μM glucose. Furthermore, the inter-electrode reproducibility (n = 3) is measured as RSD of 4.2 % in the current response to 0.4 mM glucose addition.

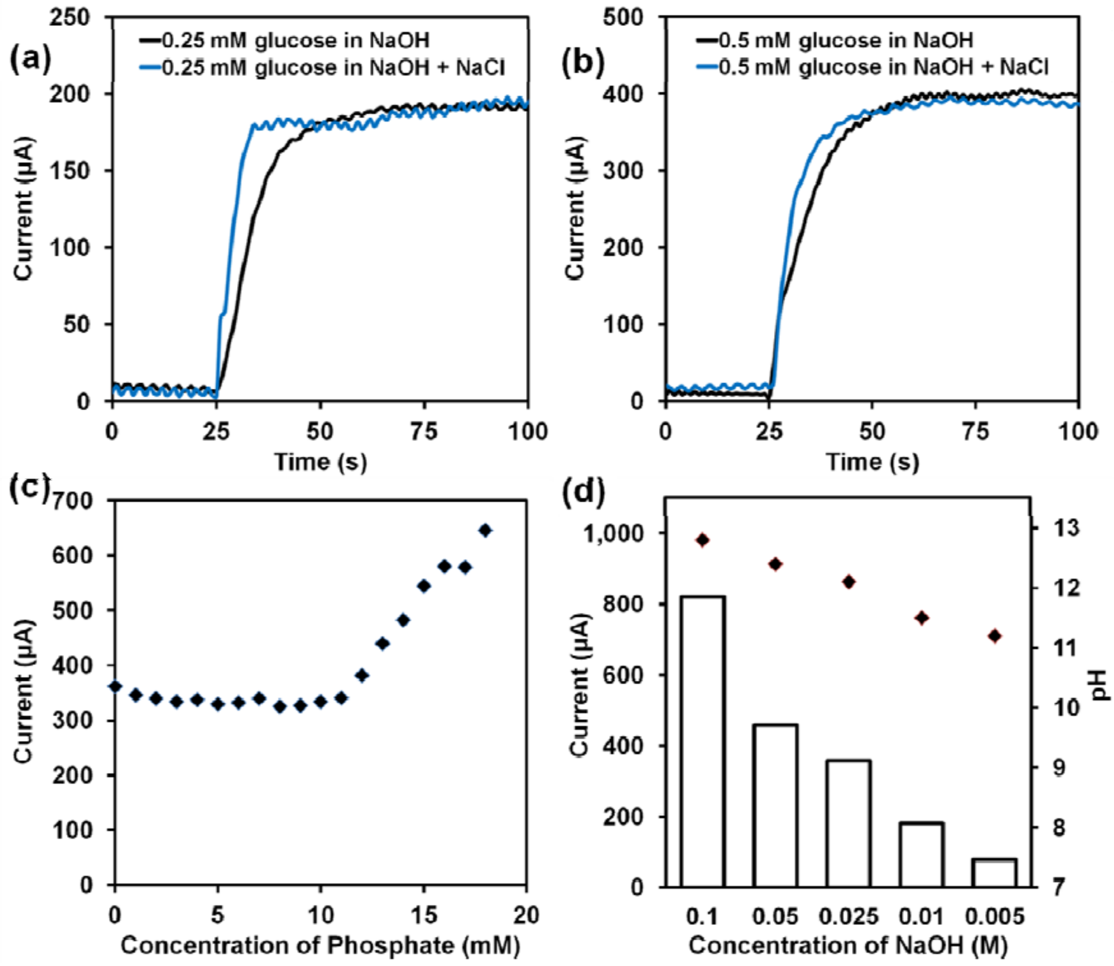

Figure 4.3. Amperometric responses of CoOOH electrode (a, b) with the addition of 0.25 mM and 0.5 mM glucose in the absence or presence of 0.1 M NaCl (in 0.1 M NaOH), (c) to the successive addition of phosphate, (d) at different NaOH concentrations and pH.

4.4 Conclusions

A non-enzymatic sensor made of CoOOH nanosheets grown directly on a cobalt substrate has been constructed. Despite the relatively narrow linear range (up to 500 μM), the sensor demonstrates low detection limit, rapid response, high sensitivity and is found to be free from chloride ion poisoning. While further studies are required to optimize the performance especially to widen the linear detection range, the CoOOH nanosheets may be applied as an electrocatalyst in glucose-based fuel cells.[28] It is anticipated that this study will motivate further studies on non-enzymatic glucose sensors in two dimensions: first is in the application of various cobalt species in glucose detection, and the secondly, the strategy to grow *in situ* nanostructures of metal oxides/oxyhydroxides on their parent metal substrates such as iron.[29,30]

4.5 References

1. J. Wang, Chem. Rev. 108 (2008) 814-825.
2. S. Park, H. Boo, T. D. Chung, Anal. Chim. Acta 556 (2006) 46-57.
3. K. E. Toghill, R. G. Compton, Int. J. Electrochem. Sci. 5 (2010) 1246-1301.
4. M. M. Rahman, A. J. S. Ahammad, J. H. Jin, S. J. Ahn, J. J. Lee, Sensors 10 (2010) 4855-4886.
5. E. Reitz, W. Jia, M. Gentile, Y. Wang, Y. Lei, Electroanal. 20 (2008) 2482-2486.
6. W. Wang, Z. Li, W. Zheng, J. Yang, H. Zhang, C. Wang, Electrochem. Comm. 11 (2009) 1811-1814.
7. W. Wang, L. Zhang, S. Tong, X. Li, W. Song, Biosens. Bioelectron. 25 (2009) 708-714.
8. X. Wang, C. Hu, H. Liu, G. Du, X. He, Y. Xi, Sensor Actuat. B 144 (2010) 220-225.
9. Z. Zhuang, X. Su, H. Yuan, Q. Sun, D. Xiao, M. M. F. Choi, Analyst 133 (2008) 126–132.
10. L. Zhang, H. Li, Y. Ni, J. Li, K. Liao, G. Zhao, Electrochem. Comm. 11 (2009) 812-815.
11. S. Cherevko, C-H. Chung, Talanta 80 (2010) 1371-1377.
12. T. G. S. Babu, T. Ramachandran, B. Nair, Microchim. Acta 169 (2010) 49-55.
13. G. Wang, T. Wei, W. Zhang, X. Zhang, B. Fang, L. Wang, Microchim. Acta 168 (2010) 87-92.
14. T. G. S. Babu, T. Ramachandran, Electrochim. Acta 55 (2010) 1612-1618.
15. C. Li, Y. Su, S. Zhang, X. Lv, H. Xia, Y. Wang, Biosens. Bioelectron. 26 (2010) 903-907.
16. X. Zhang, A. Gu, G. Wang, Y. Wei, W. Wang, H. Wu, B. Fang, CrystEngComm. 12 (2010) 1120-1126.
17. Y. Ding, Y. Wang, L. Su, M. Bellagamba, H. Zhang, Y. Lei, Biosens. Bioelectron. 26 (2010) 542-548.
18. P. Benson, G.W.D. Briggs, W.F.K. Wynne-Jones, Electrochim. Acta 9 (1964) 275-280.
19. M. Butel, L. Gautier, C. Delmas, Solid State Ionics 122 (1999) 271-284.
20. M. Morishita, S. Ochiai, T. Kakeya, T. Ozaki, Y. Kawaeb, M. Watada, T. Sakai, J. Electrochem. Soc. 156 (2009) A366-A370.

21. J. Wang, P. Diao, Electrochim. Acta 56 (2011) 10159-10165.

22. A. Gorenstein, C. N. Polo da Fonseca, R. M. Torresi, Proc. SPIE Optical Materials Technology for Energy Efficiency and Solar Energy Conversion X, Vol.1536 (1991) 104-115.

23. T. R. I. Cataldi, A. Guerrieri, I. G. Casella, E. Desimoni, Electroanalysis 7 (1995) 305-311.

24. I. G. Casella, M. R. Guascito, Electrochim. Acta, 45 (1999) 1113-1120.

25. I. G. Casella, M. Gatta, J. Electroanal. Chem. 534 (2002) 31-38.

26. C. W. Kung, C. Y. Lin, Y. H. Lai, R. Vittal, K. C. Ho, Biosens. Bioelectron. 27 (2011) 125-131.

27. R. K. Meruva, M. E. Meyerhoff, Anal. Chem. 68 (1996) 2022-2026.

28. S. Kerzenmacher, J. Ducréeb, R. Zengerlea, F. von Stettena, J. Power Sources 182 (2008) 1-17.

29. C. Xia, W. Ning, Electrochem. Comm. 12 (2010) 1581-1584.

30. L. Siegert, D. K. Kampouris, J. Kruusma, V. Sammelselg, C. E. Banks, Electroanalysis 21 (2009) 48-51.

Chapter 5 – CoOOH nanosheets electrode: Electrochemical sensing of hydrogen peroxide and hydrazine

5.1 Introduction

H_2O_2 is a simple compound with great significance in various fields, such as chemical synthesis, food manufacturing, textile and paper bleaching, fuel cells, environmental, pharmaceutical and clinical applications. In living organism, H_2O_2 is a signaling molecule to regulate various biological processes, for examples vascular remodeling, immune cell activation, stomata closure and root growth[1]. Besides, H_2O_2 appears as a common by-product of diverse biochemical enzymatic reactions such as glucose oxidase, alcohol oxidase, cholesterol oxidase etc. On the other hand, N_2H_4 is widely used in fuel cells, rocket propulsion systems, corrosive inhibitors, dyes, emulsifiers etc. Nevertheless, N_2H_4 is a neurotoxin, carcinogen and mutagen that causing damages to human organs such as lungs, livers, kidneys, respiratory tract infection and central nervous systems[2].

Based on aforementioned reasons, efficient and sensitive quantification of H_2O_2 and N_2H_4 are of practical significance in the field of biosensing. Among many chemical analysis methods, electrochemical techniques are preferred and advantageous owing to their rapid, efficient, sensitive, simple and cost effective operation. Enzyme and protein modified electrodes have been employed as amperometric biosensors for H_2O_2. However, despite the low detection limit, enzymatic sensors are sensitive to temperature and pH, and often suffer from stability issues originated from the nature of the enzymes. Enzymeless sensors are expected to offer better stability, simplicity and reproducibly. Current research on electrochemical detection of H_2O_2 and N_2H_4 mainly focuses on electrode development to enhance the electron transfer kinetics and decrease the overpotential, thus to reduce interferences from other electroactive compounds.

Recent advancement in the fabrication of various nanostructured metal and metal oxides has provided new platforms for non-enzymatic sensing applications. Transition metal-based compounds significantly enhance the direct oxidation of various substrates due to the catalytic effect originating from the multi-electron oxidation. Furthermore, nanoscale materials can significantly enhance mass transport and provide high effective surface for electrocatalytic reactions. Various metal oxides such as manganese oxides [3-5], cobalt oxides [6, 7], nickel oxides [8], Ni and Co layered double hydroxides [9], iron oxides [10], copper oxides [11] have been reported to show electrocatalytic activity towards H_2O_2. A comprehensive coverage of different materials used for electrochemical sensing of H_2O_2 can be found in a timely review written by Chen et al. [1]. On the other hand, zinc oxide [2, 12, 13], manganese oxides [14], copper oxides [15, 16], iron oxides [17] have been employed as hydrazine sensors.

Conventionally, various electroactive materials are dispersed in solution with other matrix (e.g. Nafion for entrapment), deposited and dried onto a glassy carbon electrode for electrochemical sensing. However, entrapment matrix can introduce additional diffusion resistance and blockage of certain active sites. In this study, we demonstrate a direct growth of CoOOH nanomaterials on a conductive substrate. The as-synthesized nanomaterials are ready for use directly in H_2O_2 and N_2H_4 detection without further disperse-drop-dry procedures, thus simplifying the electrode preparation procedure. Benefiting from the large surface area of the nanosheets and self-supported structure, the prepared nanoscale electrode exhibits excellent electrocatalytic properties at very low applied potential in alkaline electrolyte. The high sensitivity, fast response, wide linear detection range and low detection limit of the electrode, along with the simple and straightforward preparation method, made this electrode promising for effective non-enzymatic sensors.

5.2 Electrochemical studies

The CoOOH nanosheets were formed on both sides of the cobalt substrate following procedures described in Chapter 3. To prepare a conductive surface, one side of the sample was carefully removed by a 2 M HCl wetted wipers and cleaned. The conductive side was placed onto a circular gold plate, and sealed tightly in a Teflon holder with an O-ring of 1 cm diameter (geometric area of electrode = 0.785 cm^2). A three-electrode cell was assembled with the CoOOH nanosheets as the working electrode, platinum wire as the counter electrode and Ag/AgCl as the reference electrode. All potentials were referenced to the Ag/AgCl (3 M KCl) electrode. NaOH aqueous solution (0.1 M) was used as the electrolyte. Chronoamperometric measurements were carried out under constant magnetic stirring. All measurements were carried out using an Autolab PGSTAT 30 potentiostat/galvanostat at room temperature.

5.3 Results and Discussion

5.3.1 Electrochemical sensing of H_2O_2 on CoOOH nanosheets

Electrocatalytic activity of the CoOOH electrode towards the oxidation of H_2O_2 in alkaline medium was investigated. Figure 5.1a presents the cyclic voltammograms (CVs) recorded at 10 mV/s in the absence or presence of H_2O_2 (0 to 30 mM) in 0.1 M NaOH. It is clear that the CVs exhibited obvious increase of current response starting at potential less than 0.1 V upon the addition of H_2O_2. This indicates that CoOOH nanosheets electrode has excellent electrocatalytic properties, possibly due to the large surface area and enhanced electron transfer of the nanostructures. The CoOOH nanosheets present a very low overpotential required for H_2O_2 oxidation, thus enabling low potential amperometric detection that is potentially free from other interferences. Notably, at a closer look, the addition of 20 mM H_2O_2 induced a significant rise of oxidative current compared to 10 mM H_2O_2, accompanying with a change of the shape of CV curves. The different CV curves could be attributed to a change in the electrocatalytic reaction conditions. At higher H_2O_2 concentrations (e.g. 20 and 30 mM), electrooxidation of H_2O_2 produces oxygen gas bubbles on the electrode surface. This gas evolution enhances the diffusion of H_2O_2 towards the electrode surface, thus displaying a significantly higher oxidative current [21]. Linear sweep voltammograms (LSVs) scanned at 50 mV/s shown in Figure 5.1b demonstrate the proportional increase of current responses with the successive addition of 2 mM H_2O_2.

As amperometry provides much better current sensitivity than CV and LSV, further studies were carried out using this method. Figure 5.1c shows the amperometric response of 0.5 mM H_2O_2 during a prolonged duration (1000 s) at different applied potential from 0 to 0.4 V. Rapid (less than 3 s) and well-defined current responses can be observed from the amperometric curves, as well as stable response throughout the prolonged duration. Applied potential of 0 and 0.1 V were chosen for further studies, considering the reasonably high and especially stable current response, lower background noise, possible inhibition effect of H_2O_2 and its oxidized products at higher applied potential. Figure 5d shows the amperometric current response at CoOOH electrode held at 0 V for successive addition of 0.5 mM H_2O_2, while Figure 5e shows the amperometric current response at CoOOH electrode held at 0.1 V for successive addition of 0.1 mM H_2O_2. Upon the addition of H_2O_2, a steady state current response was obtained in less than 3 s, demonstrating rapid, stable and efficient catalytic properties of the CoOOH nanosheets. Comparison of the two curves clearly demonstrates that significantly improved current response can be obtained by applying potential at 0.1 V. Figure 5.1f shows a linear plot between the steady current response and H_2O_2 concentration in the range up to 1.6 mM at 0.1 V applied potential. The fitted linear plot is I (μA) = (78 μAmM^{-1})[H_2O_2] + 6 μA with a R^2 of 0.995. The detection limit (signal to noise ratio of 3) and sensitivity determined from the calibration plot were 40 μM and 78 μAmM^{-1} (or 99 $\mu AmM^{-1}cm^{-2}$ when normalized to electrode area of 0.785 cm^2), respectively. The reproducibility of the CoOOH electrode was evaluated. The relative standard deviation (RSD) of subsequent five measurements is 3.84 % (n=5) for 1 mM H_2O_2 addition.

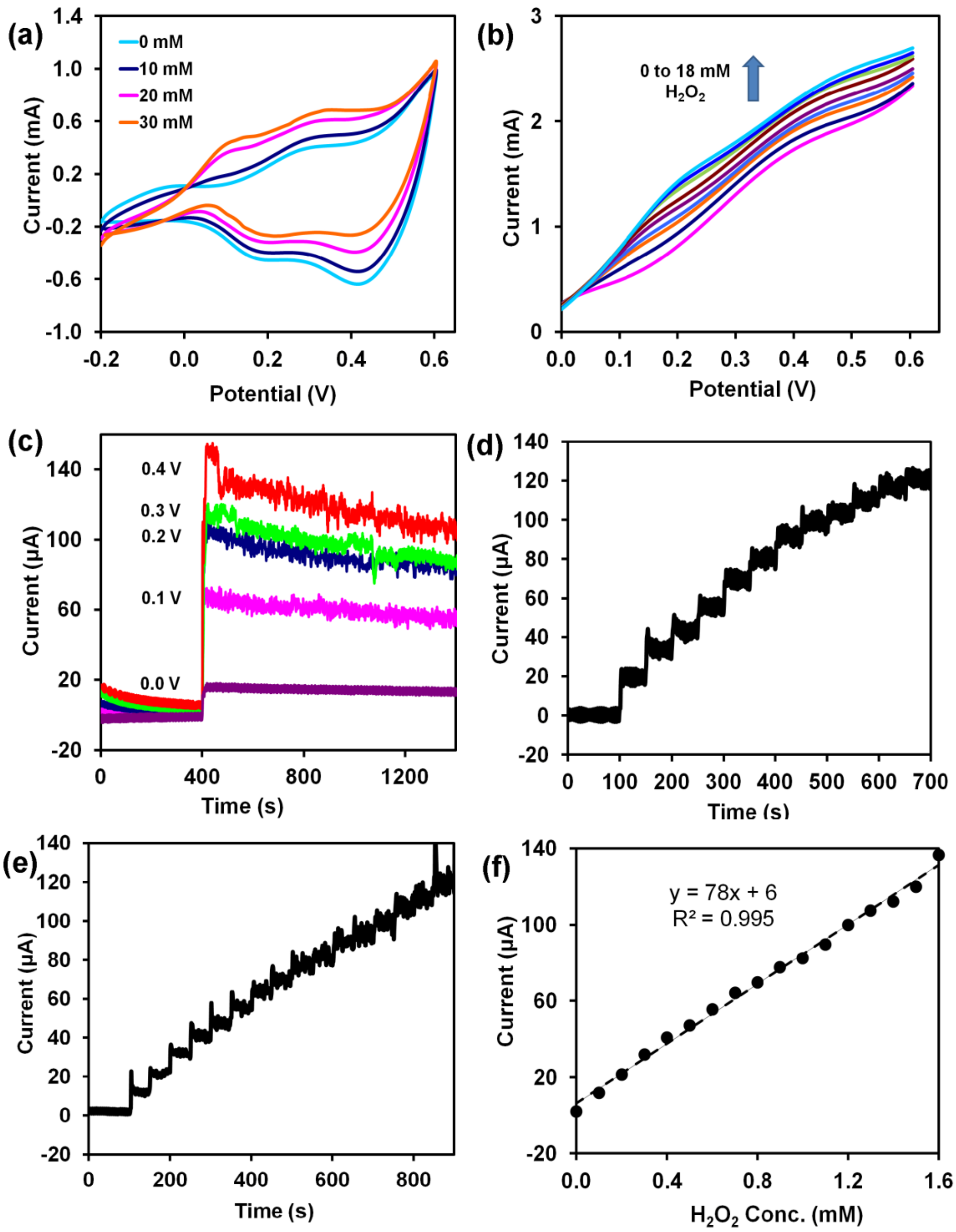

Figure 5.1. (a) CVs of CoOOH electrode in the absence or presence of various concentrations of H_2O_2 (scan rate: 10 mV/s), (b) LSVs of CoOOH electrode with successive addition of H_2O_2 (scan rate: 50 mV/s), (c) amperometric current curves at CoOOH electrode with sequential addition of 0.5 mM H_2O_2 for long duration (1000 s) at different applied potentials, (d) amperometric current response at CoOOH electrode held at 0 V with sequential addition of 0.5 mM H_2O_2, (e) amperometric current response at CoOOH electrode held at 0.1 V with sequential addition of 0.1 mM H_2O_2 and (f) the corresponding linear calibration plot for (e) (All experiments were performed in 0.1 M NaOH).

Various enzymeless H_2O_2 sensors based on nanostructured transition metal compounds have been reported in the literature since last decade. Nevertheless, fair comparison is extremely difficult to make because the sensing performance is strongly dependent on the experimental condition such as supporting electrolyte, electrolyte pH, electrode matrix and supporting electrodes (e.g. glassy carbon, gold and ITO etc.). For convenience, a list of sensors based on nanostructured transition metal compounds is compiled with their experimental conditions and detection performance in Table 5.1, focuses on sensors based on electrocatalytic oxidation of H_2O_2. As presented in the Table, materials such as MnOOH nanowires [5], MnO_2-graphene oxide composite [18], CuO nanobundles [19], CuO nanoparticles [20], CuO nanoflowers and nanowires on Cu [21], $Ni(OH)_2$ on Si nanowires [21] have been employed as electrooxidation sensing materials in alkaline medium. Comparatively, our sensor exhibits a few merits such as lower applied potential, higher sensitivity, and larger detection linear range than most of reported sensors.

Table 5.1. Summary of electrochemical sensing (electrooxidation) of hydrogen peroxide by various transition metal compounds.

	Electrode materials	**Electrolyte**	**Applied potential (V)**	**LOD (μM)**	**Sens. (μAmM^{-1}cm^{-2})**	**Resp. time (s)**	**Linear range (μM)**	**Ref**
	Manganese oxides							
1	$K_{2-x}Mn_8O_{16}$/ CPE[b]	0.01 M PBS pH 7.4	0.3 (Ag/ AgCl)	2	-	-	100-690	4
2	MnO_2-Na-montmorillonite	0.1 M PBS pH 7.4	0.65 (SCE)	0.15	31.4	-	0.5-7500	22
3	MnO_2-graphite	PBS pH 7	0.75 (SCE)	1.5	-	-	-	3
4	MnOOH nanowires	0.1 M NaOH	-	150	-	-	150-1600	5
5	MnO_2-MWCNTs[c]	0.2 M borate buffer, pH 7.8	0.45 (Ag/ AgCl)	0.8	1083	-	1.2-1800	23
6	MnO_2-graphene oxide	0.1 M NaOH	-0.3 (SCE)	0.8	38.2	< 5	5-600	18
7	β-MnO_2 nanorods	0.1 M PBS pH 8.0	0.8 (SCE)	2.45	21.74 μAmM^{-1}	< 5	2.5-42850	24
	Copper oxides/ sulfides							
8	CuO nanowires/ Cu	0.01 M PBS pH 7.4	0.6 Red: -0.2 (Ag/ AgCl)	- -	204.15 30.11	< 5 < 5	1680 28870	25
9	CuO nanobundles/ BPPG[d]	0.1 M NaOH	0.25[e] (SCE)	0.22	0.15 μAmM^{-1}	-	800	19
10	CuO nanoparticles/ CCE[f]	0.05 M NaOH	0.05 (SCE)	0.071	697	< 4	0.78-193.98	20
11	CuO nanoflowers/ Cu CuO nanowires/ Cu	0.1 M NaOH	-0.3 (SCE)	0.167 -	88.4 66.88	< 10 -	42.5-40000 6400-37200	26
12	CuO urchin	0.01 M PBS pH 7.4	0.6 (SCE)	-	-	-	10-5500	27
13	Cu_2O nanocrystals	0.1 M PBS pH 7.4	0.75 (Ag/AgCl)	0.39	52300	< 5	7	28
14	Cu_2S nanoparticles/ OMC[g]	o.1 M PBS pH 7.3	-0.1 (Ag/AgCl)	0.2	36.8	< 4	1-3030	29
	Cobalt oxides							
14	Co_3O_4 nanoparticles	0.1 M PBS pH 7.4	0.75 (Ag/AgCl)	0.4 nM	4860	< 2	0.004-300	7
15	Co_3O_4 nanowalls/ Co	0.01 M PBS pH 7.4	0.8 (Ag/AgCl)	2.8	1671	< 10	1400	6

16	CoOOH nanosheets/ Co	0.1 M NaOH	0.1 (Ag/AgCl)	40	99	< 3	1600	This study
	Nickel oxides							
17	β-$Ni(OH)_2$ nanosheets-chitosan	PBS pH 7	-0.1 (SCE)	-	24.76 μAmM^{-1}	< 5	5-80	8
18	β-$Ni(OH)_2$ nanocolumns	0.1 M PBS pH 7.2	0.4 (SCE)	-	3.995 μAmM^{-1}	-	0.1-10	30
19	$Ni(OH)_2$/ Si nanowires	0.5 M NaOH	0.2 (Ag/AgCl)	3.2	3310	< 5	500-5500	21
	Layered Double Hydroxides (LDH)							
20	Ni/Al-LDH Co/Al-LDH	0.01 M NaOH	0.06 0.49 (Ag/ AgCl)	0.009 0.05	74.82 μAmM^{-1} 97.61 μAmM^{-1}	- -	0.036-175 0.2-674	9
21	$LaNi_{0.5}Ti_{0.5}O_3$/ $CoFe_2O_4$	0.1 M NaOH	0.6 (SCE)	0.023	3210	< 3	0.1-8200	31
22	TiO_2-nanoparticles/ MWCNTs	0.1 M PBS pH 7.4	0.4 (Ag/AgCl)	0.4	13.4 μAmM^{-1}	< 5	2-20000	32

5.3.2 Electrochemical sensing of N_2H_4 on CoOOH nanosheets

CVs obtained on CoOOH electrode in 0.1 M NaOH solution containing different concentrations of N_2H_4 (0 to 8 mM) are shown in Figure 5.2a. It can be seen that the anodic current increases with the addition of N_2H_4, followed by a decrease in the corresponding cathodic current. This suggests that N_2H_4 is oxidized on the electrode surface via an electrocatalytic mechanism. Figure 5.2b shows the amperometric current response on CoOOH electrode held at 0 V for the successive addition of 0.2 mM N_2H_4, while Figure 5.2c shows the results at 0.1 V for the successive addition of 0.1 mM N_2H_4. Both 0 V and 0.1 V applied potentials are sufficient to detect a linear range of N_2H_4 concentration of 0-1.2 mM and 0-1.0 mM respectively. The linear calibration plots are I (μA) = (79 μAmM^{-1})[N_2H_4] + 8 μA (R^2 = 0.99) and I (μA) = (122 μAmM^{-1})[N_2H_4] + 14 μA (R^2 = 0.99) for applied potential of 0 V and 0.1 V respectively. The detection limit (signal to noise ratio of 3) and sensitivity determined from the calibration plots were 40 μM and 79 μAmM^{-1} (101 $\mu AmM^{-1}cm^{-2}$) for an applied potential of 0 V; and 20 μM and 122 μAmM^{-1} (155 $\mu AmM^{-1}cm^{-2}$) for applied potential of 0.1 V. Reproducibility of the proposed hydrazine sensor was also studied, and the relative standard deviation (RSD) is 4.48 % (n=5) for 0.6 mM N_2H_4.

The durability of a freshly prepared electrode was evaluated over a continuous 7 days for everyday use. After each experiment, the electrode was washed with distilled water, air dried and stored in ambient atmosphere at room temperature. Figure 5.3 shows the reading of amperometric currents when 0.4 mM N_2H_4 and another additional 0.4 mM N_2H_4 (a total of 0.8 mM N_2H_4) were added into the electrolyte in a span of 7 days. Unfortunately, it was found that the durability of the CoOOH electrode was not satisfactory. Obviously, the sensitivity of the electrode towards N_2H_4 sensing was decreasing with storage time. After 7 days, the current response dropped to 80 % and 72 % for the addition of 0.4 and 0.8 mM N_2H_4, respectively. Further study is required to understand the cause of the decreasing sensitivity over time.

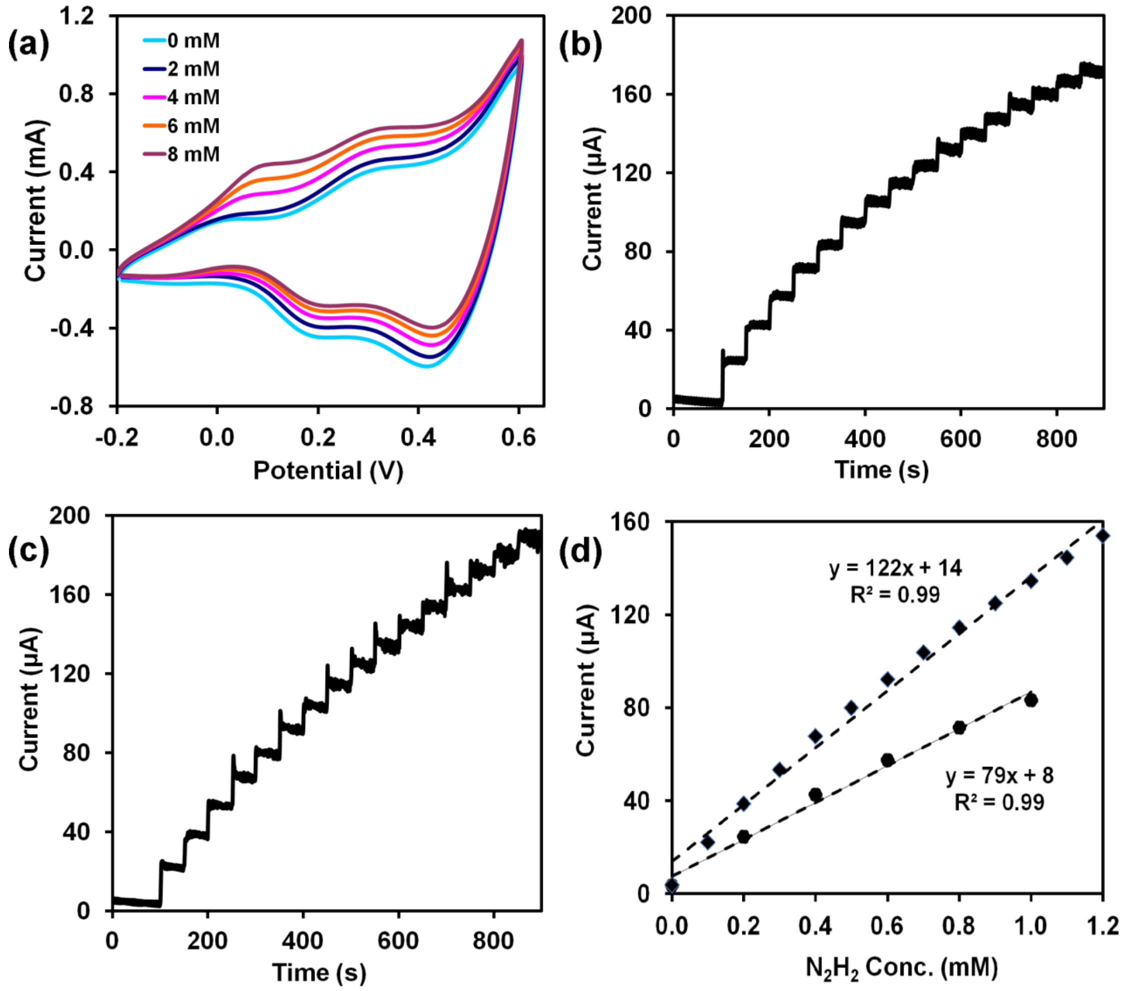

Figure 5.2. (a) CVs of CoOOH electrode in the absence or presence of N_2H_4 (scan rate: 10 mV/s), amperometric current curves at CoOOH electrode, (b) with the successive addition of 0.2 mM N_2H_4 held at 0 V, (d) with the successive addition of 0.1 mM N_2H_4 held at 0.1 V, (d) the corresponding linear calibration plots. (All experiments were performed in 0.1 M NaOH).

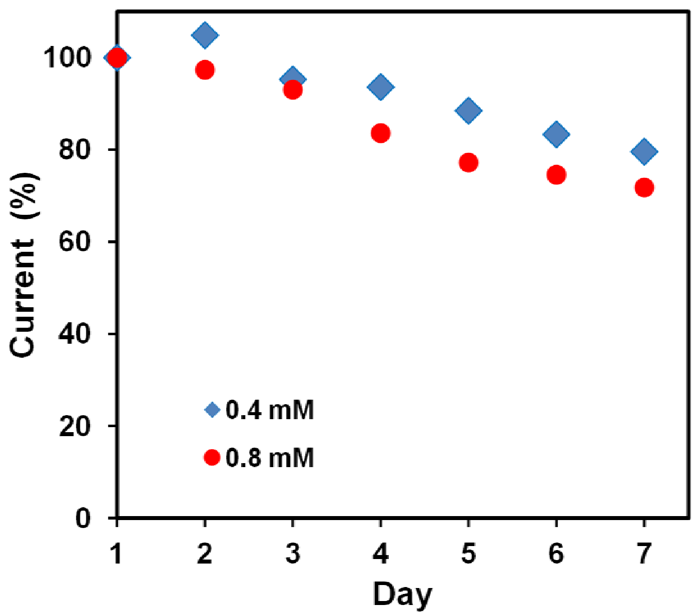

Figure 5.3. Current responses (in % with respect to Day 1) measured over a continuous 7 days with the addition of 0.4 and 0.8 mM N_2H_4.

Table 5.2 summarizes and compares the analytical details (linear range, detection limit, response time, sensitivity etc.) of our CoOOH electrode with other hydrazine sensors based on transition metal compounds in the literature. The data reveals that the analytical performances of the CoOOH electrode are comparable and most of the time better than those reported materials. Notably, the sensitivity of the CoOOH electrode (156 $\mu AmM^{-1}cm^{-2}$) is comparable with most of the electrodes. We believe this high sensitivity is due to the nanosheets arrays standing on a current-collecting metal foil. The structures offer larger electrochemical active surface area, higher utilization efficiency of the active materials, and superior mass and electron transport properties than conventional electrode. Besides using as an efficient amperometric sensor, it is anticipated that the extraordinary electrocatalytic activity of CoOOH nanosheets towards hydrazine can inspire further research on its use as electrocatalyst in alkaline hydrazine fuel cell[33].

Table 5.2. Summary of electrochemical sensing of hydrazine by various transition metal compounds.

	Electrode materials	Electrolyte	Applied potential (V)	LOD (µM)	Sensitivity (µAmM^{-1}cm^{-2})	Resp. time (s)	Linear range (µM)	Ref
1	Fe_2O_3/graphite	PBS pH 7.4	0.7 (SCE)	1.2	-	-	-	17
2	ZnO nanorods	0.01 M PBS pH 7.4	-	2.2	4.76	< 10	0.2-2.0	34
3	ZnO nanonails	0.01 M PBS pH 7.4	-	0.2	8560	< 5	0.1-1.2	2
4	ZnO nanowires	0.01 M PBS pH 7.4	-	0.084 7	12700000	< 5	0.5-1.2	35
5	ZnO nanoflowers-MWCNTs	0.1 M PBS pH 7.4	0.4 (SCE)	0.18	246.9 µAmM^{-1}	< 3	0.6-250	13
6	ZnO nanorods ZnO@C nanorods	0.1 M PBS pH 8	0.3 (SCE)	0.2 0.1	4480 9400	< 8 < 4	- -	36
7	ZnO microflowers ZnO microarchitecture	0.1 M PBS pH 7	0.1 (Ag/AgCl)	2.1 0.25	95 510	< 4 < 3	3.0-120 0.8-200	12
8	ZnO nanorods-SWCNTs	0.1 M NaOH	0.2 (Ag/AgCl)	0.17	100	-	0.5-50	37
9	PEG-coated ZnS nanoparticles	0.1 M PBS pH 7	-	1.07	89300	< 3	1-3000	38
10	MnO_2- MWCNTs nanocomposites	0.05 M PBS pH 7.4	0.3 (SCE)	0.2	-	< 5	0.5-1000	14
11	Mn_2O_3 nanofibers	0.1 M PBS pH 7	0.6 (Ag/AgCl)	0.3	474	< 5	644	39
12	CuO nanoparticles	0.01 M NaOH	0.27 (Ag/AgCl)	0.03	94.21 µAmM^{-1}	< 3	0.1 to 600	40
13	CuO nanoarray	0.1 M PBS pH 7	0 (SCE)	0.17	29.78 µAmM^{-1}	< 5	0.5-20	15
14	CuO nanoflowers	0.05 M PBS pH 7.2	0.1 (SCE)	-	941.5	< 10	50-5000	16
15	TiC@C nanofibers	0.1 M PBS pH 8	0.3 (Ag/AgCl)	0.026	-	-	0.1-1635	41
16	$NiFe_2O_4$-MWCNTs	0.1 M PBS pH 7.4	0.4 (SCE)	1.5	100 µAmM^{-1}	< 3	5-2500	42
17	CoOOH nanosheets	0.1 M NaOH	0 0.1 (Ag/AgCl)	40 20	101 156	< 3 < 3	40-1000 20-1200	this work

5.4 Conclusions

CoOOH nanosheets were synthesized by a simple alkaline treatment of cobalt foil at room temperature. This simple growth of nanostructures on a conducting substrate allows their direct use as non-enzymatic electrochemical sensors, thus eliminating the conventional electrode preparation procedures such as dispersion, sonication, dropping and drying. Due to the large surface area of the nanosheet structure, structural stability and fast electrical connection contributed from a self-supported feature, the nanostructured electrode presents excellent electrochemical sensing properties towards electrooxidation of small molecules such as H_2O_2 and N_2H_4 at very low applied potential. Further studies on using this strategy to prepare metal oxides nanostructures directly on metal substrates for electrochemical sensing properties can be extended to other materials.

5.5 References

1. W. Chen, S. Cai, Q. Q. Ren, W. Wen and Y. D. Zhao, *Analyst*, 2012, **137**, 49-58.
2. A. Umar, M. M. Rahman, S. H. Kim and Y. B. Hahn, *Chem. Commun.*, 2008, 166-168.
3. B. Sljukic and R. G. Compton, *Electroanalysis*, 2007, **19**, 1275-1280.
4. Y. H. Lin, X. L. Cui and L. Y. Li, *Electrochem. Commun.*, 2005, **7**, 166-172.
5. X. Cao, N. Wang, L. Wang, C. P. Mo, Y. J. Xu, X. L. Cai and G. Lin, *Sensors Actuat. B-Chem.*, 2010, **147**, 730-734.
6. W. Z. Jia, M. Guo, Z. Zheng, T. Yu, E. G. Rodriguez, Y. Wang and Y. Lei, *J. Electroanal. Chem.*, 2009, **625**, 27-32.
7. A. Salimi, R. Hallaj, S. Soltanian and H. Mamkhezri, *Anal. Chim. Acta*, 2007, **594**, 24-31.
8. B. Fang, A. X. Gu, G. F. Wang, B. Li, C. H. Zhang, Y. Y. Fang and X. J. Zhang, *Microchimica Acta*, 2009, **167**, 47-52.
9. Z. J. Yin, J. J. Wu and Z. S. Yang, *Biosens. Bioelectron.*, 2011, **26**, 1970-1974.
10. J. Yang, H. Xiang, L. Shuai and S. Gunasekaran, *Anal. Chim. Acta*, 2011, **708**, 44-51.

11. X. M. Miao, R. Yuan, Y. Q. Chai, Y. T. Shi and Y. Y. Yuan, *J. Electroanal. Chem.*, 2008, **612**, 157-163.

12. Y. H. Ni, J. S. Zhu, L. Zhang and J. M. Hong, *CrystEngComm*, 2010, **12**, 2213-2218.

13. B. Fang, C. H. Zhang, W. Zhang and G. F. Wang, *Electrochim. Acta*, 2009, **55**, 178-182.

14. M. F. Wang, C. Wang, G. F. Wang, W. Zhang and F. Bin, *Electroanalysis*, 2010, **22**, 1123-1129.

15. G. F. Wang, A. X. Gu, W. Wang, Y. Wei, J. J. Wu, G. Z. Wang, X. J. Zhang and B. Fang, *Electrochem. Commun.*, 2009, **11**, 631-634.

16. X. J. Zhang, A. X. Gu, G. F. Wang, W. Wang, H. Q. Wu and B. Fang, *Chem. Lett.*, 2009, **38**, 466-467.

17. B. Sljukic, C. E. Banks, A. Crossley and R. G. Compton, *Electroanalysis*, 2006, **18**, 1757-1762.

18. L. Li, Z. Du, S. Liu, Q. Hao, Y. Wang, Q. Li and T. Wang, *Talanta*, 2010, **82**, 1637-1641.

19. C. Batchelor-McAuley, Y. Du, G. G. Wildgoose and R. G. Compton, *Sensors Actuat. B-Chem.*, 2008, **135**, 230-235.

20. H. Razmi and H. Nasiri, *Electroanalysis*, 2011, **23**, 1691-1698.

21. Q. Yan, Z. Wang, J. Zhang, H. Peng, X. Chen, H. Hou and C. Liu, *Electrochim. Acta*, 2012, **61**, 148-153.

22. S. Yao, S. Yuan, J. Xu, Y. wang, J. Luo and S. Hu, *Appl. Clay Sci.*, 2006, **33**, 35-42.

23. B. Xu, M. L. Ye, Y. X. Yu and W. D. Zhang, *Anal. Chim. Acta*, 2010, **674**, 20-26.

24. A.-J. Wang, P.-P. Zhang, Y.-F. Li, J.-J. Feng, W.-J. Dong and X.-Y. Liu, *Microchimica Acta*, 2011, **175**, 31-37.

25. W. Jia, M. Guo, Z. Zheng, T. Yu, Y. Wang, E. G. Rodriguez and Y. Lei, *Electroanalysis*, 2008, **20**, 2153-2157.

26. M. J. Song, S. W. Hwang and D. Whang, *Talanta*, 2010, **80**, 1648-1652.

27. J. Y. Li, Xiong, S., Pan, J., Qian, Y. , *J. Phys. Chem. C*, 2010, **114**, 9645-9650.

28. S. Li, Y. Zheng, G. W. Qin, Y. Ren, W. Pei and L. Zuo, *Talanta*, 2011, **85**, 1260-1264.

29. X. Bo, J. Bai, L. Wang and L. Guo, *Talanta*, 2010, **81**, 339-345.

30. X. Zhang, A. Gu, G. Wang, B. Fang, Q. Yan, J. Zhu, T. Sun, J. Ma and H. H. Hng, *CrystEngComm*, 2011, **13**, 188-192.

31. D. Ye, Y. Xu, L. Luo, Y. Ding, Y. Wang, X. Liu, L. Xing and J. Peng, *Colloids Surf B Biointerfaces*, 2012, **89**, 10-14.

32. L.-C. Jiang and W.-D. Zhang, *Electroanalysis*, 2009, **21**, 988-993.

33. A. Serov and C. Kwak, *Appl. Catal. B-Environ.*, 2010, **98**, 1-9.

34. A. Umar, S. H. Kim, J. H. Kim and Y. B. Hahn, *J. Nanosci. Nanotechnol.*, 2007, **7**, 4522-4528.

35. A. Umar, M. M. Rahman and Y. B. Hahn, *Talanta*, 2009, **77**, 1376-1380.

36. J. P. Liu, Y. Y. Li, J. A. Jiang and X. T. Huang, *Dalton Trans*, 2010, **39**, 8693-8697.

37. K. N. Han, C. A. Li, M. P. Bui, X. H. Pham and G. H. Seong, *Chem. Commun.*, 2011, **47**, 938-940.

38. S. K. Mehta, Khushboo and A. Umar, *Talanta*, 2011, **85**, 2411-2416.

39. Y. Ding, C. Hou, B. Li and Y. Lei, *Electroanalysis*, 2011, **23**, 1245-1251.

40. Z. Yin, L. Liu and Z. Yang, *J. Solid State Electrochem.*, 2010, **15**, 821-827.

41. W. Zhang, K. Huo, Y. Jiang, L. Hu, R. Chen and P. K. Chu, *Microchimica Acta*, 2011, **175**, 137-143.

42. B. Fang, Y. Feng, M. Liu, G. Wang, X. Zhang and M. Wang, *Microchimica Acta*, 2011, **175**, 145-150.

Chapter 6 – α-Fe_2O_3 nanotubes-reduced graphene oxide composites as synergistic electrochemical capacitor materials

6.1 Introduction

Among the candidates for pseudocapacitors, iron oxides exhibit many advantageous characteristics, such as natural abundance, low cost, low toxicity and environmental friendliness. In contrast to other metal oxides (e.g. manganese or nickel oxides), iron oxides possess high hydrogen evolution potential in aqueous solution, this thus makes them a promising candidate as negative electrode in asymmetrical electrochemical capacitors (ECs).[1] By synthesizing the nanostructured iron oxides with high surface area, the charge storage capacity can be improved markedly over conventional forms of iron oxide.[2] Among the iron compounds for ECs, Fe_3O_4 is the most studied[3-10] while Fe_2O_3 remains under explored[11-14] since its insulating nature severely hinders the charge storage capability. Fe_3O_4 possesses metallic electrical conductivity (~10^2-10^3 S cm^{-1}) while α-Fe_2O_3 is an insulator (~10^{-14} S cm^{-1}) at room temperature.[2, 15, 16]

On the other hand, graphene emerges as an excellent electrode material for EDLC because of its high electrical conductivity, high surface area (2630 m^2g^{-1}) and rich electrochemistry. Studies on graphene or rGO materials prepared by different methods present specific capacitances ranging from 80 to 264 F/g in aqueous electrolytes.[17-19] The use of graphene for EC often suffers from a critical issue that the chemically reduced graphene tends to restack or agglomerate, thus reducing the effective surface area accessible to the electrolyte.[17-19] Rational design of nanoarchitecture by combining graphene materials and pseudocapacitive nanostructured metal oxide materials offers potential as new composite materials. Both components can serve as spacers to minimize their clustering, aggregation and thus increase the electrochemically accessible area. The two-dimensional graphene sheets can act as conductive mats to support the fast electric conduction through the electrode. This enables maximum utilization of the pseudocapacitive materials, particularly for those that are electrochemically active but not electrically conductive. Meanwhile, the presence of metal oxide increases the specific capacitance of graphene, which is limited by EDL capacitance. In turn, graphene increases the cycling stability suffered by these redox materials. Notwithstanding the considerable progress (Table 6.1), there seems to be still lack of control over the morphology of nanoparticles grown on rGO. It remains a major topic of interest to further improve the performance of metal oxide-graphene hybrids by combining well-defined nanostructured materials on electrically conducting rGO. In this Chapter, we demonstrate the design and fabrication of a novel nanocomposite by coupling α-Fe_2O_3 hollow NTs and rGO via a simple and green route to achieve high specific capacitance and long cycle life for EC.

Table 6.1. Electrochemical properties of various metal oxide-graphene materials composite electrodes explored in aqueous electrolytes.

Pseudocapactive material	Grap. mater.	Electrolyte	V. vs. Ag/AgCl	C_m (F/g)	Method	Ref.
MnO_2 microparticles	EG	1 M Na_2SO_4	-0.08 to 0.92	124	GS 0.1 A/g	20, 21
MnO_2 nanorods	EG	2 M $(NH_4)_2SO_4$	-0.08 to 0.92	158	GS 2 mA/cm^2	22
ZnO nanoparticles	rGO	1 M KCl	-0.58-0.42	11.3	CV 10 mV/s	23
SnO_2 nanoparticles	rGO	1 M H_2SO_4	0 to 1	43.4	CV 2 mV/s	24
MnO_2 nanoneedles	GO	1 M Na_2SO_4	-0.08 to 0.92	216	GS 0.15 A/g	25
$Ni(OH)_2$ nanoplates	GS	1 M KOH	0 to 0.55	935	GS 2.8 A/g	26
Mn_3O_4 nanoparticles	rGO	1 M Na_2SO_4 6 M KOH	-0.28 to 0.72 -0.58 to 0.42	175 256	CV 5 mV/s	27
MnO_2 nanoparticles	rGO	1 M Na_2SO_4	-0.18 to 0.82	310	CV 2 mV/s	28
Co_3O_4 nanoparticles	rGO	6 M KOH	-0.08 to 0.32	243.2	CV 10 mV/s	29
$Co(OH)_2$ nanoparticles	rGO	6 M KOH	-0.28 to 0.42	972.5	GS 0.5 A/g	30
Fe_3O_4 nanoparticles	rGO	1 M KOH	-0.88 to 0.12	480	GS 5 A/g	31
ZnO nanoparticles	rGO	0.1 M Na_2SO_4	-0.08 to 0.92	308	GS 1 A/g	32
$[Co_{0.66}Al_{0.34}(OH)_2]^+$ -nanosheets	GO	1 M KOH	0 to 0.55	1031	GS 1 A/g	33
α-$Ni(OH)_2$ nanoparticles	rGO	6 M KOH	0 to 0.45	1215	CV 5 mV/s	34
CeO_2 nanoparticles	rGO	6 M KOH	-0.08 to 0.42	208	GS 1 A/g	35

EG: exfoliated graphite, GO: graphene oxides, rGO: reduced graphene oxides, GS: graphene sheets.

6.2 Experimental Section

6.2.1 Synthesis of rGO, α-Fe_2O_3 NTs, and α-Fe_2O_3 NTs-rGO composites

GO used in this work was prepared by the Hummers method. α-Fe_2O_3 NTs were synthesized by a hydrothermal treatment of $FeCl_3$ solution in the presence of $NH_4H_2PO_4$ at 220°C. Detailed procedures have been reported.[36] For the synthesis of α-Fe_2O_3 NTs-rGO composites, ~20 mg of GO was added to 0.4 mmol of α-Fe_2O_3

NTs and dispersed in 40 mL of deionized water. The dispersion was then hydrothermally treated at 180 °C for 24 h.

6.2.2 Characterizations

The morphologies of the as-synthesized nanocomposites were examined with a JEOL JSM-6400F Field Emission Scanning Electron Microscope (FESEM) operating at 5 kV in high vacuum. TEM and HRTEM analysis, selected-area electron diffraction (SAED), and energy dispersive X-ray spectroscopy (EDS) were performed with a JEOL JEM 2010 Field-emission Transmission Electron Microscope at accelerating voltage of 200 kV. The crystal structure of the materials was analyzed by a Bruker D/MAX 2500 X-ray Diffractometer with Cu K_{α} radiation λ = 1.54056 Å. Raman spectrum was recorded by a micro-Raman system (Jobin-Yvon T64000) with a typical laser power of 0.2 mW under ambient conditions. Elemental analyses were carried out on a Perkin-Elmer 2400 Elemental Analyzer. Based on elemental analyses, the weight percentage of rGO content is 16 wt % in the α-Fe_2O_3 NTs-rGO composite.

6.2.3 Preparation of working electrodes

The electrodes for the electrochemical studies were prepared by the doctor-blade technique using a mixture of the active materials (Fe_2O_3 NTs, rGO, Fe_2O_3 NTs-rGO), Super P carbon (MMM Ensaco) and binder (Kynar 2801) in the mass ratio 70:15:15, using N-Methylpyrrolidone (NMP) as the solvent for the binder. The slurry was pressed on an etched-copper foil (thickness, 15 μm, Alpha Industries Co Ltd., Japan) as current collector. The electrode area and mass of active material were 2 cm^2 and 3–4 mg. A Shimadzu Libror AEM 5200 electronic microbalance was used for weighing of the electrodes.

6.2.4 Electrochemical studies

An electrochemical half-cell was assembled in a three-electrode configuration with Pt wire as the counter electrode, Ag/AgCl (3 M KCl) as the reference electrode, and the above-mentioned prepared materials as working electrodes. In the setup of working electrode, the conductive side of the copper foil was placed on a gold plate connected to a Teflon-sealed copper rod. The front side of the copper foil (with active materials) was sealed with a Teflon cell with an O-ring. Thus the working electrode had a exposed area of 0.785 cm^2 to the electrolyte and contained about 1.2-1.5 mg of the above mentioned mixed slurry. All electrochemical measurements were carried out in 1 M Na_2SO_4 solution as electrolyte. Cyclic voltammetry (CV) and galvanostatic charge-discharge studies were conducted using an Autolab PGSTAT 30 potentiostat/ galvanostat at room temperature (~24 °C).

6.3 Results and Discussion

6.3.1 Synthesis and characterizations of α-Fe_2O_3 NTs-rGO composite

Firstly, α-Fe_2O_3 NTs were prepared and washed with deionized water. These were then mixed with GO dissolved in deionized water and hydrothermally treated at 180 °C for 24 h. We found that the α-Fe_2O_3 NTs were well-attached and distributed on rGO sheets, with ~16 wt % rGO in the hybrid material (determined by elemental analysis). It is possible that the NTs were anchored covalently to the GO through functional groups such as carboxyl, hydroxyl, and epoxy groups on the surface of the GO sheets. In the control sample without α-Fe_2O_3 NTs, the starting GO sheets evolved into rGO due to reduction under hydrothermal conditions at 180°C, as evidenced by the red shift of the plasmon excitation peak to 257 nm in the UV-Vis spectra (Fig. 6.1). The UV-vis absorption spectra show that the absorption peak (227 nm) of GO corresponding to $\pi \rightarrow \pi^*$ transitions of aromatic C=C bonds red-shifts to 257 nm after hydrothermal treatment at 180°C for 24 h. Together with the increase in absorption in the whole spectral region, these show that the hydrothermal treatment restores the electronic conjugation within the rGO nanosheets. The small red shift of the Plasmon excitation peak of rGO from 257 to 266 nm in the α-Fe_2O_3 NTs composite indicates interaction between the π -electrons in r-GO and the α-Fe_2O_3 NTs in the resultant composite. The band at 427-437 nm is attributed to ligand to metal charge-transfer transitions of α-Fe_2O_3. The plasmon excitation peak is further red-shifted from 257 to 266 nm in the α-Fe_2O_3 NTs-rGO composite, indicating interaction between the π-electrons in rGO and α-Fe_2O_3 NTs in the resultant composite.

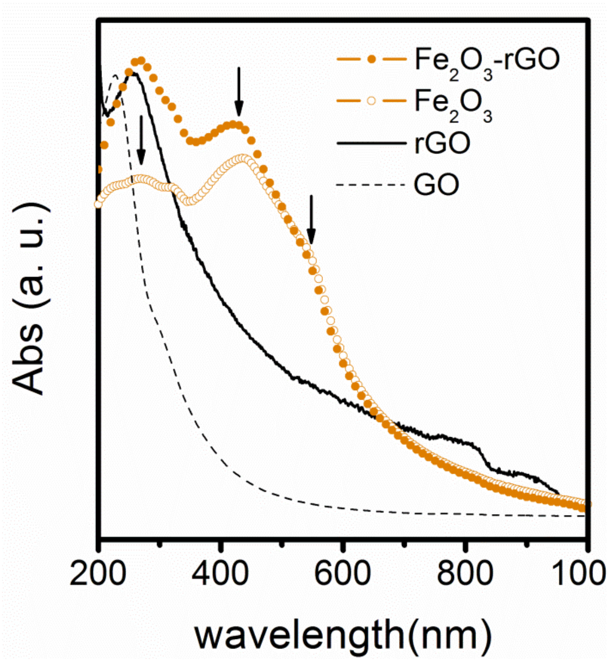

Figure 6.1. UV-Vis absorption spectra of GO and rGO.

SEM image of the α-Fe_2O_3 NTs composite (Fig. 6.2a) shows layered structure consisting of α-Fe_2O_3 NTs distributed over the rGO sheets. As shown in the detailed SEM view in Fig. 6.2b, the α-Fe_2O_3 NTs are wrapped in the rGO sheets, giving good dispersion of these oxide particles over the rGO. The rGO sheets overlap with each other to afford a three-dimensional conducting network for fast electron transfer between the active materials and the charge collector. The average length of the NTs is about 370 nm, with a wall thickness ranging from 15 to 40 nm. The NT hollow morphology was preserved after the reduction of GO to rGO. To elucidate the morphology of the composites fabricated, TEM measurements were carried out (Fig. 6.2c and d). High resolution TEM images and diffraction patterns shown in Fig. 6.2d clearly indicate that the NTs are single-crystalline trigonal α-Fe_2O_3, which is also confirmed by XRD patterns (Fig. 6.3a). The tube axes of the α-Fe_2O_3 NTs are in the <001> direction. The spacings between lattice planes are 2.7 Å, which correspond to those of Fe_2O_3 {014} planes.

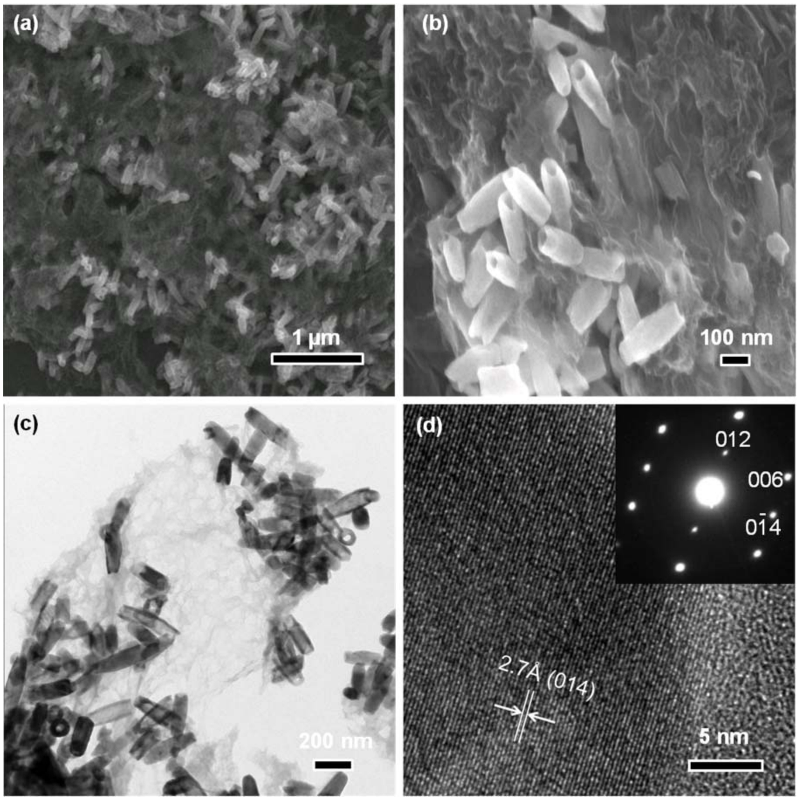

Figure 6.2. (a) SEM image of the α-Fe_2O_3 NTs-rGO composite, (b) higher magnification SEM image, (c) TEM image and (d) high-resolution TEM image and SAED (inset).

The phase purity and crystal structure of the α-Fe_2O_3 NTs-rGO samples were examined by XRD and Raman spectroscopy. As shown in Figure 6.3a, all of the diffraction peaks can be exclusively indexed as the trigonal α-Fe_2O_3 (JCPDS 87-1165), and no other impurities are observed. For the α-Fe_2O_3 NTs, the Raman band (Fig. 6.3b) at 225 cm^{-1} is assigned to A_{1g} mode and the bands at 290 and 407 cm^{-1} are assigned to E_g modes. The Raman spectrum of the α-Fe_2O_3 NTs-rGO composite shows typical peaks of hematite and characteristic peaks of the D and G bands from rGO at around 1331 and 1596 cm^{-1}. The G-band is related to the number of graphene layers while the D band is defect-related, and also appears as a strong band when the number of graphene layers in a sample is large. The strongest second-order band is observed around 2700 cm^{-1} (2D band).[37]

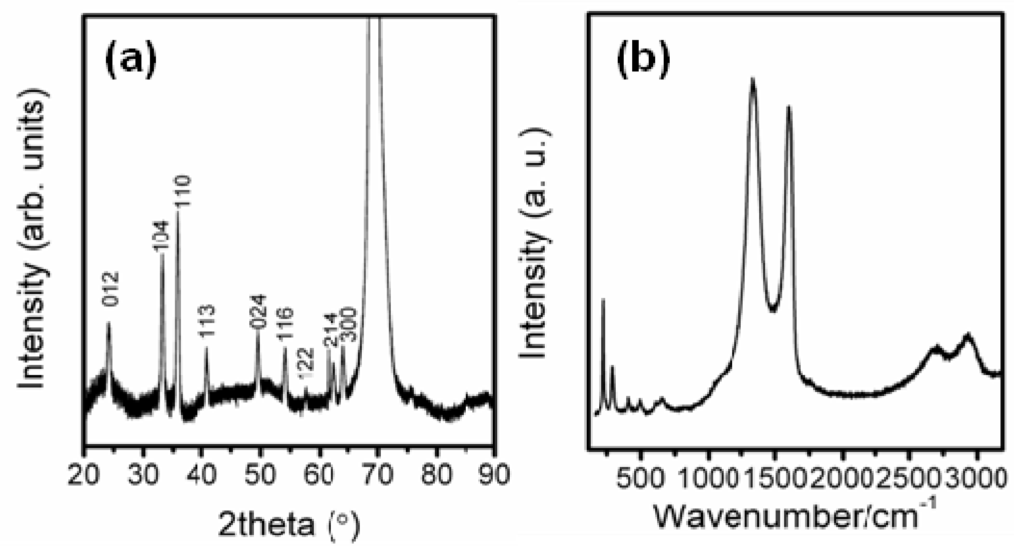

Figure 6.3. (a) XRD and (b) Raman spectrum of α-Fe_2O_3 NTs-rGO.

X-ray photoemission Fe2p spectra (XPS) for both α-Fe_2O_3 NTs and α-Fe_2O_3 NTs-rGO indicate two major components at binding energies (BEs) of 711.6 and 724.8 eV, corresponding to $Fe2p_{3/2}$ and $Fe2p_{1/2}$ core levels, respectively. In addition, a satellite peak at ~720 eV is also observed in accordance with reported data for α-Fe_2O_3 (Figure 6.4).[38] Figure 6.5 shows narrow scans from the C 1s region of GO and α-Fe_2O_3 –rGO, which could be deconvoluted into four components as summarized in Table 6.2. The original GO signal shows two separated peaks, as expected, due to the high percentage of oxygen functionalities. It is clear that the amount of components at higher BE region is relatively reduced in the α-Fe_2O_3–rGO composite, suggesting a decrease in the relative content of carbon species bound to oxygen. Based on the percentage of content before and after the hydrothermal reduction (Table 6.2), it is noted that C-O and C=O functional groups were significantly reduced but the percentage of C(O)O remained the same.

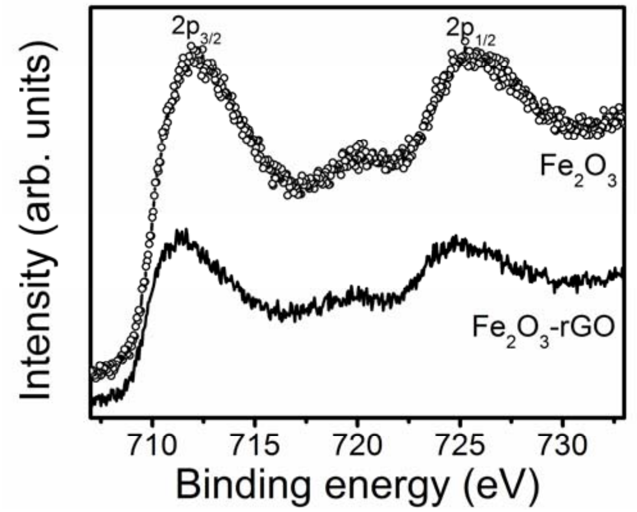

Figure 6.4. Fe 2p core-level XPS spectra of the α-Fe_2O_3 sample and α-Fe_2O_3 –rGO nanocomposite.

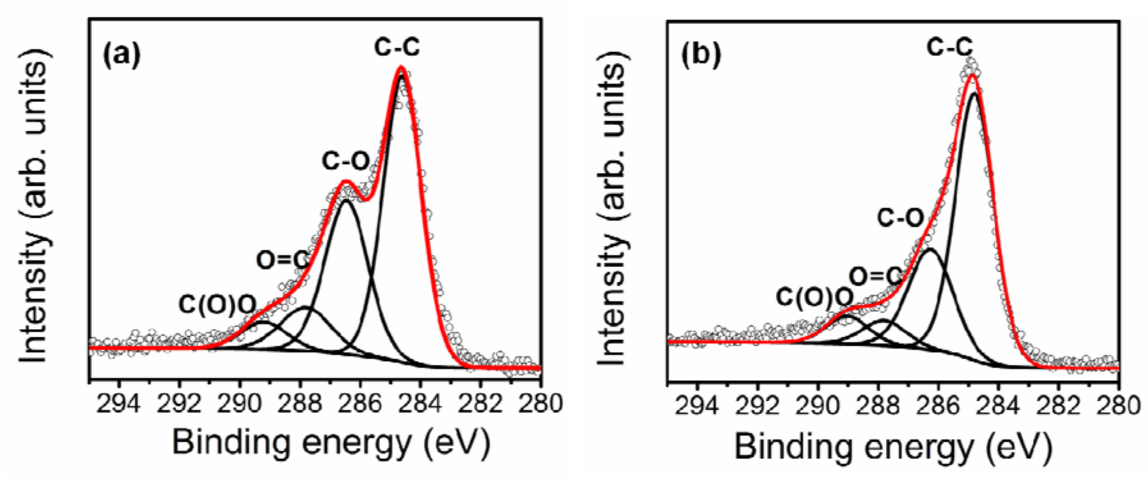

Figure 6.5. C 1s core-level XPS spectra of (a) GO and (b) α-Fe_2O_3-rGO.

Table 6.2. Percentage of various oxygenated functional groups

	C-C	C-O (epoxy)	C=O	C(O)O
B. E. (eV)	284.8	286.3	287.8	289.0
GO	52.1%	31.5%	9.4%	6.9%
Fe_2O_3-rGO	60.3%	26.5%	6.4%	6.9%

6.3.2 Electrochemical studies

The CV curves (Fig. 6.6a-d) present higher cathodic charges than anodic charges, especially when the electrodes were cycled to progressively negative potential. Similar phenomena of higher cathodic charges are observable in previous studies on iron oxides based electrodes.[2, 6, 12, 13] Wu et al. attributed the increase of capacitance towards increasing negative potentials to characteristic of space-charge-limited capacitance for a semiconductor-electrolyte interface.[2] In addition, the redox peaks observed at the negative potential region of the CV curve involve reversible reactions in conjunction with the H^+/H_2 irreversible reaction.[2] On the other hand, Cottineau et al. reported that a redox wave with a peak potential of -1.1 V is observed when a Fe_3O_4 electrode is cycled at potential more negative than -0.8 V (vs. Ag/ AgCl) in 0.1 M K_2SO_4 electrolyte.[5] The nature of this redox process is unclear. Based on Pourbaix diagram (potential-pH electrochemical equilibrium diagram) of Fe in aqueous solution, Fe_3O_4 may be reduced to metallic Fe under these conditions.

In our study, the cathodic charges may be associated with semiconductor-electrolyte character, as well as irreversible reduction of Fe^{3+} to Fe^{2+}/Fe and H^+ to H_2. Notably, surface (electro-)adsorption/ desorption of sulfate ions and redox reaction of sulfate may further complicate the CV curves (as well as charge-discharge curves).[7] Thus, the mechanisms are tentative and further evaluations such as *in situ* spectroscopic studies are required to provide direct evidences. The irreversible reduction processes are lesser when the electrodes were subjected to electrochemical studies at higher scan rates or current densities due to decreasing interaction between electrode and electrolyte.

Notably, for the α-Fe_2O_3 NTs, the separation between leveled anodic and cathodic currents at the same scan rates is much smaller than the α-Fe_2O_3 NTs-rGO composites (Fig. 6.6b), indicating smaller capacitance. The calculated specific capacitances (C_m) for both samples at different scan rates were depicted in Fig. 6.6e. The specific capacitance of the α-Fe_2O_3 NTs-rGO composites was calculated to be 215 F/g at a scan rate of 2.5 mV/s, 113 F/g at a high scan rate of 20 mV/s (~53 % of that at 2.5 mV/s), and 88 F/g at a very high scan rate of 100 mV/s (~41 % of that at 2.5 mV/s). The maximum specific capacitance of α-Fe_2O_3 NTs was calculated to be 30 F/g at a scan rate of 2.5 mV/s, 23 F/g at 20 mV/s (~77 % of that at 2.5 mV/s), and 21 F/g at 100 mV/s (~70 % of that at 2.5 mV/s). Over the different scan rates, the specific capacitance of the α-Fe_2O_3 NTs-rGO composite we fabricated is remarkably 4-7 times higher than the specific capacitance of α-Fe_2O_3 NTs.

Fig. 6.6c and 6.6d show galvanostatic charge-discharge curves of the α-Fe_2O_3 NTs and α-Fe_2O_3 NTs-rGO composites at different current densities. The α-Fe_2O_3 NTs-rGO composites presented a specific capacitance as high as 181 F/g at a discharge current density of 3 A/g and remained at 69 F/g for high discharge current density of 10 A/g. At the lower current density, the diffusion of ion from the electrolyte can gain access to the maximum surface area of the active materials, therefore a higher specific capacitance can be attained. With the increment of current density, the effective interaction between the ions and electrode is reduced resulting in a reduction in capacitance. Besides, this may also be due to the ohmic resistance resulting from poorer electrolyte diffusion within α-Fe_2O_3 NTs-rGO composites at high rate of charging-discharging. The specific capacitance of α-Fe_2O_3 NTs-rGO composites (114 F/g) is 5 times higher than the specific capacitance of α-Fe_2O_3 NTs

(22 F/g) at the discharge current density of 5 A/g. The values of specific capacitances determined from galvanostatic discharge curves (Fig. 6.6f) are comparable with the values derived from CV curves. Thus, both the CV and GS results suggested that, through the incorporation of rGO as conductive mats, the specific capacitance from α-Fe_2O_3 NTs can be enhanced significantly due to the more efficient charge transfer. The intimate interaction between α-Fe_2O_3 NTs and rGO formed through the hydrothermal reactions facilitates electron transfer between the hollow tubular α-Fe_2O_3 and the rGO sheets, and results in the high specific capacitance of the hybrid composites.

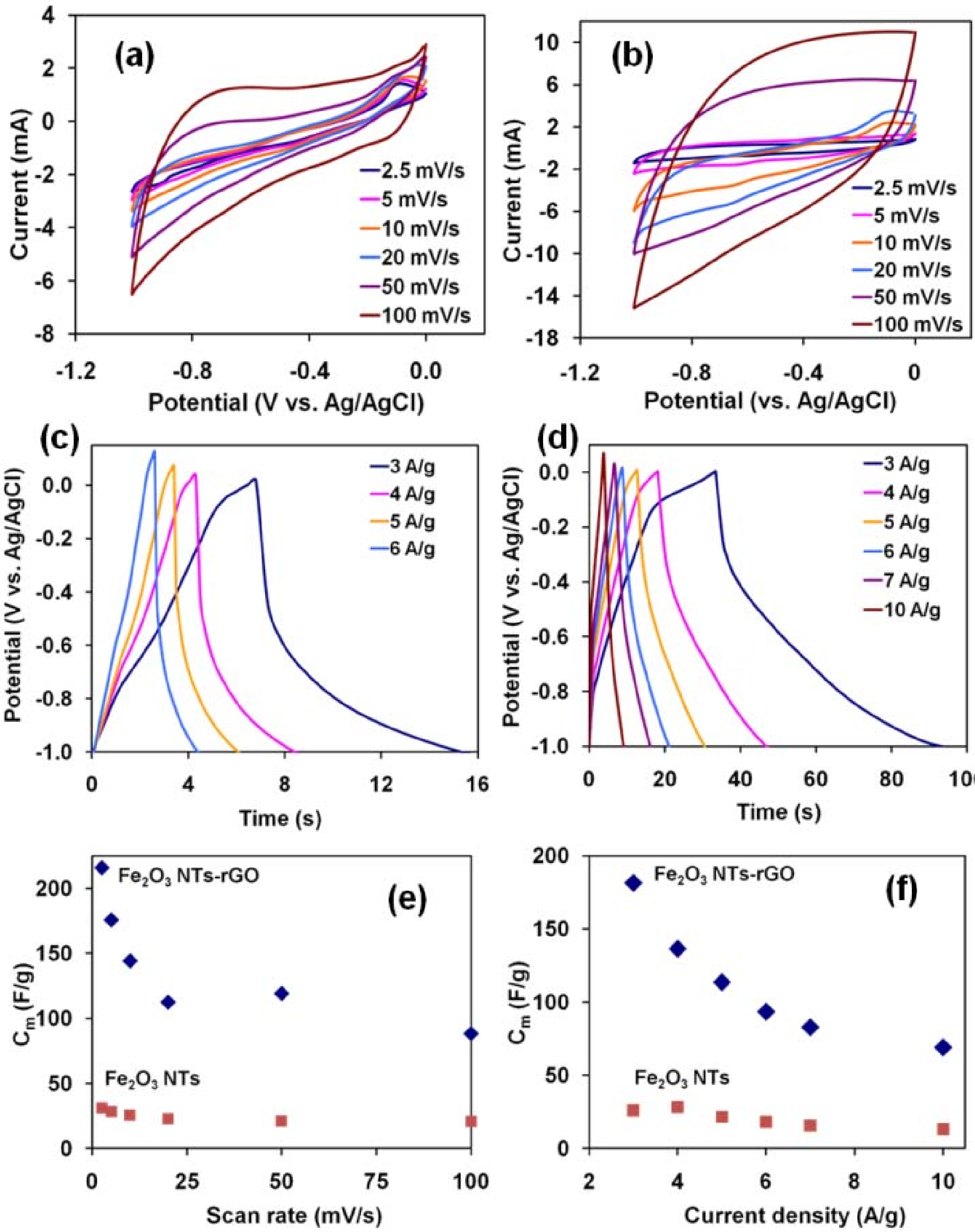

Figure 6.6. CV curves of (a) α-Fe_2O_3 NTs, (b) α-Fe_2O_3 NTs-rGO at different scan rates and galvanostatic charge-discharge curves of (c) α-Fe_2O_3 NTs, (d) α-Fe_2O_3 NTs-rGO electrodes at different current densities in 1 M Na_2SO_4, the corresponding calculated specific capacitances based on (e) CV curves and (f) galvanostatic charge-discharge curves.

Due to the high specific capacitance and wide working potential range, the α-Fe_2O_3 NTs-rGO composite has the potential to provide very high energy and power density. Consequently, it is highly desirable to couple this hybrid composite with a suitable counter electrode materials with a high oxygen evolution potential (e.g. MnO_2-based nanomaterials) to achieve a large operating potential range (~2 V in aqueous solution) and to optimize the energy and power densities.

The cycling performance of the α-Fe_2O_3 NTs and α-Fe_2O_3 NTs-rGO composites were compared by continuous GS experiments for 2000 cycles at 5 A/g in the potential window ranging from 0 to -1 V. Fig. 6.7a presents the specific capacitance retention of these two electrodes as a function of charge-discharge cycling numbers. α-Fe_2O_3 NTs exhibit high cycling stability and a capacitance loss of ~8 % after 700 cycles and remained stable after 2000 cycles. On the other hand, the specific capacitance of α-Fe_2O_3 NTs-rGO composite electrode increases about 10 % (from 117 F/g to 128 F/g) after initial 200 cycles. The increase of specific capacitance during these cycles can be attributed to the activation process that allows the trapped ions to diffuse out, while the expansion of interlayer spacing of rGO sheets facilitates counter ion intercalation[1, 39]. Charge-discharge curves of different cycles (namely cycle 1, 50, 100, 200 and 2000) from cycling studies are presented in Fig. 6.7b. There was no significant change of charge-discharge behavior except the gradual increment of capacitance from cycle 1 to cycle 200. The charge-discharge curves from cycle 200 to cycle 1000 are identical, showing that there was no material degradation occurring during the electrochemical process. With this, the specific capacitance of α-Fe_2O_3 NTs-rGO composite electrode remained almost totally unchanged up to 2000 cycles. These cycling studies revealed the remarkable long-term cycling stability of the α-Fe_2O_3 NTs-rGO composite electrode.

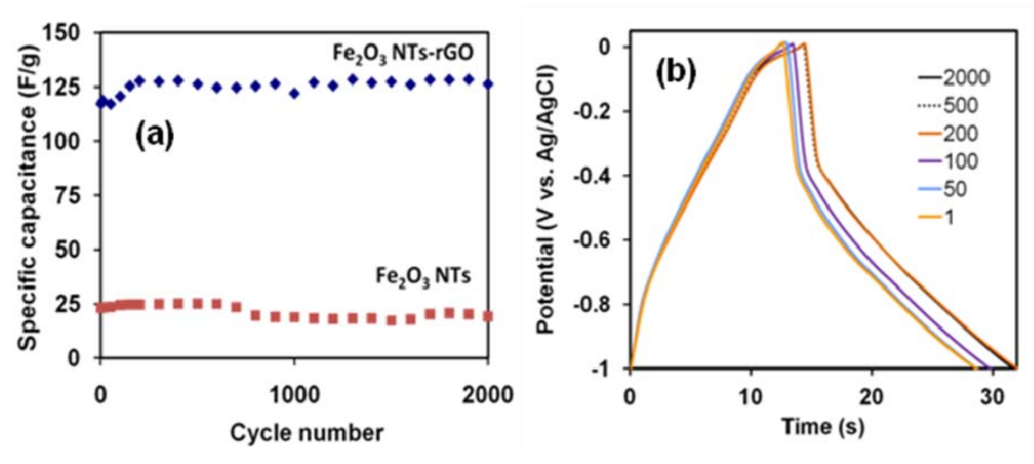

Figure 6.7. (a) Cycling performance of α-Fe_2O_3 NTs and α-Fe_2O_3 NTs-rGO composites at a current density of 5 A/g in 1 M Na_2SO_4, (b) Galvanostatic charge-discharge curves of α-Fe_2O_3 NTs-rGO electrode from different cycles.

6.4 Conclusions

In conclusion, a simple and green route to fabricate α-Fe_2O_3 NTs-rGO nanocomposites for ECs had been demonstrated. The hollow tubular α-Fe_2O_3 possesses high surface area, while the incorporation of rGO provides an efficient two-dimensional conductive pathway to allow a fast, reversible redox reaction, and thus maximize the capacitance. The excellent electrochemical performance of α-Fe_2O_3 NTs-rGO, i.e. its high specific capacitance, excellent cycling life, and large negative potential window, suggests that such nanocomposite is very promising as a negative electrode in asymmetric capacitors with neutral electrolytes.

6.5 References

1. P. Simon, Y. Gogotsi, *Nat. Mater.*, **2008**, 7, 845.
2. N.-L. Wu, S.-Y. Wang, C.-Y. Han, D.-S. Wu, L.-R. Shiue, *J. Power Sources*, **2003**, 113, 173.
3. S.-Y. Wang, N.-L. Wu, *J. Appl. Electrochem.*, **2003**, 33, 345.
4. T., Brousse, D. Bélanger, *Electrochem. Solid-State Lett.*, **2003**, 6, A244.
5. T. Cottineau, M. Toupin, T. Delahaye, T. Brousse, D. Belanger, *Appl. Phys. A*, **2006**, 82, 599.

6. K.W. Chung, K.B. Kim, S.-H. Han, H. Lee, *Electrochem. Solid-State Lett.*, **2005**, 8, A259.

7. S.-Y. Wang, K.-C. Ho, S.-L. Kuo, N.-L. Wu, *J. Electrochem. Soc.*, **2006**, 153, A75.

8. S. P. Pang, W. H. Khoh, S. F. Chin, *J. Mater. Sci.*, **2010**, 45, 5598.

9. J. Chen, K. Huang, S. Liu, *Electrochim. Acta,* **2009**, 55, 1.

10. J. Zhao, C. Johnson, A. Crossley, P. S. Grant, *J. Mater. Chem.*, **2010**, 20, 7637.

11. N. Nagarajan, I. Zhitomirsky, *J. App. Electrochem.*, **2006**, 36, 1399.

12. M.-S. Wu, R.-H. Lee, J.-J. Jow, W.-D. Yang, C.-Y. Hsieh, B.-J. Weng, *Electrochem. Solid-State Lett.*, 2009, 12, A1.

13. M.-S. Wu, R.-H. Lee, *J. Electrochem. Soc.*, **2009**, 156, A737.

14. D. Wang, Q. Wang, T. Wang, *Nanotechnology*, **2011**, 22, 135604.

15. Y. J. Kim, Y. Gao, S.A. Chambers, *Surf. Sci.*, **1997**, 371, 358.

16. F. J. Morin, *Phys. Rev.*, **1951**, 83, 1005.

17. Y. Sun, Q. Wu, G. Shi, *Energy Environ. Sci.*, **2011**, 4, 1113.

18. M. Pumera, *Energy Environ. Sci.*, **2011**, 4, 668.

19. C. Liu, Z. Yu, D. Neff, A. Zhamu, B. Z. Jang, *Nano Lett.*, **2010**, 10, 4863.

20. Wan, C., Azumi, K., Konno, H., *Electrochim. Acta* **2007**, *52*, 3061.

21. Wan, C., Azumi, K., Konno, H., *J. Appl. Electrochem.***2007**, *37*, 1055.

22. Yan, J., Fan, Z., Wei, T., Qie, Z., Wang, S., Zhang, M., *Mater. Sci. Eng. B* **2008**, *151*, 174.

23. Zhang, Y., Li, H., Pan, L., Lu, T., Sun, Z., *J. Electroanal. Chem.* **2009**, 634, 68.

24. Li, F., Song, J., Yang, H., Gan, S, Zhang, Q., Han, D., Ivaska, A., Niu, L., *Nanotechnol.* **2009**, 20, 455602.

25. Chen, S., Zhu, J., Wu, X., Han, Q., Wang, X., *ACS Nano* **2010**, 4, 2822.

26. Wang, H., Casalongue, H. S., Liang, Y., Dai, H., *J. Am. Chem. Soc.* **2010**, 132, 7472.

27. Wang, B., Park, J., Wang, C., Ahn, H., Wang, G., *Electrochim. Acta.* **2010**, 55, 6812.

28. Yan, J., Fan, Z., Wei, T., Qian, W., Zhang, M., Wei, F., *Carbon* **2010**, 48, 3825.

29. Yan, J., Wei, T., Qian, W., Shao, B., Zhao, Q., Zhang, L., Fan, Z., *Electrochim. Acta.* **2010**, 55, 6812.

30. Chen, S., Zhu, J., Wang, X., *J. Phys. Chem. C* **2010**, 114, 11829.

31. Shi, W. H., Zhu, J., Sim, D. H., Tay, Y. Y., Lu, Z., Zhang, X., Sharma, Y., Srinivasan, M., Zhang, H., Hng, H. H., Yan, Q., *J. Mater. Chem.* **2011**, 21, 3422.

32. Chen, Y.-L, Hu, Z.-A., Chang, Y.-Q., Wang, H.-W., Zhang, Z.-Y., Yang, Y.-Y., Wu, H.-Y., *J. Phys. Chem. C* **2011**, 115, 2563.

33. Wang, L., Wang, D., Dong, X. Y., Zhang, Z. J., Pei, X. F., Chen, X. J., Chen, B., Jin, J., *Chem. Commun.* **2011**, 47, 3556.

34. Lee, J. W., Ahn, T., Soundararajan, D., Ko, J. M., Kim, J.-D., *Chem. Commun.* **2011**, 47, 6305.

35. Wang, Y., Guo, C. X., Liu, J., Chen, T., Yang, H., Li, C. M., *Dalton Trans.* **2011**, 40, 6388.

36. H-M. Fan, J-B. Yi, Y. Yang, K-W. Kho, H-R. Tan, Z-X. Shen, J. Ding, X-W. Sun, M. C. Olivo, Y-P. Feng, *ACS Nano*, 2009, **3**, 2798.

37. D. Graft, F. Molitor, K. Ensslin, C. Stampfer, A. Jungen, C. Hierold, L. Wirtz, *Nano Lett.*, 2007, **7**, 238.

38. C-J. Jia, L-D. Sun, F. Luo, X-D. Han, L. J. Heyderman, Z-G. Yan, C-H. Yan, K. Zheng, Z. Zhang, M. Takano, N. Hayashi, M. Eltschka, M. Kläui, U. Rüdiger, T. Kasama, L. Cervera-Gontard, R. E. Dunin-Borkowski, G. Tzvetkov, J. Raabe, *J. Am. Chem. Soc.* 2008, **130**, 16968.

39. H. Wang, M. Yoshio, *Electrochem. Commun.* 2006, **8**, 1481.

40. Wu, N.-L., Wang, S.-Y., Han, C.-Y., Wu, D.-S., Shiue, L.-R., *J. Power Sources* **2003**, *113*, 173.

41. Wang, S.-Y., Wu, N.-L., *J. Appl. Electrochem.* **2003**, *33*, 345.

42. Brousse, T, Bélanger, D., *Electrochem. Solid-State Lett.* **2003**, *6*, A244.

43. Cottineau, T., Toupin, M., Delahaye, T., Brousse, T., Belanger, D., *Appl. Phys. A* **2006**, *82*, 599.

44. Chung, K.W., Kim, K.B., Han, S.-H., Lee, H., *Electrochem. Solid-State Lett.* **2005**, *8*, A259.

45. Wang, S.-Y., Ho, K.-C., Kuo, S.-L., Wu, N.-L., *J. Electrochem. Soc.* **2006**, *153*, A75.

46. Pang, S. P., Khoh, W. H., Chin, S. F., *J. Mater. Sci.* **2010**, *45*, 5598.

47. Chen, J., Huang, K., Liu, S., *Electrochim. Acta* **2009**, *55*, 1.

48. Zhao, X., Johnson, C., Crossley, A., Grant, P. S., *J. Mater. Chem.* **2010**, *20*, 7637.

49. Nagarajan, N., Zhitomirsky, I., *J. App. Electrochem.* **2006**, *36*, 1399.

50. Wu, M.-S., Lee, R.-H., Jow, J.-J., Yang, W.-D., Hsieh, C.-Y., Weng, B.-J., *Electrochem. Solid-State Lett.* **2009**, *12*, A1.

51. Wu, M.-S., Lee, R.-H., *J. Electrochem. Soc.* **2009**, *156*, A737.

52. Wang, D., Wang, Q., Wang, T., *Nanotechnology* **2011**, *22*, 135604.

53. Jin, W-H., Cao, G-T., Sun, J-Y., *J. Power Sources* **2008**, 175, 686.

54. Santos-Pena, J., Crosnier, O., Brousse, T., *Electrochim. Acta* **2010**, 55, 7511.

55. Radhakrishnan, S., Prakash, S., Rao, C. R. K., Vijayan, M., *Electrochem. Solid State Lett.* **2009**, 12, A84.

56. Sassin, M. B., Mansour, A. N., Pettigrew, K. A., Rolison, D. R., Long, J. L., *ACS Nano* **2010**, 4, 4505.

Chapter 7 – Vertically aligned iron (III) oxyhydroxide/ oxide nanosheets grown on iron substrates for electrochemical charge storage

7.1 Introduction

Transition metal oxides are actively being studied for the electrochemical energy storage in pseudocapacitive-type electrochemical capacitors (ECs). Hydrous ruthenium oxides represented the state-of- the-art pseudocapacitors. The high cost of ruthenium oxides limits its application and thus inspires tremendous efforts in searching for earth-abundant and economical alternative materials. Among the candidates, oxides and hydroxides of cobalt, nickel and manganese etc. present high pseudocapacitance due to their rich redox properties involving multiple oxidation states. These three types of compounds are ideally used as positive electrode materials based on their high capacitances in positive potential window. In contrast to other metal compounds, iron oxides/(oxy)hydroxides possess high hydrogen evolution potential in aqueous solution, thus stand out as promising negative electrode material. When coupling iron compounds based negative electrode with a positive electrode in a suitable electrolyte, the cell voltage of the asymmetric EC can be increased significantly, leading to marked improvement of energy and power densities [1-3].

The charge storage capacity of iron oxides/(oxy)hydroxides improve significantly compared to conventional powder forms when synthesized in high surface area nanostructures. The progress in the iron oxides/(oxy)hydroxides based ECs was briefly summarized in our recent report [4]. In comparison to conventional electrode prepared from powder composite, nanostructured arrays directly grown on metal substrates not only eliminate the laborious electrode preparation steps, they also present superior benefits such as robust active materials-current collector contact, binder and additive free, high surface area for electrochemical reactions, enhanced individual nanostructures-electrolyte contact and improved electron and ion transports [5, 6]. In this Chapter, we demonstrate iron (III) oxyhydroxide/oxide nanostructures grown on iron foils fabricated by a chemical oxidation method (or purpose-built "corrosion"/ "rusting"). We further investigate the electrochemical performances of the prepared samples in various electrolytes.

7.2 Experimental

Iron foils (Alfa Aesar, 0.1 mm thick, 99.5%) were used as a supporting substrate as well as a metal precursor for the growth of iron oxide nanostructures. The synthesis method was adapted from literature [7]. A stock of 0.1 M KCl solution was prepared in distilled water and the solution pH was adjusted to 3.00 with a pH meter (Metrohm) under drop-wise addition of concentrated HCl. Prior to reaction, the Fe foil of dimension 1.2 × 1.2 cm^2 was polished with silicon carbide sandpapers (200 grit and 500 grit). One side of the Fe foil was covered with Kapton polyimide tape to prevent contact with the reacting solution, thus serving as a conducting side for electrochemical experiments later. A magnetic bar was fixed to the covered side of Fe foil by polyimide tape as well. The Fe foil was immersed into the 0.1 M acidic KCl solution (10 mL). After stirring at 125 rpm on a hotplate maintained at 70 °C for 2 h, the sample was harvested and rinsed with distilled water. After drying in air, the sample was characterized by a JEOL JSM-6400F Field Emission Scanning Electron Microscope (FESEM) and Raman Spectroscope (Renishaw 2000 system) at 532 nm wavelength. The setup for electrochemical experiments was similar to our previous studies [8, 9]. A three-electrode cell was assembled with the iron (III) oxyhydroxide/oxide nanostructures as the working electrode, platinum wire as the counter electrode and Ag/AgCl as the reference electrode. All potentials were referenced to the Ag/AgCl (3 M KCl).

7.3 Results and Discussion

7.3.1 Characterizations of the nanostructured iron compound

After treatment in acidic KCl solution, the shiny surface of iron foils turned to greenish black indicating the formation of $Fe(OH)_2$ (green rust) or Fe_3O_4 (magnetite). However, upon drying in air, the surface turned to orange colour with some brown spots as indicated in Figure 7.1a. Previous studies demonstrated that some iron compounds are readily transformed to other phases under intense laser illumination. Thus, low laser power (1.6 mW) was employed in Raman studies, compensated with longer scanning time (400-1000 s). After recording each spectrum, a careful visual observation was made using white light illumination to detect any colour change associated with phase transformation. Extensive scans at different spots on the samples revealed two type of representative Raman spectra as shown in Figure 7.1b, with the 7.1b(i) predominant than the 7.1b(ii). The signature Raman peaks of hematite and magnetite are absent in our samples, ruling out the presence of hematite and magnetite [10-12]. Figure 7.1b(i) shows two sharp peaks at 250, 380 cm^{-1} and two broad peaks at 527, 692 cm^{-1} with a pattern similar to reported spectra of lepidocrocite (γ-FeOOH) [11, 13, 14]. Meanwhile, the broad peaks in Figure 7.1b(ii) are closely resembled to the spectrum of maghemite (γ-Fe_2O_3) [11, 15-17]. Notably, the KCl and HCl solutions play an important role in determining the final phases of the products. We obtained the γ-FeOOH and γ-Fe_2O_3 mixed phases reproducibly over 20 trials from the same stock solution while a previous study produced Fe_3O_4[7]. This remains an interesting issue to pursue in future studies. Figure 7.1c and d present typical FESEM images of the sample, showing dense arrays of nanosheets formed on the metal substrate.

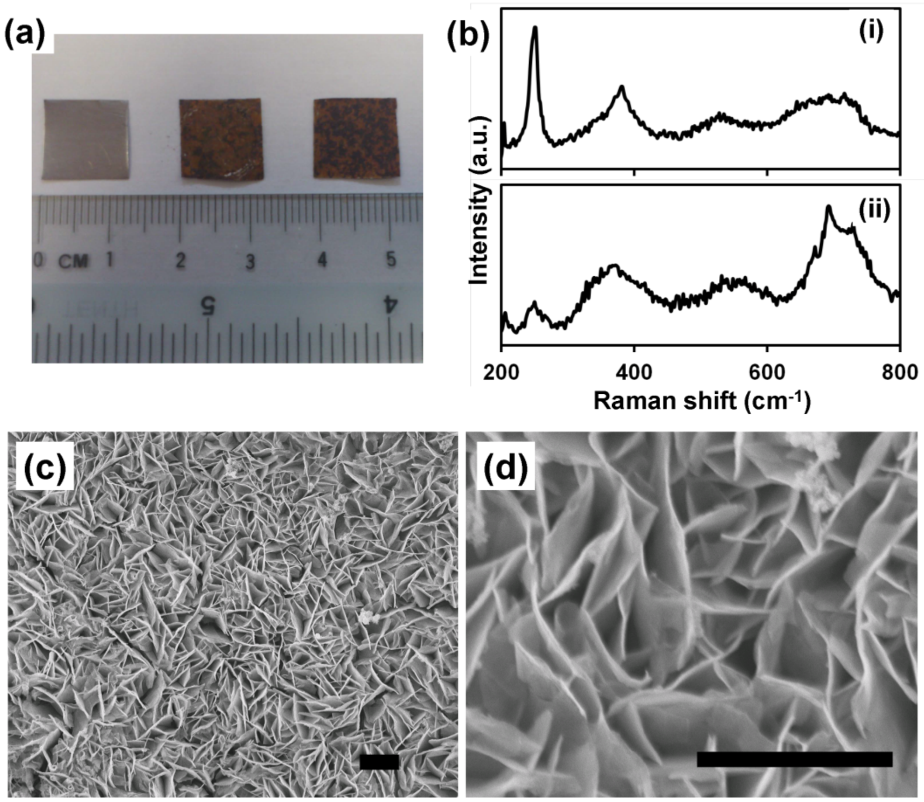

Figure 7.1. (a) Photographs of polished Fe foil (left) and two samples after reaction in acidic KCl solution, (b) two representative Raman spectra obtained for the samples, (c, d) SEM images of the iron (III) oxyhydroxide/oxide nanosheets at different magnifications. Scale bars are equal to 1 µm.

7.3.2 Electrochemical studies in three different electrolytes

The CV curves of the iron (III) oxyhydroxide/oxide electrode obtained in different electrolytes (1 M KOH, 1 M Na_2SO_4 and 1 M Na_2SO_3) and at different scan rates were presented in Figure 7.2a-c. In comparison (Figure 7.2d), as revealed by the integral area of the CV curves at the same scan rate, the capacitance of the electrode is much lower in 1 M KOH. Meanwhile, the shape of the CV curves for the electrode in Na_2SO_4 and Na_2SO_3 are similar. The capacitances of the electrode in

Na_2SO_4 and Na_2SO_3 can be correlated with the charge storage in the electric double layer at the electrode/electrolyte interface and the surface redox reactions[18]. The calculated areal capacitances of the electrode in different electrolytes and at different scan rates are presented in Figure 7.2e. The areal capacitance of the iron (III) oxyhydroxide/oxide electrode was the highest in Na_2SO_3, achieving 312 mF/cm^2 at 10 mV/s over a potential range of 0 to -0.8 V. Under the same condition, areal capacitances of the electrode in Na_2SO_4 and KOH were 240 mF/cm^2 and 63 mF/cm^2, respectively. Unfortunately, the rate capability of the electrode was unsatisfactory, it only retained 17 % and 19 % when the scan rate increased ten times in Na_2SO_3 and Na_2SO_4, respectively.

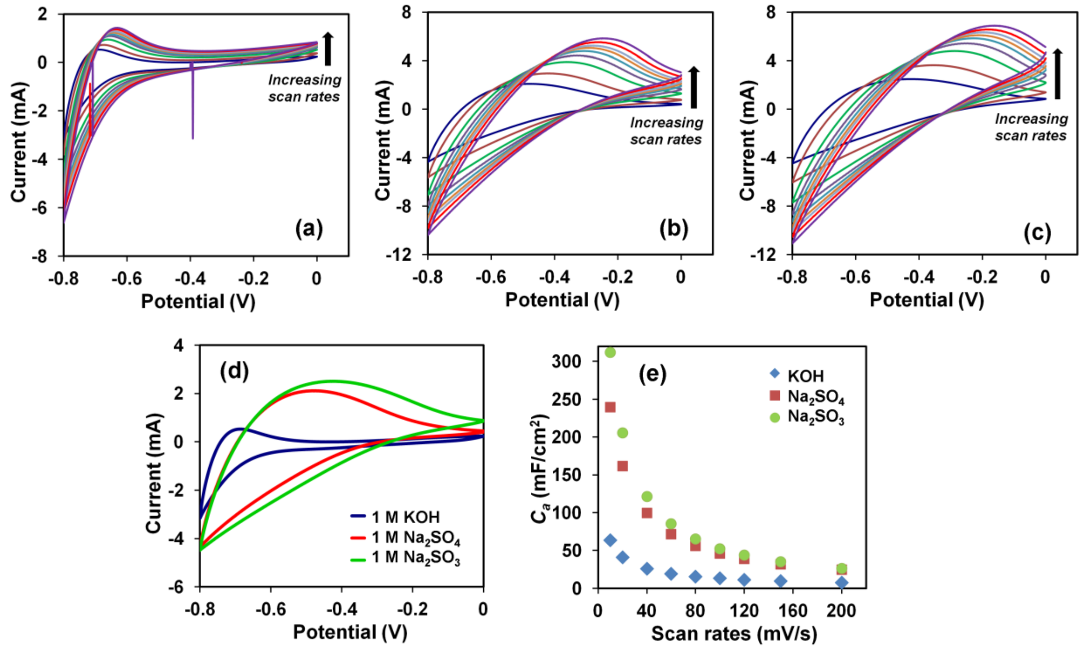

Figure 7.2. CV curves of the iron (III) oxyhydroxide/oxide electrode in (a) 1 M KOH, (b) 1 M Na_2SO_4 and (c) 1 M Na_2SO_3 at different scan rates (10 to 200 mV/s); (d) Comparison of CV curves of the iron (III) oxyhydroxide/oxide electrode in different electrolytes at 10 mV/s; (e) Areal capacitances of the iron (III) oxyhydroxide/oxide electrode against scan rates in different electrolytes calculated from (a-c).

Figure 7.3 exhibits the galvanostatic charge-discharge curves of the iron (III) oxyhydroxide/oxide electrode. As expected from the CV results, the charge-discharge times for the electrode in KOH were the shortest, while the charge-discharge curves in Na_2SO_3 and Na_2SO_4 were fairly similar. Areal capacitances of the iron (III) oxyhydroxide/oxide electrode calculated from the discharge curves are slightly higher than the values computed from CV curves due to the fact that the average slope of the discharge curves were obtained after the IR (voltage) drop. Nevertheless, the areal capacitances at increasing current densities presented a consistent trend that the iron (III) oxyhydroxide/oxide electrode suffered from considerable capacitance loss at high rates. The unsatisfactory rate capability is due to the low conductivity of the electrode, and the poorer electrolyte diffusion at high charge-discharge rates.

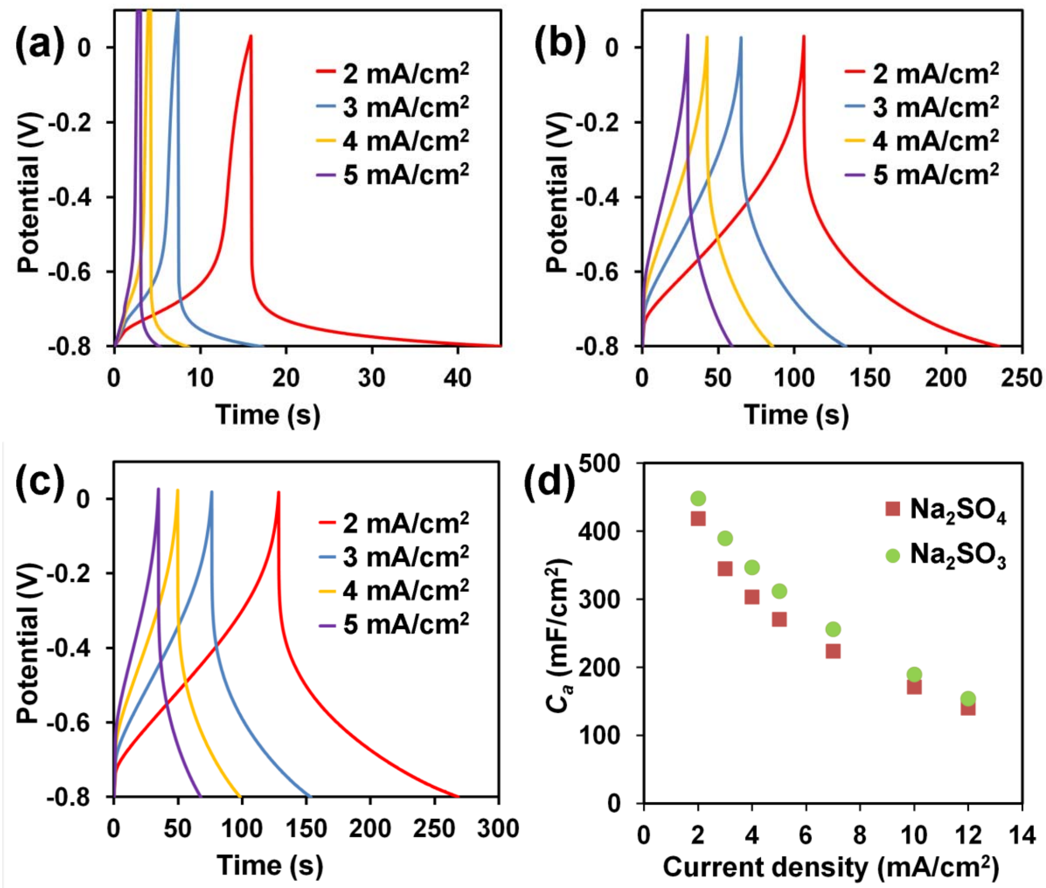

Figure 7.3. Galvanostatic charge-discharge curves of the iron (III) oxyhydroxide/oxide electrode in (a) 1 M KOH, (b) 1 M Na_2SO_4 and (c) 1 M Na_2SO_3 at different current densities; (d) Areal capacitances of the iron (III) oxyhydroxide/oxide electrode in 1 M Na_2SO_4 and Na_2SO_3 against current densities.

7.3.3 Cycling stability of electrodes in Na_2SO_3 and Na_2SO_4

The long term cycling life of the iron (III) oxyhydroxide/oxide electrode was evaluated by continuous CV cycling in Na_2SO_3 and Na_2SO_4. CV was chosen instead of galvanostatic charge-discharge because CV provides more information on the electrochemical events occurred, if any. Unexpectedly, upon continuous CV cycling of the electrode in Na_2SO_4, there was a drastic change in the shape of CV curve and an unusual increase of current (Figure 7.4a). This was accompanied with dissolution of materials from the electrode, turning the originally clear solution into yellow-greenish turbid solution (Figure 7.4b). A literature survey showed that the event is related to the electrochemical reduction of lepidocrocite in a solution containing sulfate[19]. During the cathodic cycling, solid lepidocrocite could be reduced to soluble Fe^{2+} species and sulfate green rust as hinted by the greenish colour. On the other hand, the iron (III) oxyhydroxide/oxide electrode remained stable for continuous 2000 CV cycles in Na_2SO_3. The areal capacitance of the electrode increased considerably in the first 600 cycles and then slowly up to 2000 cycles, attributable to the activation process that allows the trapped ions (e.g. K^+, Cl^- trapped during synthesis process) to diffuse out [4]. After the cycling studies in Na_2SO_3, there was no noticeable change in colour and the Raman spectra of the electrode, indicating the electrode is stable in Na_2SO_3.

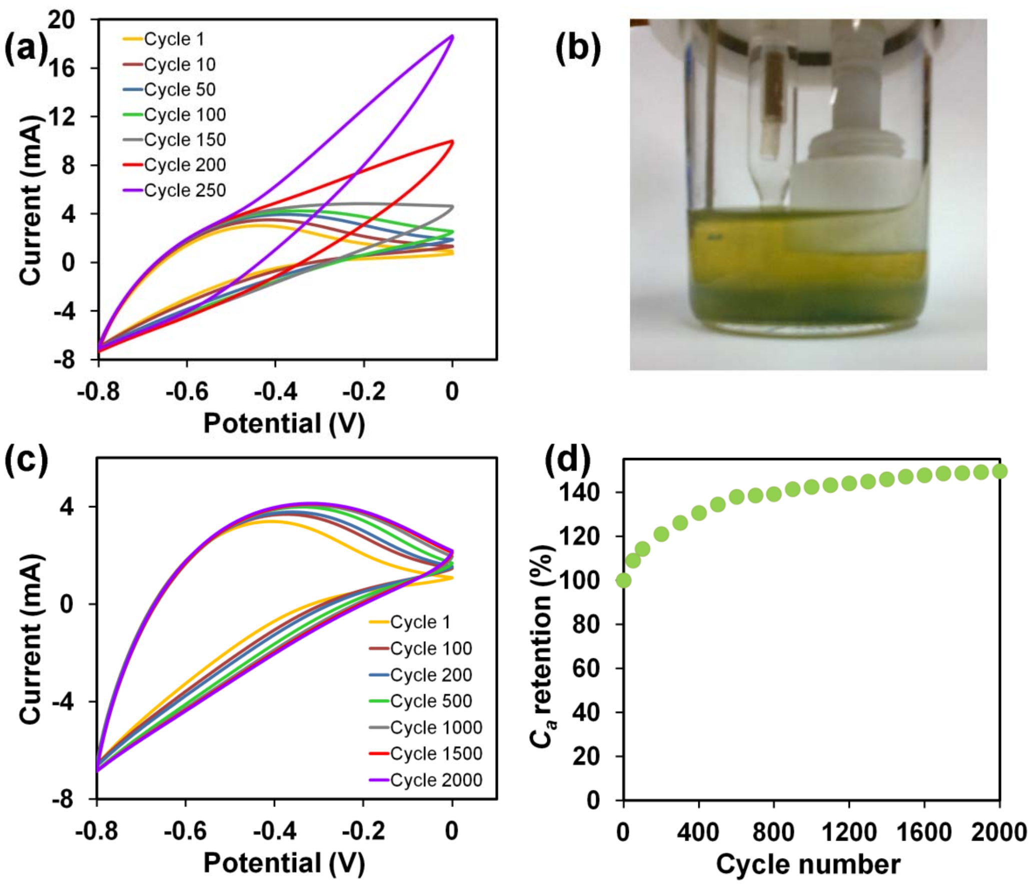

Figure 7.4. CV curves of iron (III) oxyhydroxide/oxide electrode at different cycles in (a) 1 M Na_2SO_4 and (b) a photograph showing the change in electrolyte color after 200 cycles; (c) CV curves of iron (III) oxyhydroxide/oxide electrode in 1 M Na_2SO_3 at different cycles and (d) the corresponding areal capacitance retention against cycle numbers.

7.4 Conclusions

Iron (III) oxyhydroxide/oxide nanosheets fabricated on iron foil was evaluated as an electrode for ECs in three commonly used aqueous electrolytes namely KOH, Na_2SO_4 and Na_2SO_3. CV and chronopotentiometry studies revealed much higher capacitances of the sample in Na_2SO_4 and Na_2SO_3 as compared to KOH. However, cycling studies showed that the electrode was not stable cathodically in Na_2SO_4. In order to give detailed comparative electrochemical studies, pure and different phases of iron oxides and hydroxides of similar morphology need to be synthesized. This effort is significant because different phases of iron oxides and hydroxides exhibit different electrochemical stability in different electrolytes.

7.5 References

1. T. Brousse and D. Belanger, *Electrochem. Solid-State Lett.*, 2003, **6**, A244-A248.
2. T. Cottineau, M. Toupin, T. Delahaye, T. Brousse and D. Belanger, *Appl. Phys. A-Mater.*, 2006, **82**, 599-606.
3. W.-H. Jin, G.-T. Cao and J.-Y. Sun, *J. Power Sources*, 2008, **175**, 686-691.
4. K. K. Lee, S. Deng, H. M. Fan, S. Mhaisalkar, H. R. Tan, E. S. Tok, K. P. Loh, W. S. Chin and C. H. Sow, *Nanoscale*, 2012, **4**, 2958-2961.
5. J. Jiang, Y. Li, J. Liu and X. Huang, *Nanoscale*, 2011, **3**, 45-58.
6. K. Xie, J. Li, Y. Lai, W. Lu, Z. a. Zhang, Y. Liu, L. Zhou and H. Huang, *Electrochem. Commun.*, 2011, **13**, 657-660.
7. K. C. Chin, G. L. Chong, C. K. Poh, L. H. Van, C. H. Sow, J. Y. Lin and A. T. S. Wee, *J. Phys. Chem. C*, 2007, **111**, 9136-9141.
8. K. K. Lee, P. Y. Loh, C. H. Sow and W. S. Chin, *Biosens. Bioelectron.*, 2013, **39**, 255-260.
9. K. K. Lee, P. Y. Loh, C. H. Sow and W. S. Chin, *Electrochem. Commun.*, 2012, **20**, 128-132.
10. R. M. Cornell and U. Schwertmann, in *The Iron Oxides: Structure, Properties, Reactions, Occurrences and Uses*, Wiley-VCH Verlag GmbH & Co, Weinheim, 2003.
11. D. L. A. deFaria, S. V. Silva and M. T. deOliveira, *J. Raman Spectrosc.*, 1997, **28**, 873-878.
12. S. J. Oh, D. C. Cook and H. E. Townsend, *Hyperfine Interact.*, 1998, **112**, 59-65.
13. D. Fu and J. C. Wren, *J. Nucl. Mater.*, 2008, **374**, 116-122.
14. S. X. Li and L. H. Hihara, *J. Electrochem. Soc.*, 2012, **159**, C147-C154.
15. P. Makie, G. Westin, P. Persson and L. Osterlund, *J. Phys. Chem. A*, 2011, **115**, 8948-8959.
16. Y. El Mendili, J.-F. Bardeau, N. Randrianantoandro, F. Grasset and J.-M. Greneche, *J. Phys. Chem. C*, 2012, **116**, 23785-23792.
17. A. M. Jubb and H. C. Allen, *ACS Appl. Mater. Interfaces*, 2010, **2**, 2804-2812.
18. S. Y. Wang, K. C. Ho, S. L. Kuo and N. L. Wu, *J. Electrochem. Soc.*, 2006, **153**, A75-A80.
19. H. Antony, L. Legrand, L. Marechal, S. Perrin, P. Dillmann and A. Chausse, *Electrochim. Acta*, 2005, **51**, 745-753.

Chapter 8 – Conclusions and Outlook

This thesis has described the preparation, characterizations and electrochemical applications of Fe- and Co-oxides/ oxyhydroxides nanostructures, specifically Co_3O_4 nanowalls, CoOOH and Co_3O_4 nanosheets, α-Fe_2O_3 nanotubes, α-Fe_2O_3 nanotubes-rGO composites and γ-FeOOH nanosheets. Several key conclusions drawn out from the results of this work are summarized and reviewed. In addition, some potential future works are proposed.

A major part of this thesis was devoted to the study of CoOOH nanosheets. For the first time, we demonstrated that CoOOH nanosheets can be grown *in situ* from (as a precursor) and on (as a substrate) metallic cobalt substrates via a wet oxidation approach. Various characterizations evidenced the formation of pure phase CoOOH by a single experimental step, in contrast to the conventional preparation of CoOOH involving post-treatment of $Co(OH)_2$. Being a highly electroactive material directly anchored on a conductive substrate, CoOOH nanosheets grown on cobalt foil stand out as an attractive material for electrochemical applications.

Potential applications of CoOOH nanosheets were explored as electrochemical sensors for glucose, hydrazine and hydrogen peroxide. Benefiting from the large surface area of the nanosheets and self-supported structure, the electrode exhibited excellent sensitivity higher than most reported literatures towards the detection of these analytes. However, the CoOOH electrode requires an alkaline medium for operation and this presents a significant challenge in biocompatibility, especially for glucose sensing. Other electroactive interferences such as ascorbic acid was found to be oxidized by the electrode, giving an amperometric current that overestimates the glucose value in physiological fluid. Thus, further works can be pursued to apply the electrode for non-enzymatic glucose fuel cell which is not restrained by the problems associated with physiological conditions. Besides, investigation of the CoOOH electrode as an electrocatalyst for oxygen evolution reaction can be carried out.

CoOOH nanosheets can be conveniently converted to Co_3O_4 nanosheets with good retention of the morphology. The samples provided opportunity to study the differences of CoOOH and Co_3O_4 for electrochemical capacitors, ruling out the effect of morphology. Comparative electrochemical capacitance studies revealed that CoOOH electrode was better than Co_3O_4 electrode in terms of higher specific capacitance and rate capability. However Co_3O_4 electrode possessed a better cycling stability. In future, various cobalt compounds such as $Co(OH)_2$, CoOOH, Co_3O_4, CoS, $LiCoO_2$ etc. of identical size and morphology can be prepared. The properties and applications as electrocatalyst, electrode materials can then be compared. The obtained information will be important and useful in choosing the optimum phase for certain applications.

Further, we demonstrated that although the conductivity of α-Fe_2O_3 is low, the electrochemical capacitance of α-Fe_2O_3 can be enhanced by rationally incorporating a small amount of conductive reduced graphene oxide (rGO). In a neutral electrolyte (Na_2SO_4), the specific capacitance of the α-Fe_2O_3 nanotubes-rGO was remarkably 4-7 times higher than the specific capacitance of α-Fe_2O_3 nanotubes. Due to the high specific capacitance and wide working negative potential window, the composite material is potentially useful to provide high energy and power densities. Consequently, it is highly desirable to couple the composite with a suitable counter electrode materials with a high oxygen evolution potential (thus wide working positive potential window), particularly MnO_2-based nanomaterials to achieve a large operating potential range (~1.8 V) in neutral aqueous electrolyte.

Lastly, γ-FeOOH (predominant phase) and γ-Fe_2O_3 nanosheets were formed *in situ* form and on iron substrates via oxidation in acidic KCl medium. Alkaline medium is not favourable for iron oxide/ hydroxide formation on iron substrate as iron can be passivated in a chloride-free solution with a pH above 8. Three type of common aqueous electrolytes used for iron compounds, namely KOH, Na_2SO_3, Na_2SO_4 were employed to evaluate the electrochemical performance of γ-FeOOH nanosheets. The γ-FeOOH exhibited an impressively high areal capacitance (~300-400 mF/cm^2) in Na_2SO_3. However, due to the low conductivity of γ-FeOOH, the rate capability was unsatisfactory. Moreover, it was realised that γ-FeOOH electrode was not stable in Na_2SO_4, undergoing reductive dissolution. In future, various experimental conditions and chemical formulations need to be tuned to oxidize the iron surface to different phases of iron compounds (α-FeOOH, β-FeOOH, α-Fe_2O_3, β-Fe_2O_3, γ-Fe_2O_3, Fe_3O_4 and many more) and nanostructures. The various samples can be compared in terms of various electrochemical applications for instance photoelectrochemical water splitting.